

MAGNETIC FIELD EFFECTS ON COLD HOLLOW
CATHODE DC DISCHARGE: AN EXPERIMENTAL
AND MODELING STUDY

By

Montu Prafulbhai Bhuva

ENGG06201504002

INSTITUTE FOR PLASMA RESEARCH, GANDHINAGAR

*A thesis submitted to the
Board of Studies in Engineering Sciences*

*In partial fulfillment of the requirements
for the degree of*

DOCTOR OF PHILOSOPHY

of

HOMI BHABHA NATIONAL INSTITUTE



September 2020

Homi Bhabha National Institute

Recommendations of the Viva Voce Committee

As members of the Viva Voce Committee, we certify that we have read the dissertation prepared by **Mr. Montu Prafulbhai Bhuvu** entitled "Magnetic field effects on Cold Hollow Cathode DC Discharge : An Experimental and Modeling Study" and recommend that it may be accepted as fulfilling the thesis requirement for the award of Degree of Doctor of Philosophy.

P. Sharma

----- Date : 22/ 02/ 2021

Chairman : Dr. Pramod K Sharma

Shantanu Karkari

----- Date : 22/ 02/ 2021

Guide/ Convener : Dr. Shantanu Kumar Karkari

K.R. Gunasekhar

----- Date : 22/ 02/ 2021

Examiner : Dr. K. R. Gunasekhar

M. Bandyopadhyay

----- Date : 22/ 02/ 2021

Member : Dr. M. Bandyopadhyay

G. Ravi

----- Date : 22/ 02/ 2021

Member : Dr. G. Ravi

Sunil Kumar

----- Date : 22/ 02/ 2021

Technology Advisor : Shri. Sunil Kumar

Final approval and acceptance of this thesis is contingent upon the candidate's submission of the final copies of the thesis to HBNI.

I hereby certify that I have read this thesis prepared under my direction and recommend that it may be accepted as fulfilling the thesis requirement.

Shantanu Karkari

----- Date : 22/ 02/ 2021

Guide : Dr. Shantanu Kumar Karkari

Place: IPR, Gandhinagar

STATEMENT BY AUTHOR

This dissertation has been submitted in partial fulfillment of requirements for Ph.D. in Engineering Sciences at Homi Bhabha National Institute (HBNI) and is deposited in the Library to be made available to borrowers under rules of the HBNI.

Brief quotations from this dissertation are allowable without special permission, provided that accurate acknowledgement of source is made. Requests for permission for extended quotation from or reproduction of this manuscript in whole or in part may be granted by the Competent Authority of HBNI when in his or her judgement the proposed use of the material is in the interests of scholarship. In all other instances, however, permission must be obtained from the author.



Montu Prafulbhai Bhuvra

CERTIFICATION ON ACADEMIC INTEGRITY

1. I Mr. Montu Prafulbhai Bhuvu HBNI Enrollment No. ENGG06201504002 hereby undertake that, the Thesis titled *Magnetic field effects on Cold Hollow Cathode DC Discharge: An Experimental and Modeling Study* is prepared by me and is the original work undertaken by me and free of any plagiarism. That the document has been duly checked through a plagiarism detection tool and the document is plagiarism free.
2. I am aware and undertake that if plagiarism is detected in my thesis at any stage in future, suitable penalty will be imposed as per the applicable guidelines of the institute/UGC.



Montu Prafulbhai Bhuvu

Date: 22/02/2021

Endorsed by the Thesis Supervisor:

I certify that the work done by the Researcher is plagiarism free.

Signature *Shantanu Karkari*

Date: 22/02/2021

Name: Dr. Shantanu Kumar Karkari

Designation: Associate Professor

Department/ Centre: Department of Atomic Energy

Name of the CI/ OCC: Institute for Plasma Research

List of Publications arising from the thesis

Journal:

1. **Characteristics of an elongated plasma column produced by magnetically coupled hollow cathode plasma source**
M. P. Bhuva, S. K. Karkari and Sunil Kumar *Physics of Plasmas* **25(3)**, 033509, (2018).
2. **The Role of Apex Angle of a Cone-Shaped Hollow Cathode on Plasma Parameters**
M. P. Bhuva and S. K. Karkari *IEEE Transactions on Plasma Science* **47(6)**, 2929-2936, (2019).
3. **Influence of cold hollow cathode geometry on the radial characteristics of downstream magnetized plasma column**
M. P. Bhuva, S. K. Karkari and Sunil Kumar *Plasma Sources Science and Technology* **28(11)**, 115013, (2019).
4. **Understanding Langmuir probe characteristics of a magnetized plasma column in partial contact with grounded probe reference**
M. P. Bhuva, S. K. Karkari and Sunil Kumar *Journal of Instrumentation* **14(11)**, 1748-0221, (2019).

Conferences Presentations:

1. **The influence of conical and cylindrical hollow cathode geometries on the characteristics of a magnetized plasma column**
M. P. Bhuva, S. K. Karkari and Sunil Kumar. *72nd Annual Gaseous Electronics Conference, October 28 to November 1, 2019*, College Station, Texas, USA.
2. **Magnetization effect on secondary electron emission in a hollow cathode plasma source**
M. P. Bhuva. *71st Annual Gaseous Electronics Conference, November 5 to 9, 2018*, Portland, Oregon, USA.
3. **Effect of cathode geometry on magnetically coupled hollow cathode plasma source**
M. P. Bhuva, S. K. Karkari and Sunil Kumar. *27th IAEA Fusion Energy Conference, October 22 to 27, 2018*, Gandhinagar, India.



Montu Prafulbhai Bhuva

Dedicated
to
my parents

ACKNOWLEDGEMENTS

First and foremost, I would like to acknowledge my Ph.D. supervisor *Dr. Shantanu Kumar Karkari* for his overall guidance and invaluable support over the period of my entire research tenure. He has always made himself available to discuss the experimental results and has sincerely helped me a lot in improvising my thinking, visualizing and presentation skills. I would also like to acknowledge my technology advisor *Shri. Sunil Kumar* for his overall technical support in this research. Also, I would like to thank my entire doctoral committee for regularly reviewing my research progress and providing the important suggestions which have significantly improved the overall research presented in this thesis.

I am extremely thankful to my mom and dad as they have always encouraged me to move ahead in life and pursue my dreams. Especially, I would like to acknowledge my dad, because without his encouragement and support my career would have never entered in the research domain. I would also like to thank my friends and all the members of the MPD (Magnetized Plasma Division) lab for their fruitful discussions and their support in conducting the experiments. In-person, I am extremely thankful to my roommate and my closest friend *Jay Joshi* and his family members for their invaluable support, care and love. They have always treated me as a part of their family and I sincerely find myself blessed with all of them. In my entire research journey, I was fortunate to be accompanied by very good life long friends especially my dearest sisters *Bhumi Chaudhary* and *Shikha Binwal*, who have always been my moral strength and source of inspiration.

In my Ph.D. tenure, I also got the opportunity to visit international conferences for exploring my research skills and building the research network. I am extremely thankful to *Institute for Plasma Research, Homi Bhabha National Institute, Department of Science and Technology* and *American Physical Society* for providing me the financial support to attend the *Gaseous Electronics Conference* in 2018 and 2019. Finally, I acknowledge the *Department of Atomic Energy, Government of India* for supporting the overall Ph.D. program.



Montu Prafulbhai Bhuvra

Contents

Abstract	iv
List of Figures	vi
List of Tables	xv
1 Introduction	1
1.1 DC Electric Discharge	4
1.1.1 Basics of a DC glow discharge	6
1.1.2 Effect of Hollow Cathode geometry	8
1.2 Sustenance of the DC discharge and role of secondary electrons	9
1.3 Magnetic field effect in DC discharge	11
1.3.1 Application of $\vec{E} \times \vec{B}$ drifts in DC discharge devices	12
1.3.2 Magnetization effects in a hollow cathode device	14
1.4 Thesis outline	15
2 Experimental Consideration for Hollow Cathode Plasma Source and Diagnostic	17
2.1 Discharge using hollow cathode devices	17
2.1.1 Hollow Cathode Discharge Mechanism	19
2.1.2 DC hollow cathode discharge in presence of magnetic field	21
2.1.3 Current constituting through the discharge	22
2.2 Design and Construction of Hollow Cathode Device	23
2.2.1 Electrical Discharge Circuit	25
2.3 Experimental Setup	26
2.3.1 Linear Device and Magnetic Field Topology	28
2.4 Langmuir probe and measurement circuit	28
2.4.1 Measurement circuit calibration	30
3 Langmuir Probe Application in Magnetized Plasma Column	33
3.1 Langmuir Probe characteristics	34
3.2 Single Langmuir probe theory	36

3.2.1	Cylindrical probe characteristics	37
3.2.2	Probe characteristics for two-temperature electron populations	39
3.3	Magnetic field and reference electrode effects on Langmuir probe characteristics	41
3.3.1	Magnetic field effects on Langmuir probe characteristics . . .	42
3.3.2	The effect of probe reference electrode on I(U) Characteristics	44
3.4	Experimental probe I(U) characteristics	46
3.4.1	Comparison of experimental and theoretically modeled probe I(U) characteristics	47
3.4.2	Correction factors for determining electron saturation current	49
4	Global Discharge Model for Cylindrical and Conical Hollow Cathode	53
4.1	Global discharge model	54
4.2	Global model formulation	55
4.2.1	Spatial plasma density	56
4.2.2	Effective plasma length and the average electron temperature	58
4.2.3	Peak plasma density	60
4.3	Experimental and Modeling results	61
4.4	Overall scope of the global discharge model	66
5	Magnetic Field Effects on Direct-Current Hollow Cathode Discharge	69
5.1	DC discharge breakdown and sustenance	70
5.1.1	Paschen relation for discharge sustenance	72
5.2	Magnetic field effects on discharge sustenance	74
5.2.1	Secondary electron emission from cylindrical hollow cathode surface	75
5.2.2	Secondary electron emission yield from an oblique cathode sheath	78
5.2.3	Cathode fall characteristics in presence of magnetic field . .	79
5.3	Results and Discussion	81

6	Radial Characteristic of Hollow Cathode produced Magnetized Plasma Column	85
6.1	Ionization mechanism inside cylindrical and conical hollow cathode	86
6.2	Radial plasma characteristics in the downstream region	89
6.2.1	Radial plasma characteristics of a cylindrical hollow cathode source	89
6.2.2	Radial plasma characteristics of a conical hollow cathode source	91
6.3	Phenomenological model: Radial plasma properties	93
6.4	Results and Discussion	96
7	Elongated Plasma production using Magnetized Hollow Cathode	99
7.1	The discharge circuit model	100
7.2	Experimental results	103
7.3	Phenomenological model of a magnetized plasma column	105
7.3.1	Model to determine the length of magnetized plasma column	107
7.4	Results and Discussion	109
8	Conclusions and Future Scope	113
8.1	Summary and conclusion	113
8.2	Future Scope	115
	Bibliography	117

List of Figures

1.1	Schematic of a low pressure DC discharge in an electrical discharge tube.	5
1.2	Voltage-Current characteristics of a low-pressure DC discharge. . . .	6
1.3	Different dark and intense regions that constitutes an ideal DC glow discharge using plane parallel electrodes.	7
1.4	Ideal glow discharge pattern between a planar anode and a hollow cylindrical cathode.	8
1.5	Schematic showing the hollow cathode effect inside the cylindrical cathode cavity.	9
1.6	Schematic of a Hall effect thruster.	13
1.7	(a): Schematic of a Penning trap. (b): Schematic showing the use of cylindrical hollow cathode in different magnetron configuration. . .	13
1.8	(a): Schematic showing the plasma pattern for a hollow cathode discharge in absence of B-field. (b): Schematic showing the effects of cross-field drifts on the plasma pattern in an axially magnetized hollow cathode.	14
2.1	(a): Schematic showing the electric field in a hollow cathode device. (b): Particle current at the respective electrodes.	20
2.2	(a): Schematic showing the electrons gyrating back to the cathode surface under the influence of tangential magnetic field at the cylindrical hollow cathode. (b): Schematic showing the oblique magnetic field at tapered hollow cathode surface.	21
2.3	(a): Schematic showing the path of primary electrons in a magnetized plasma column formed using a cylindrical hollow cathode with axially placed constricted anode. (b): Schematic showing the path of primary electrons in a magnetized plasma column formed using a conical hollow cathode with axially placed constricted anode. . . .	22

2.4	Cylindrical HC plasma source, #1: Hollow cathode (HC), #2: Anode, #3: floating cylinder, #4: Teflon rings, #5: Perspex flange, #6: Gas feed port, #7: Electrode supply terminal, #8: Teflon flange, #9: PEEK insulation cap, #10: HC connection point, #11: Anode connection point, #12: floating metallic rings, #13: Ceramic bushes.	24
2.5	Conical HC plasma source, #1: Hollow cathode (HC), #2: Anode, #3: floating cylinder, #4: Teflon ring, #5: SS flange, #6: Gas feed port, #7: Electrode supply terminal, #8: Teflon flange, #9: Ceramic insulators, #10: Ceramic isolator.	24
2.6	Electrical discharge circuit with current limiting resistance $R_L = 500\Omega$, $R_1 = 200\Omega$, $R_2 = 5k\Omega$, and current measuring resistance $R_M = 20\Omega$	25
2.7	Schematic of experimental linear device, PG=Absolute pressure Gauge, TMP=turbo-molecular pump, S= Plasma source, EC= Extension chamber, LD= Linear device, LP= Langmuir Probe. The enlarged view indicates the arrangement of plasma source in the experimental device and LP arrangement for axial plasma measurement inside the source.	26
2.8	(a): Axial B-field profile in the system for coil current ~ 100 A. (b) Radial profile of B-field at the location of plasma source for coil current ~ 100 A.	27
2.9	(a): Extension chamber (i.e. EC) equipped with cylindrical Langmuir probe. (b): Schematic showing the radial probe movement across the plasma column.	29
2.10	Schematic diagram for Langmuir probe (LP) measurement circuit, DAQ= Data acquisition, OP-AMP = Operation amplifier.	29
2.11	(a): The probe current due to noise signals recorded by the probe circuit in absence of plasma for a given sweep of the voltage bias. (b): Comparison of calibrated and uncalibrated probe I(U) traces.	30
3.1	(a): Schematic of cylindrical Langmuir probe setup. (b): Current-voltage characteristics of a cylindrical Langmuir probe, floating potential V_f , plasma potential V_p	34

3.2	(a): Typical current-voltage characteristics of a single Langmuir probe, floating potential V_f , plasma potential V_p . (b) Ideal current-voltage characteristics of a Langmuir probe with planar, cylindrical and spherical probe geometries.	35
3.3	Ideal current-voltage characteristics of a cylindrical Langmuir probe for known values of n_e , T_e and V_p	39
3.4	Electron current $I_e(U)$ collected by a cylindrical Langmuir probe in a plasma with single and two temperature electron population. . . .	40
3.5	(a): Electron current collected by a cylindrical Langmuir probe biased at plasma potential in unmagnetized plasma. (b): Electron current collected by a cylindrical Langmuir probe biased at plasma potential in a magnetized plasma.	42
3.6	(a): $I(U)$ characteristics of a cylindrical Langmuir probe in a magnetized and unmagnetized case. (b): Electron current collected by a cylindrical Langmuir probe in a magnetized and unmagnetized case.	43
3.7	(a): Cylindrical probe measurements where probe reference is in partial contact with bulk plasma. (b): Electrical analogy of the probe current for the case where probe reference is in partial contact with bulk plasma.	44
3.8	(a): Effect of probe reference on $I(U)$ characteristics of a cylindrical Langmuir probe. (b): Effect of probe reference on electron current collected by a cylindrical Langmuir probe. The Red curve corresponds to a case when probe reference is in good contact with bulk plasma.	45
3.9	(a): Cylindrical probe measurements where probe reference is in partial contact with bulk plasma. (b): Discharge and diffusion currents, (i.e. I_{dis} and I_{diff}) measured over a range of axial B-field. . .	46
3.10	(a): Measured probe $I(U)$ characteristics inside hollow cathode source. (b): Measured electron to ion saturation current ratios from the $I(U)$ traces along the axis of hollow cathode cavity.	47
3.11	Comparison of experimental and theoretical probe $I(U)$ characteristics of a cylindrical Langmuir probe.	48

3.12 (a): Correction factor corresponding to the difference in the measured and actual plasma potential along the axis of hollow cathode cavity. (b): Magnetic correction factor along the axis of hollow cathode cavity.	49
3.13 Corrected electron to ion saturation current ratios along the axis of hollow cathode cavity.	50
4.1 Overview of the global discharge model.	54
4.2 Cylindrical and conical plasma volume with peak plasma density n_0 , plasma radius R_p and plasma length L_p inside respective HC cavities.	55
4.3 (a): Contour plot showing normalized spatial density profile inside cylindrical HC. (b): The contour plot showing normalized spatial density profile inside conical HC.	57
4.4 Generalized particle balance relation showing the variation of T_e versus product $n_g\Lambda$ for Maxwellian electrons in Argon.	59
4.5 (a): Effect of neutral gas pressure on discharge power. (b): Effect of neutral gas pressure on discharge voltage and discharge current across the discharge electrodes. Triangle represents the experimental data for the case of conical HC whereas circles represent the data for cylindrical case.	62
4.6 (a): Axial plasma parameters inside respective HC cavities. (b): Plasma density and potential indicating the Boltzmann distribution inside the source cavities.	63
4.7 Axial profile of normalized plasma density inside HC cavity. The scattered data points represents the experimental values of plasma density which have been normalized with the peak measured density at $z = 0.01$ m.	64
4.8 (a): Average T_e inside HC cavity for experimental values of neutral gas pressure. (b): Peak plasma density n_0 inside HC for experimental values of the product $n_g P_{dis}$. The scattered data points represent the experimental values.	65
4.9 Variation in global plasma parameters as a function of apex angle θ or HC geometry under fixed discharge condition (i.e discharge power = 145 W and pressure = 1.4 Pa).	67

5.1	Townsend avalanche process in the breakdown of a neutral gas. . . .	70
5.2	Typical Paschen characteristic curve showing the relationship between breakdown voltage V_b , operating pressure p and electrode separation L	72
5.3	Cathode fall region after the discharge is established.	73
5.4	(a): Paschen like characteristics for discharge sustenance using Argon gas. (b): Cathode sheath thickness " d " estimated from the characteristic curve for the experimental values of discharge voltage V_{dis} , $\gamma_{se} \approx \epsilon_c/V_{dis}$ and neutral gas pressure for cylindrical HC source.	74
5.5	(a): Effect of transverse magnetic field on the trajectories of secondary electrons emitted from solid cylindrical cathode. (b): Effect of transverse magnetic field on the trajectories of secondary electrons emitted from hollow cylindrical cathode.	76
5.6	Cathode recapture probabilities as a function of axial magnetic field for different neutral gas pressure.	77
5.7	(a): Effect of tangential B-field on the flux of secondary electrons from cylindrical HC surface. (b): Effect of tangential B-field on the secondary electron emission yield.	77
5.8	(a): Phenomenology to show the effect of oblique B-field on the flux of secondary electrons from HC surface. (b): Effect of oblique angle θ on the secondary electron emission yield.	78
5.9	The Paschen relation indicating the effect of magnetic field on the cathode fall characteristics of an Argon discharge.	80
5.10	(a): Variation in discharge current at 1.4 Pa with an axial magnetic field. (b): Variation in discharge voltage at 1.4 Pa with an axial magnetic field.	80
5.11	(a): Discharge voltage as a function of axial magnetic field for a range of neutral gas pressure. (b): Discharge current as a function of axial magnetic field for a range of neutral gas.	82
5.12	(a): Cathode fall thickness as a function of axial magnetic field for a range of neutral gas pressure. (b): Secondary electron emission yield as a function of axial magnetic field for a range of neutral gas pressure.	83

5.13	(a): Cathode fall thickness as a function of an axial magnetic field at a neutral gas pressure 1.4 Pa. (b): Effective secondary electron emission yield as a function of an axial magnetic field at a neutral gas pressure of 1.4 Pa. All the parameters are normalized with the respective experimental values in absence of magnetic field.	83
6.1	(a): Possible ionization mechanism inside a cylindrical hollow cathode cavity in presence of axial magnetic field. (b): Possible ionization mechanism inside a conical hollow cathode cavity in presence of axial magnetic field.	87
6.2	(a): Optical image and intensity map of magnetized plasma column by a cylindrical HC source at 17.16 mT and operating pressure of 1.4 Pa. (b): Optical image and intensity map of magnetized plasma column by a conical HC source at 17.16 mT and operating pressure of 1.4 Pa.	88
6.3	(a): Radial profile of ion density n_+ , bulk electron temperature T_{eb} and plasma potential ϕ at axial location $z = 30$ cm for cylindrical HC plasma source. (b) Radial profile of hot electron density n_{eh} / temperature T_{eh} at axial location $z = 30$ cm for cylindrical HC plasma source.	90
6.4	Radial profile of ion density n_+ , bulk electron temperature T_{eb} and plasma potential ϕ at axial location $z = 30$ cm for conical HC plasma source.	92
6.5	(a): Radial density profile for cylindrical HC for boundary conditions and experimental parameters given in table 6.1. (b): Radial density profile for conical HC for experimental parameters given in table 6.2. The scattered points represents the experimental values for each case.	97
7.1	(a): Electrical analogy of a discharge between anode "A" and cathode "C". (b): Equivalent electrical circuit of a DC discharge in equilibrium state.	100

7.2	(a): Effect of axial B-field on cathode and anode potential measured w.r.t the ground. (b): Plasma potential in the discharge as a function of axial magnetic field for a neutral gas pressure of 1.4 Pa.	101
7.3	(a): Effect of axial B-field on anode sheath resistance R_A and cathode sheath resistance R_C . (b): Effect of axial B-field on Plasma resistance R_p .	102
7.4	(a): Axial plasma potential along the axis of the magnetized plasma column at neutral gas pressure of 1.4 Pa. (b): Axial plasma density along the axis of the magnetized plasma column at neutral gas pressure of 1.4 Pa.	103
7.5	Axial profile of hot and bulk electron populations for axial B-field 11.66 mT and at neutral gas pressure of 1.4 Pa.	104
7.6	(a): Primary electron current paths in presence of magnetic field. (b): Plasma equivalent impedance circuit in presence of magnetic field with $R_A =$ Anode sheath resistance, $R_p =$ Plasma resistance having parallel components $R_{ } \approx$ (ie R1,R2,R3...R9) and perpendicular components $R_{\perp} \approx$ (ie Ra,Rb,Rc...Rz), $R_C =$ Cathode sheath resistance.	105
7.7	Effect of magnetic field on plasma resistance R_p and plasma conductivity σ_{dc} at a neutral gas pressure of 1.4 Pa.	107
7.8	Perpendicular and parallel electron fluxes entering and leaving magnetized plasma tube assuming the plasma column to be homogeneous. Here r_a is the radius of anode which is assumed to be the radius of magnetized plasma column and L_p is the length of magnetized plasma column.	108
7.9	(a): The estimated length of plasma column for different axial magnetic field strengths. (b): Side view of magnetized plasma column at a neutral gas pressure of 1.4 Pa.	109

List of Tables

6.1	Experimental values J_e , ϕ_0 , n_0 and T_e for different axial magnetic field in the case of cylindrical HC.	95
6.2	Experimental values ϕ_0 , n_0 and S_0 for different axial magnetic field in the case of conical HC.	95

1

Introduction

In the modern world, plasma manufactured products have entered every household; occupying an inevitable place in our daily lifestyle. From handheld gadgets to efficient lighting, food processing, automobile industries, agricultural, biomedical and in space applications, plasma technologies are widely used. The plasma created by electric discharges are used in a large number of applications such as in the light industry (i.e. in fluorescence lamps, neon discharge tube for advertisements, etc.), as flat plasma display panels (i.e. PDPs) for the new generation of large-area television screens [1–4]. Besides, there are other important applications such as those in the microelectronic industry and in the material processing technology [1–3]. These include surface treatment, etching of surfaces (i.e. for the fabrication of integrated circuits, etc.), plasma polymerization and the deposition of thin protective coatings [1–4].

Electric discharges provide an exceptional mechanism of producing low-temperature plasma in laboratories and also for various industrial applications [1–3]. Popular electric discharges operated with direct current (DC) sources are the magnetron sputtering discharge used for the deposition of metal coatings on the substrates [1, 4–8]. Electric-arc plasmas are used for the synthesizing of nano-particles [9]; while dielectric-barrier discharges are used for treating the food grains, air purification and various environmental applications [10]. The DC discharge combined with a static magnetic field is a key concept behind Hall thrusters used for spacecraft propulsion [11, 12]. In laboratories, DC glow discharge is a popular setup for

carrying dusty plasma experiments [13]; while the thermionic arc [14, 15] and cold cathode discharges [16–18] are well known for producing intense plasma column in linear plasma devices. The performance of these devices strongly depends on the electrical properties of the discharge and intrinsically governed by the shape and the configuration of the discharge electrodes [4, 19, 20]. Analytical / phenomenological modeling of plasma sources can help in the improvement of the performance of these devices [21–23].

Basically an electric discharge refers to ionized gas, produced by setting a strong electric field between a pair of electrodes; resulting in a net electric current passing through the ionized gas [24]. This current is mainly constituted of energetic electrons which provide ohmic heating to the gaseous atoms / molecules and it is responsible for sustaining the discharge plasma [1, 4]. The electric current can be provided employing either direct or the alternating current (AC) source. Discharge produced by low-frequency AC has characteristics similar to that of DC discharge; however at very high frequency, i.e in Radio-Frequency (RF) or Microwave-Frequency (MF) range, the mechanism of plasma production is significantly different [1, 25]. In the case of capacitively coupled RF discharge, the discharge current through the plasma is mainly constituted of electrons; whereas the displacement current flows across the electron free region inside the sheaths formed in the immediate neighborhood of RF electrodes [1, 26]. The RF discharges can be formed using insulating / dielectric electrodes and therefore they are highly popular in microelectronic industries [25]. On the other hand, cold cathode DC discharge requires conducting electrodes that provide secondary electrons for the sustenance of discharge between the electrode gaps [1, 4]. The DC discharges are operated at relatively higher pressures and high operating voltages. Therefore, both current densities, as well as ion bombardment energies at the cathode, are higher which is favorable for the sputtering of target materials [1–4].

The hollow cathode discharge is a special type of DC discharge in which the cathode comprises of a hollow cylinder [1, 4, 19, 27]. Hence the energetic electrons emitting from the cathode are electrostatically confined inside the hollow cavity and undergo pendular oscillations due to multiple reflections from the opposing sheaths at the cathode surface. As a result, significant ionization takes place inside the

hollow cathode, and higher current densities can be sustained at lower operating pressure as compared with planar cathode geometries [19, 27, 28]. Hollow cathodes are widely popular in applications such as high power plasma switches, electron / ion beam sources, for the production of soft x-rays, material deposition and as a source of intense line radiation [4, 19, 29–33]. The efficiency of DC discharge can be enhanced by applying an external magnetic field along the cylindrical cathode [34, 35]. This concept is applied in penning discharges for generating electron beams [36]. The external magnetic field is also applied in magnetron sputtering discharges to achieve a high ionization fraction of the deposition material [7, 8, 37]. The magnetic field not only affects the plasma characteristics inside the source but it also leads to the formation of space charge gradients, allowing positive ion acceleration in Hall thrusters [11, 12]. Therefore the fundamental understanding of magnetized hollow cathode devices requires insight into both plasma dynamics emerging from $\vec{E} \times \vec{B}$ drifts as well as the engineering design of the electrodes which is crucial for achieving improved secondary electron emission yield γ_{se} and plasma extraction from the hollow cathode source.

With the above motivation, the present thesis focuses on a detailed investigation on the performance of cold hollow cathode discharge operated with an axial magnetic field. In particular, two distinct hollow cathodes consisting of; (1): cylindrical geometry with an axially placed constricted anode and (2): cone-shaped hollow cathode with a constricted anode at its minor end is considered in the study. In the case of cylindrical hollow cathode, the magnet field lines are tangential at the cathode surface; whereas in the conical case, the magnetic field line is at an oblique angle with regard to the cathode surface. It is found that the above hollow cathode geometries have a phenomenal effect on the discharge performance as well as it affects the plasma properties in the downstream region outside the source. A comprehensive part of the thesis is devoted to the development of phenomenological models which is crucial for understanding various physical aspects observed in the experiments. The analytical models are also crucial for better design and optimization of plasma sources, besides explaining the spatial distribution of plasma properties resulting from each source. Furthermore, the experimental data is also helpful for the benchmarking of the formulated models.

In particular the thesis attempts to find; how the magnetic field influences the secondary electron emission yield from the hollow cathode surface and how the primary electron current constituted through the discharge affects the radial and axial plasma properties in the downstream plasma region. The methodology used in the entire study is based on experimental measurement of plasma parameters both inside and outside the cylindrical and cone-shaped hollow cathodes; and using the experimental information to build analytical models for predicting the qualitative performance of the source. Some of the major outcomes from the thesis are the development of a phenomenological formula for approximating the length of the downstream magnetized plasma column; use of the gross electrical discharge parameters for the estimation of cathode fall characteristics and predicting the discharge behavior; development of an electric probe analysis technique for isolated magnetized plasma column; and development of global models for the interpretation of radial and axial plasma characteristics for cylindrical and conical hollow cathode sources.

Before we discuss the overall contents of the thesis; a brief introduction to DC discharge including the hollow cathode effect is presented in section-1.1. The role of secondary electrons in the sustenance of DC discharges is presented in section-1.2. Section-1.3 introduces the effect of the magnetic field in DC hollow cathode sources. Finally, a brief content of the thesis is presented in section-1.4.

1.1 DC Electric Discharge

The simplest form of DC discharge comprising of a pair of circular metallic electrodes inside a gas-filled glass chamber is shown in figure 1.1. The discharge is created by applying high voltage DC between the two electrodes, giving rise to cascaded multiplication of electrons by impact ionization with the background neutrals present in the discharge gap [24]. Typically, a few hundred volts are required between the respective electrodes to sustain the discharge at an operating pressure range between 10 mTorr to 10 Torr. DC discharges are highly reliable and easily reproducible sources of plasmas in laboratories. Hence these discharges were the subject of intensive research for almost 200 years [4]. The DC discharge

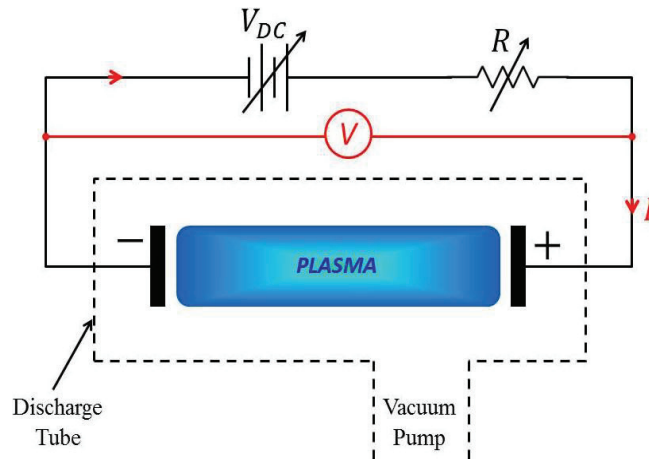


Figure 1.1: Schematic of a low pressure DC discharge in an electrical discharge tube.

and in particular the glow discharge is important historically, both for studying the basic plasma physics as well as for the various industrial applications; where the DC discharges are employed as a source of weakly ionized plasmas [1, 2, 4].

The electric discharge varies over several orders of magnitude in current and voltage ranging from 10 – 1000’s of volts. By varying the current limiting resistor R , one can control the applied voltage V across the electrodes; correspondingly the current I through the discharge also varies. An extensive literature on Voltage-Current (i.e. $V - I$) characteristics of a DC discharge can be found in various research articles [1, 4, 24]. As shown in figure 1.2, the $V - I$ characteristic curve can be classified into three main regimes i.e. Dark discharge, Glow discharge and Arc discharge [24].

The region between A and E is considered as *dark discharge* as the entire discharge remains invisible except for the corona and the breakdown spark region. The dark region is primarily sustained by cosmic rays producing electrons and ions, which are quickly absorbed at the electrode. This region is characterized by high voltage with relatively low current. As the current increases, a luminous glow can be seen with a significant drop in the voltage across the discharge gap, which is popularly known as *glow discharge region*. A negative resistance can be seen as the increase in discharge current is associated with a fall in the voltage (E to F). However in

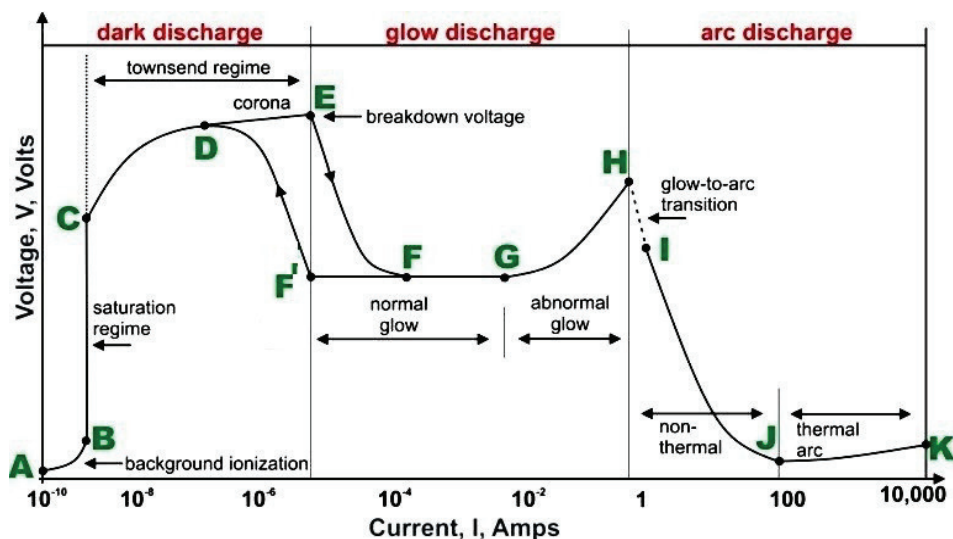


Figure 1.2: Voltage-Current characteristics of a low-pressure DC discharge.

the abnormal glow region (G to H), once again the voltage across the electrode increases with current. Beyond the abnormal glow, there is a rapid transition into the *arc region*, where the discharge current increases tremendously which can be only limited by the external current limiting resistance in the discharge circuit.

1.1.1 Basics of a DC glow discharge

The glow discharge plasma is important for plasma production at low gas pressure. In this regime, the electron energy-densities are enough to produce visible light by recombination and excitation collisions [1, 2, 4, 24]. The gap between the electrodes is categorized into successive regions of luminous and dark spaces as illustrated in figure 1.3.

It can be seen that the entire voltage applied between the discharge gap is dropped near the cathode. This region is identified as a cathode dark space, the electrons can hardly reach the cathode surface; as a result, a space charge of positive ions / or sheath is formed at the cathode surface. An opposing effect can be seen near the positive electrode; where electrons are concentrated to shield the positive potential at the anode. Sometime anode glow can be seen as a bright region that appears just in front of the anode (i.e. at the boundary of anode sheath). In cer-

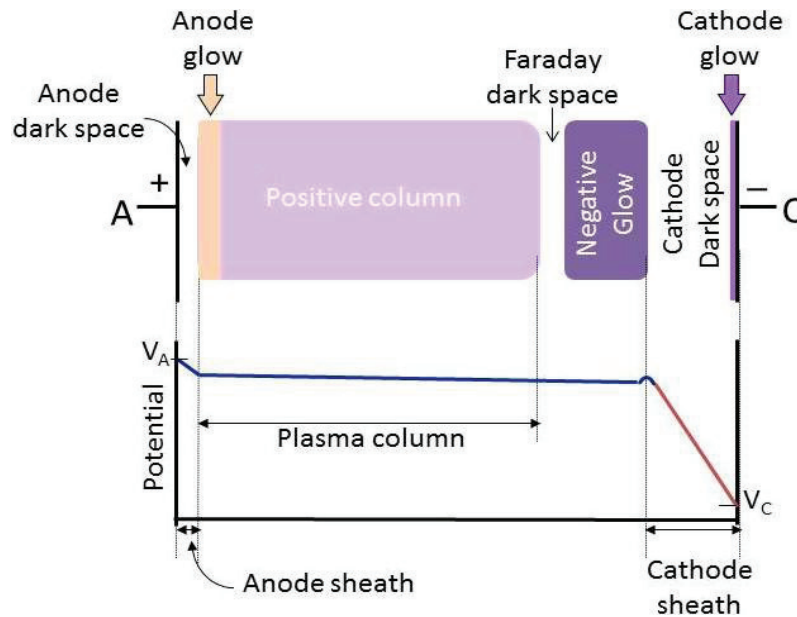


Figure 1.3: Different dark and intense regions that constitutes an ideal DC glow discharge using plane parallel electrodes.

tain low-pressure DC discharges with a constricted anode and relatively large size cathode, the anodic glow is clearly observed surrounding the anode surface [38, 39]. Sometimes it is visually difficult to differentiate the anode glow region and positive column, however, the anodic glow is slightly more intense than the positive column.

The plasma column is almost electric field-free region, and it is often referred to as the positive column as it is nearly at the same potential as the anode. It is important to note that the anode must be slightly positive w.r.t the positive column in order to maintain the flow of current. The region between the positive column and the cathode fall region has bright and dark spaces which are regarded as negative glow and Faraday dark space respectively. The positive column acts as a conducting path between the negative glow region and the anode. Sometimes a double layer plasma structure is also formed near the anode. But since the voltage drop in this region is small, it plays a very little role in the overall discharge dynamics [1, 4].

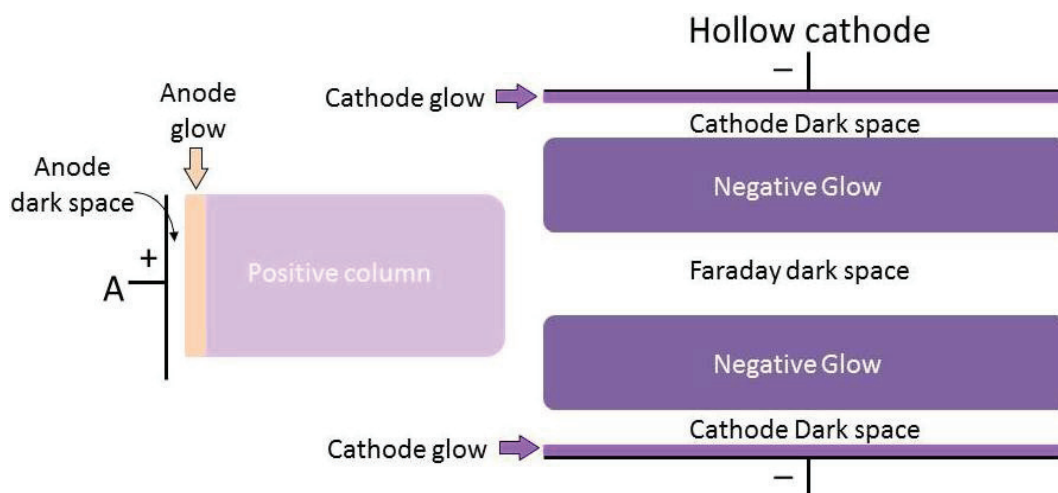


Figure 1.4: Ideal glow discharge pattern between a planar anode and a hollow cylindrical cathode.

1.1.2 Effect of Hollow Cathode geometry

If the planar cathode is replaced by a large area hollow cathode, then the cathode sheath region, the negative glow and the Faraday dark space are localized inside the hollow cathode as illustrated in figure 1.4. If the anode is placed outside the hollow cathode, then the positive column fills the region between the anode and the hollow cathode (HC). The glow discharge pattern with the positioning of the anode (i.e. anode being remote / center of the hollow cathode / at one end of HC axis) also depends on the relative area of HC w.r.t the anode and the aspect ratio (i.e. HC length / HC diameter) of the hollow cathode as well as the operating pressure.

In figure 1.5 a typical case of hollow cathode having length L much larger than its diameter D (i.e. $L \gg D$) is shown. In this case, the negative glow formed uniformly inside the inner surface of the cathode overlaps. This gives rise to an intense electric field dominated region inside the hollow cathode. Therefore the secondary electrons emerging due to positive ion bombardment at the cathode surface are electro-statically trapped inside the hollow cathode and undergo pendular oscillations between the diametrically opposing sheaths. As a result, sufficient excitation of neutral atoms/molecules is seen inside the hollow cavity. This effect is known as Hollow Cathode Effect and the discharge operating in this mode is conventionally

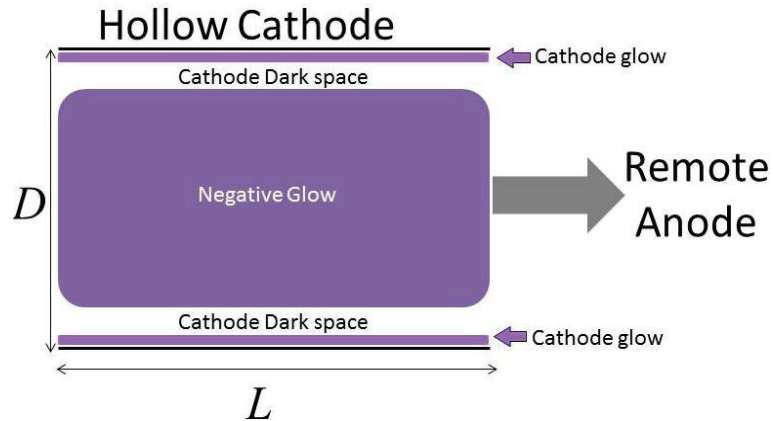


Figure 1.5: Schematic showing the hollow cathode effect inside the cylindrical cathode cavity.

termed as a hollow cathode discharge [1, 4, 19, 30, 31, 40]. The geometry and position of the anode in a hollow cathode device may vary depending on the type of application and requirement, but the basic mechanism governing the hollow cathode effect is still preserved. The hollow cathode discharges have been extensively studied in the past due to higher ionization efficiency at low operating pressures as compared to ordinary glow discharges produced using planar electrodes [19, 27, 28].

1.2 Sustenance of the DC discharge and role of secondary electrons

In a steady-state condition, DC discharge is mainly sustained by a balance between the generation of electron-ion pairs produced via electron impact ionization inside the discharge gap and subsequent loss of electron-ion pairs at the plasma boundary [1, 4]. The ionization that takes place within the positive column is compensated by losses due to recombination and diffusion to the chamber walls. However, the relative importance of these processes depends on external parameters such as shape and configuration of the discharge electrodes, neutral gas pressure, external magnetic field and the operating voltage.

The positive column is the main part of the plasma column and there exists a

weak electric field \vec{E} in this region, just sufficient to ensure the current continuity by electrons (i.e. also referred as *Primary electrons*). If \vec{J} is the discharge current density in the plasma column and \vec{E} is the driving electric field, then product $\vec{J} \cdot \vec{E}$ is the electric power deposited per unit volume inside the plasma column. If R_p is the dynamic plasma resistance, the power absorbed in the plasma column can be related with ohmic heating as; $I_{dis}^2 R_p = \int_v (\vec{J} \cdot \vec{E}) dv$. Here the discharge current density \vec{J} and the driving electric field \vec{E} are expressed as [1, 4];

$$J = en\sqrt{\mu_e \nu_{iz} \varepsilon_T} \quad (1.1)$$

$$E = \sqrt{\frac{\nu_{iz}}{\mu_e} \varepsilon_T} \quad (1.2)$$

In both the above equations; n is the density of current carrying primary electrons, μ_e is the electron mobility, ν_{iz} is the frequency of ionization and ε_T is the total energy loss associated with the particle interaction and transport [1, 4].

In a DC discharge the electrons are resistively heated due to the flow of current in presence of constant electric field between the discharge plates. The energy corresponding to $\vec{J} \cdot \vec{E}$ gained by electrons is transferred in to excitation and ionization of the background gas neutrals [1, 4, 24]. The main source of these electrons is the cathode, which emits the secondary electrons via the process of thermionic, photo-electric or energetic charge/neutral particles bombardment at the cathode surface. In cold-cathode DC discharge, the secondary electrons are produced by the bombardment of positive ions at energies almost equivalent to the cathode fall voltage [4]. After releasing from the cathode, these secondary electrons undergo ionizing collisions with the background atoms, producing electron and ion pair along the discharge length. A self-sustenance condition is reached when a minimal number of positive ions created in the discharge give rise to the nascent secondary electron from the cathode when the ions strike the cathode surface.

The number of electron-ion pairs created by each secondary electron that interacts with the background neutrals is given as [1, 4];

$$N = \frac{V_c}{\varepsilon_c} \quad (1.3)$$

In above equation, V_c is the cathode fall voltage drop and ε_c is the collisional energy loss per electron-ion pair created with the flow of secondary electrons into the plasma. If γ_{se} is the net yield of secondary electrons that are primarily responsible in the ionization process; hence one can write a self-sustenance condition as $N\gamma_{se} = 1$. Thus the secondary electron emission yield γ_{se} under a given discharge condition can be related to the experimentally measured cathode fall voltage V_c as [1, 4];

$$\gamma_{se} = \frac{\varepsilon_c}{V_c} \quad (1.4)$$

1.3 Magnetic field effect in DC discharge

Both magnetic field strength, as well as the direction of \vec{B} w.r.t the local electric field \vec{E} , plays an important role in DC discharge characteristics.

When an external magnetic field is introduced, the current constituted through the discharge is modified because the charge particles, mainly the electrons, tend to spiral around the magnetic field lines under the influence of $e(\vec{V} \times \vec{B})$ force. The *gyro frequency* or *cyclotron frequency* is expressed as [41];

$$\omega_c = \frac{eB}{m} \quad (1.5)$$

In above equation ω_c is cyclotron frequency, e , B and m are respectively the electric charge, magnetic field strength and the mass of the particle.

The radius of the gyration is an important scale length in magnetized plasmas, it is also termed as *Gyro radius* or *Larmour radius* and is defined as;

$$\rho_l = \frac{V_\perp}{\omega_c} \quad (1.6)$$

In above equation, ρ_l is the gyro radius and V_\perp is the perpendicular velocity component of the charge particle. The ions are highly massive (i.e. for e.g. Ar⁺ ion to electron mass ratio is $m_i/m_e = 40 \times 1837$), hence their gyro radius is very large as compared to that of electrons. In most case ion larmor radius turns out to be significantly larger than the discharge dimensions; in such cases ions are usually

considered as un-magnetized species.

The ρ_l can be compared with the system length such as electrode gap length, cathode fall thickness, particle mean free paths, etc; to assess whether the magnetic field in the system is important or not. A plasma is considered to be weakly / partially magnetized even if only the electrons in the system are magnetized and scaling lengths follows [41]; $\rho_l \ll \lambda_e$ and $\omega_{ce} \gg \nu_m$. In planar DC discharges, the axial magnetic field reduces the radial loss of plasma electrons to the side walls; hence the discharge efficiency can be enhanced. However, the effective collisions between the charge particles and the background neutrals can reduce the overall effect of the magnetic field.

If the local electric field \vec{E} and magnetic field \vec{B} are perpendicular to each other, the charged particles experience a $\vec{E} \times \vec{B}$ drift in the system, which is expressed as [41];

$$V_E = \frac{\vec{E} \times \vec{B}}{B^2} \quad (1.7)$$

In above equation, V_E is basically the drift velocity of guiding center and its direction is perpendicular to both \vec{E} and \vec{B} . In above expression, the velocity of guiding center does not depend on the mass and charge of the particle. Therefore, both electrons and ions experience $\vec{E} \times \vec{B}$ drift in the same direction.

1.3.1 Application of $\vec{E} \times \vec{B}$ drifts in DC discharge devices

The effect of $\vec{E} \times \vec{B}$ drifts is popularly recognized in cross-field electric discharges such as *Hall effect thrusters* shown in figure 1.6; where $\vec{E} \times \vec{B}$ effect gives rise to the creation of localized electric field responsible for positive ion acceleration [11, 12].

Figure 1.7 shows a few configuration of cylindrical cathode sources having magnetic field applied in the direction perpendicular to the local electric field. Magnetically enhanced hollow cathode devices are popular source of production of intense charge particle beams [36] and also for ion deposition on substrates [1, 4–8]. *Penning traps* and *Magnetrons* employ cylindrical hollow cathodes in presence of axial magnetic field. Penning traps operate at very low neutral gas pressures (i.e. 0.01 mPa - 0.01

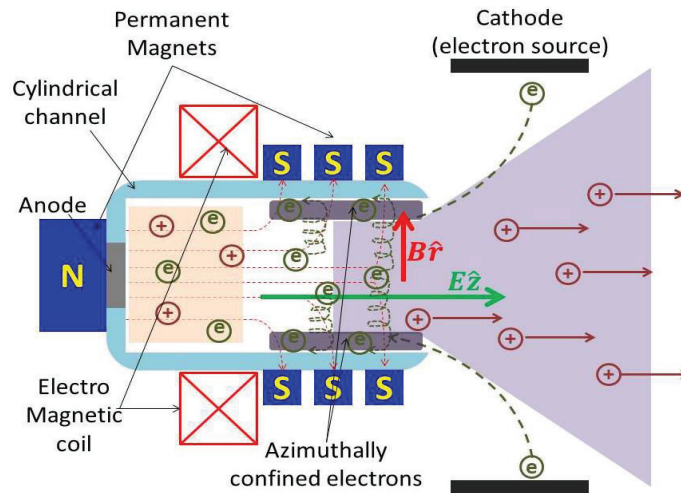


Figure 1.6: Schematic of a Hall effect thruster.

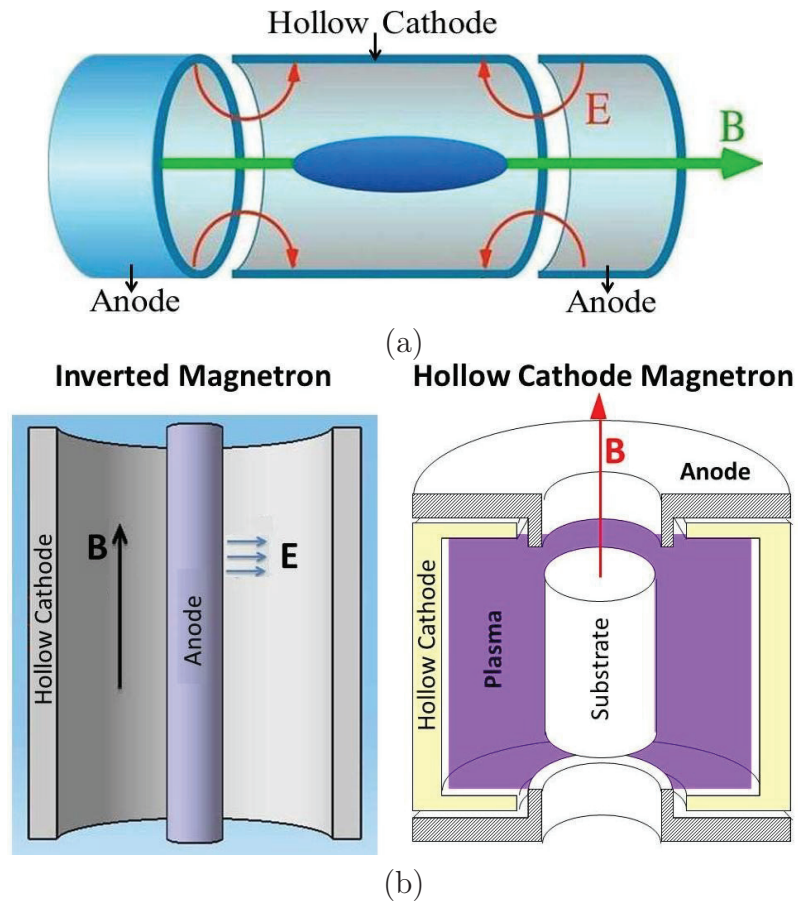


Figure 1.7: (a): Schematic of a Penning trap. (b): Schematic showing the use of cylindrical hollow cathode in different magnetron configuration.

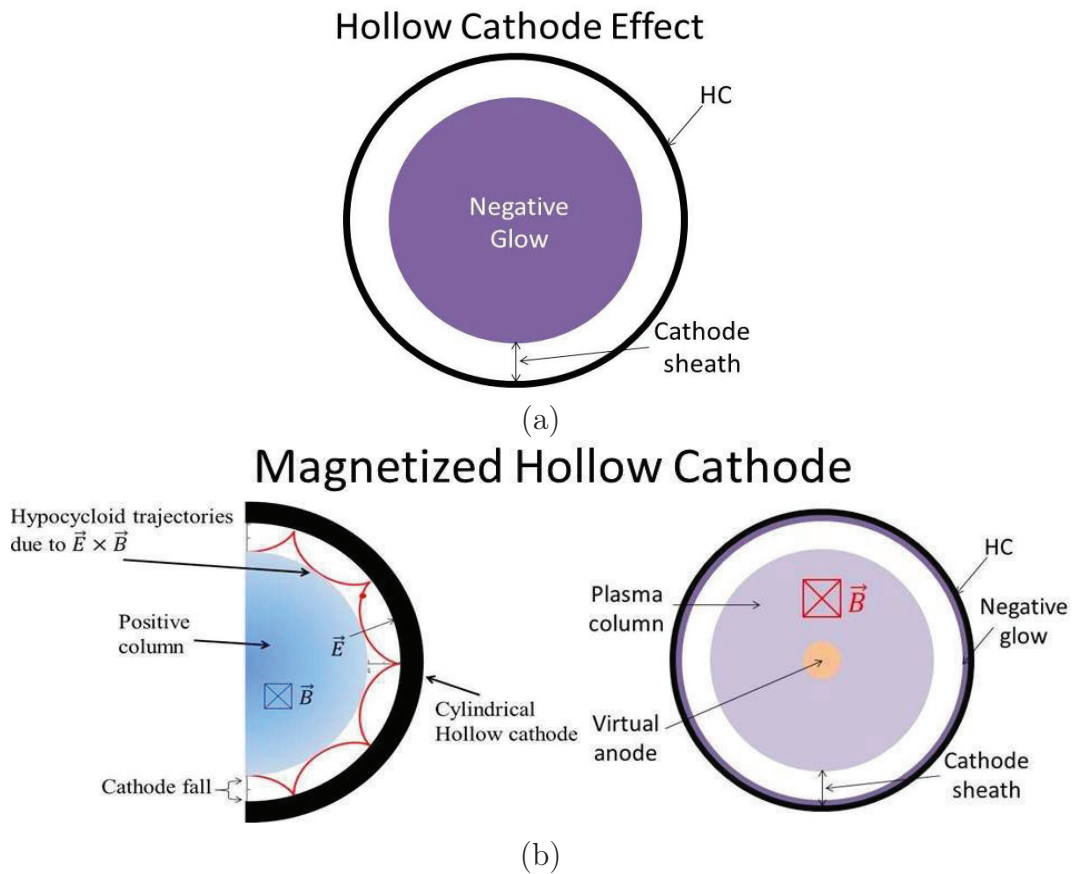


Figure 1.8: (a): Schematic showing the plasma pattern for a hollow cathode discharge in absence of B -field. (b): Schematic showing the effects of cross-field drifts on the plasma pattern in an axially magnetized hollow cathode.

Pa) and are conventionally used as a source of electrons. Whereas, in magnetron devices, the $\vec{E} \times \vec{B}$ confinement of primary electrons gives rise to intense ionization and sputtering of the cathode target.

1.3.2 Magnetization effects in a hollow cathode device

Consider the case of hollow cathode, in which the magnetic field is applied along the cylindrical axis as shown in figure 1.8. As the negative glow is situated inside the hollow cathode region, it produces a strong radial electric field from the centre towards the cathode surface as indicated in figure 1.8a. As a result the electrons experience a strong $\vec{E} \times \vec{B}$ drift parallel to the cathode surface as shown in figure 1.8b.

In unmagnetized case, electrons undergo pendular oscillations inside the hollow cavity; however due to presence of axial magnetic field, the electrons tend to orbit in cycloidal trajectories along the hollow cathode surface in a closed loop. Therefore, as shown in figure 1.8b the negative glow region get localized in the vicinity of the cathode surface and consequently the hollow cathode effect vanishes. A virtual anode is usually formed at the axis of the hollow cathode due to presence of magnetic field. Furthermore the plasma column in presence of an axially magnetized hollow cathode is sustained by primary electrons that constitute the discharge current.

1.4 Thesis outline

In the present research, the combined effect of the magnetic field and hollow cathode geometry on the characteristics of a DC discharge has been investigated. Chapter 2 describes the cylindrical and conical hollow cathode plasma sources that have been developed for the present study. This chapter presents the overall description of the experimental apparatus which includes; Plasma sources, a Linear vacuum vessel, an Electrical discharge circuit and a Langmuir probe measurement circuit used for plasma diagnostics. Chapter 3 gives a comprehensive description on Langmuir probe diagnostics in a magnetized plasma. The overall effect of the magnetic field and discharge configuration on the measured probe $I(U)$ traces has been discussed and a methodology to extract the reliable plasma parameters in concern to the present experimental scenario has been proposed. Chapter 4 investigates the effect of neutral gas pressure on the characteristics of cylindrical and conical hollow cathode source in absence of magnetic field. In this chapter, along with the experiments a global model formulation has been introduced to study the basic plasma characteristic of each source. This chapter also highlights the importance of the global model as a source design tool, as it correlates the measured plasma properties with the source geometry and experimental conditions. Chapter 5 highlights the importance of secondary electron emission in sustaining a DC discharge. This chapter provides an in-depth investigation on the effect of the axial magnetic field and hollow cathode geometry on secondary electron emission yield. Also,

the overall effect of the magnetic field and neutral gas pressure on the cathode fall characteristics has been discussed with the help of experimental measurements and phenomenological modeling. In chapter 6, the effect of hollow cathode geometry on the radial characteristics of a magnetized plasma column has been presented. In this chapter, with the help of experiments in cylindrical and conical plasma source, a phenomenological model has been formulated which considers the effect of tangential and oblique magnetic field on the ionization phenomenology inside each cathode cavity. In Chapter 7, considering the electrical analogy of the discharge, the role of current carrying primary electrons in the formation and sustenance of an elongated magnetized plasma column in a cylindrical hollow cathode source is presented. Finally, chapter 8 summarizes the key results and future scope arising from this research.

2

Experimental Consideration for Hollow Cathode Plasma Source and Diagnostic

This chapter mainly deals with the hollow cathode plasma source and diagnostics that have been designed for the present study. The underlying principle behind the hollow cathode discharge is briefly discussed with emphasis on the role played by the external magnetic field and the electrical discharge circuit on the performance of the source. A section is devoted to instrumentation and calibration of Langmuir probe traces for the characterization of the magnetized plasma column.

Section-2.1 presents a brief overview of the hollow cathode device providing impetus emphasis on the present experimental study. In section-2.2 the engineering details of the hollow cathode plasma sources developed for the experiment are presented. The linear plasma device used for conducting the experiment is described in section-2.3. The instrumentation and electronics for the plasma diagnostics are presented in section-2.4.

2.1 Discharge using hollow cathode devices

Hollow cathode discharge is primarily created using a pair of discharge electrodes in which the cathode is usually a hollow cylinder [1, 4, 19]. The hollow cavity

provides a means for electrostatic confinement of primary ionizing electrons; that results in achieving high current densities at low operating pressures than conventional planar cathodes [19, 42].

In literature, several variants of hollow cathode plasma sources are available, which vary in shape and configuration as per specific application [1, 4, 19, 20, 30, 31, 40]. One of the examples is Pseudo-spark discharge, which consists of a closed cylindrical cathode cavity with a central aperture/hole. This device can produce a well-pinned highly intense electron / ion beams. Pseudo-spark devices are also popular as high power plasma switches and source of x-rays [19, 29]. Hollow cathodes in transverse and longitudinal configurations are also used in a wide range of metal vapor ion lasers producing wavelengths that extend from the infrared to the deep ultra-violet (as short as 224 nm) [1, 19, 40]. Micro hollow cathodes are used for the generation of non-thermal plasmas at atmospheric pressures for environmental applications [43].

The discharge properties of a hollow cathode device depend on several factors such as operating pressure, electrode material, electrode shape / size and discharge gap length [19, 23, 44, 45]. The performance of the discharge also depends on the external driving power source and the magnetic field. Besides the size as well as the position of the anode is also significantly important. In reference [20], it is shown that if the area of the anode is constricted, the discharge gets locally enhanced near the anode. In the presence of a magnetic field, the position of the anode plays a significant role in the discharge properties as it provides the return current to the external power supply through the plasma [20, 46]. Therefore hollow cathode source with axially located constricted anode generally exhibits radial and axial non-uniformity in the discharge [16–18].

When an external magnetic field is imposed on the hollow cathode discharge, it can cause two primary effects. Firstly, the magnetic field reduces the cross-field mobility of current carrying electrons, which helps in collimating the ionizing plasma electrons along the magnetic field lines [17]. Secondly, inside the hollow cavity the magnetic field gives rise to $\vec{E} \times \vec{B}$ drift of electrons by influencing the secondary emission emitted during positive ion bombardment at the cathode [18, 47–51]. In

addition, magnetic field can also influence DC breakdown characteristics by reducing the operating pressure [4, 19, 49–51].

In the present study, the role of the external magnetic field on the performance of a hollow cathode device has been reported. Therefore, the experimental design is motivated towards developing a discharge setup based on a hollow cathode configuration with the following objectives:

1. Producing a stable and elongated plasma column along the axial magnetic field in a linear plasma device.
2. Obtain useful experimental data for benchmarking analytical model developed for optimization of plasma device using hollow cathode discharge.
3. To study the effect of the oblique magnetic field on secondary electron emission yield and its influence on the plasma column.

In line with the above objectives, two different hollow cathode plasma sources have been developed. Before discussing these sources a brief overview of the discharge mechanism is presented.

2.1.1 Hollow Cathode Discharge Mechanism

Figure 2.1a, shows a basic configuration of a hollow cathode discharge. The discharge is sustained through a high voltage DC power supply providing a potential V_{DC} in the range of 100 V to 1 kV between the hollow cathode and the anode. This results in a discharge current I_D flowing along the axial electric field inside the discharge column and perpendicular to the cathode. As a result, the Ohmic heating $I_D^2 R_{plasma}$ is generated which helps in sustaining the discharge [1, 4]. The resistor R_L is usually used to limit the current from growing the discharge into an arc mode, while it can also be used to measure the discharge current in the circuit.

In the figure 2.1a, the axial electric field \vec{E}_z is relatively small as compared to the radial electric field \vec{E}_r inside the cathode cavity. This electric field mainly corresponds to the voltage drop across the cathode sheath, due to which, the positive ions from the plasma bombard the cathode surface with very high kinetic

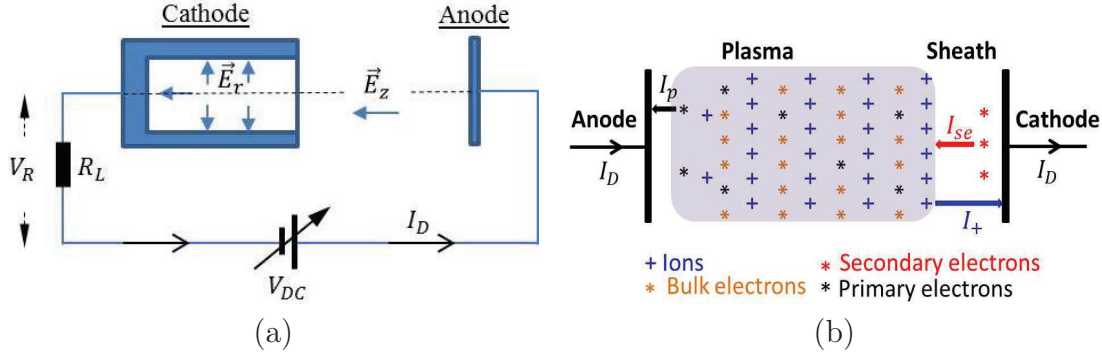


Figure 2.1: (a): Schematic showing the electric field in a hollow cathode device. (b): Particle current at the respective electrodes.

energies and enable the secondary electron emission [1, 19]. The discharge current is mainly constituted of energetic electrons flowing towards the anode and a relatively small fraction of positive ions that are absorbed by the hollow cathode. The difference between the electron and positive ion flux at the respective electrodes is compensated by the emission of secondary electrons from the cathode surface. In absence of external magnetic, these electrons are energetically expelled towards the center of the hollow cathode and subsequently undergo ionizing collision with the background neutrals by reflecting multiple times from the diametrically opposing sheaths inside the hollow cavity [1, 4, 19, 40].

In figure 2.1b, the arrows indicate the direction of individual particle current and I_D flowing through the plasma. The energetic secondary electrons generated at the cathode undergoes multiple ionization, producing the avalanche of electron-ion pair before getting absorbed at the anode. The current continuity through the discharge is maintained by the same amount of opposing charges being emitted and collected at the cathode and anode respectively. The net discharge current I_D through the plasma is expressed as the surface integral of current carrying electron fluxes across the discharge cross-section [1, 4];

$$I_D = \int_s en\sqrt{\mu_e\nu_{iz}\epsilon_T}ds \quad (2.1)$$

In above equation n is the density of current carrying primary electrons, μ_e is the electron mobility, ν_{iz} is the ionization frequency and ϵ_T is the total energy loss

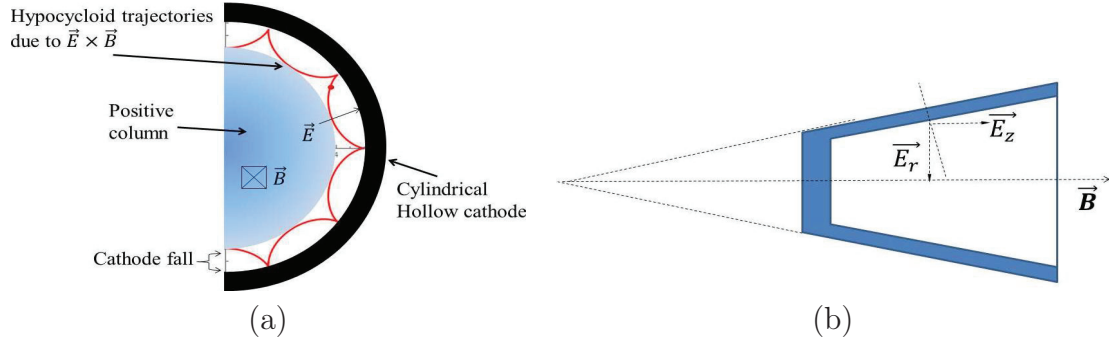


Figure 2.2: (a): Schematic showing the electrons gyrating back to the cathode surface under the influence of tangential magnetic field at the cylindrical hollow cathode. (b): Schematic showing the oblique magnetic field at tapered hollow cathode surface.

associated with the particle interaction and transport [1, 4].

The electrons inside the discharge can be classified as primary electrons and bulk electrons. The primary electrons have elevated temperature and they mainly constitute the discharge current through the plasma [17]. These electrons interact with the background gas atoms and metallic surfaces whereas, the bulk electrons are trapped inside the plasma column by the sheaths at the respective electrodes.

2.1.2 DC hollow cathode discharge in presence of magnetic field

When an external magnetic field is applied along the axis of the hollow cathode; it reduces the radial loss of primary electrons from the discharge [17], reduces secondary electron emission from the cathode surface [18, 47, 49, 52] and also introduces a Hall current inside the hollow cavity [6, 8, 20, 53]. The secondary electrons after emitting from the cathode surface undergo a cycloid trajectory instead of pendular oscillations observed in normal hollow cathode discharge operated without a magnetic field [18, 48]. As shown in schematic figure 2.2a the secondary electrons are azimuthally trapped in a hypocycloidal motion along the direction of $\vec{E} \times \vec{B}$ drift inside the hollow cavity. Some of the electrons gyrate back to the cathode surface and so depending on the experimental conditions, there is

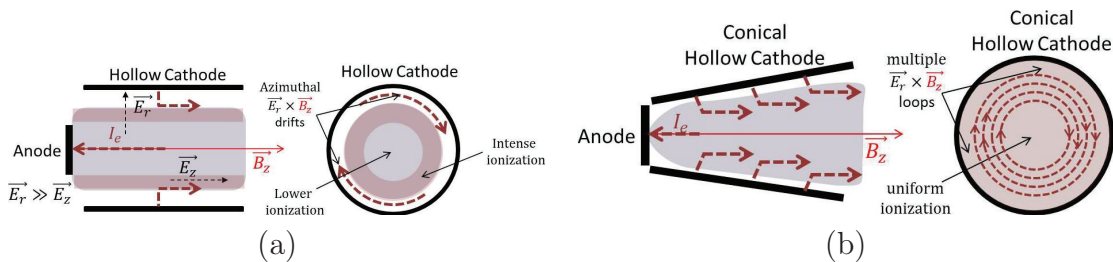


Figure 2.3: (a): Schematic showing the path of primary electrons in a magnetized plasma column formed using a cylindrical hollow cathode with axially placed constricted anode. (b): Schematic showing the path of primary electrons in a magnetized plasma column formed using a conical hollow cathode with axially placed constricted anode.

a finite probability that these electrons are recaptured by the cathode [18, 48, 52]. This cathode recapture reduces the number of secondary electrons participating in the ionization process. As a result, under the effect of magnetic field the net secondary electron emission yield reduces [18, 47–50, 52].

However, if a tapered hollow cathode is applied as shown in figure 2.2b, the axial magnetic field makes an oblique angle with the sheath electric field at the cathode surface [18]. Hence, a component of the electric field \vec{E}_z will be along the direction of B-field, which allows the fraction of secondary electrons to escape the hollow cathode region along the magnetic field lines. Furthermore, the cycloidal trajectory will be evenly distributed at all radial distances for the case of a cone shaped hollow cathode. The performance of the discharge with both oblique and tangential magnetic field for the case of conical and cylindrical hollow cathode geometries are comprehensively discussed in chapter-5 and chapter-6.

2.1.3 Current constituting through the discharge

When the anode is situated inside the hollow cathode as shown in figure 2.3, then the current carrying primary electrons have to flow along the magnetic field lines to reach the anode surface. This is primarily caused because of the reduced mobility of electrons across the magnetic field [1, 8, 17]. The radial diffusion of electrons across the magnetic field will take place by a random walk process to reach the central region. The axial electric field then accelerates these electrons towards the anode.

A schematic is shown in figure 2.3a and 2.3b for the current carrying electrons in the case of the cylindrical and conical hollow cathode. For the conical hollow cathode case, the primary electrons are present at all radial locations as compared to the cylindrical case in which the electrons generally tend to be confined in a single magnetic flux tube adjacent to the cathode surface [6, 8, 18, 19, 53].

2.2 Design and Construction of Hollow Cathode Device

Based on the above concept, two kinds of plasma sources have been designed and installed in a linear plasma device to produce an elongated plasma column in the presence of an axial magnetic field. The plasma sources mainly vary with regard to the shape of the hollow cathode. In one case a cylindrical hollow cathode has been used and in the second case, a tapered hollow cathode is applied (see schematic figure 2.3). In both the plasma sources the anode is situated axially at one end of the hollow cathode, whereas the magnetic field is applied along the axis [18].

In order to constrain the discharge to form inside the hollow cathode region, the cathode is encapsulated inside a floating metallic cylinder that shadows the exterior HC surface from the grounded vacuum vessel. Thus it terminates the electric field lines emerging from the outer HC surface and thereby ensures that the discharge takes place between the inner HC surface and the centrally located anode [17, 18].

The schematic of the cylindrical HC plasma source is shown in figure 2.4. It consists of a hollow cylindrical cathode (HC) having an internal diameter 70 mm, length 100 mm and a tubular anode (A) made from stainless steel (SS304). The outer/inner diameter of the anode tube is 20mm/16 mm. An end cap is attached to this tube which has a 3 mm hole in the center. The anode sits inside the supporting Teflon flange (i.e. part #8), whereas the end cap (diameter 20 mm) is flush to the Teflon surface that defines the active anode area, participating in the discharge. The HC is mounted on the same Teflon flange using two threaded rods and it stays isolated from the Teflon flange with the help of ceramic bushings. The exposed Teflon surface has been shielded by isolated SS-304 rings of varying

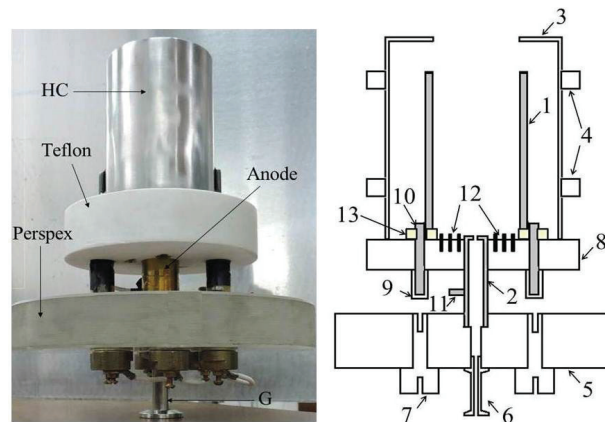


Figure 2.4: Cylindrical HC plasma source, #1: Hollow cathode (HC), #2: Anode, #3: floating cylinder, #4: Teflon rings, #5: Perspex flange, #6: Gas feed port, #7: Electrode supply terminal, #8: Teflon flange, #9: PEEK insulation cap, #10: HC connection point, #11: Anode connection point, #12: floating metallic rings, #13: Ceramic bushes.

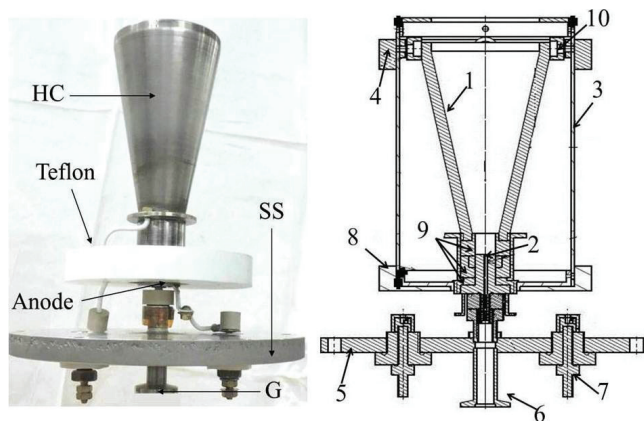


Figure 2.5: Conical HC plasma source, #1: Hollow cathode (HC), #2: Anode, #3: floating cylinder, #4: Teflon ring, #5: SS flange, #6: Gas feed port, #7: Electrode supply terminal, #8: Teflon flange, #9: Ceramic insulators, #10: Ceramic isolator.

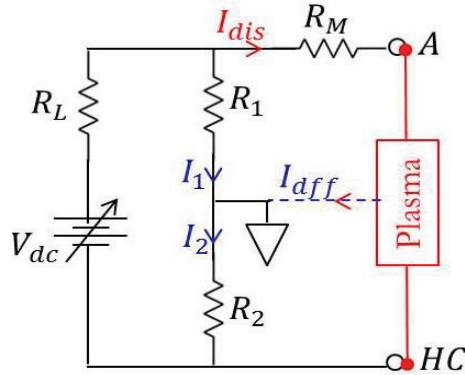


Figure 2.6: Electrical discharge circuit with current limiting resistance $R_L = 500\Omega$, $R_1 = 200\Omega$, $R_2 = 5k\Omega$, and current measuring resistance $R_M = 20\Omega$.

diameter to avoid excessive heating of the Teflon.

The image of the conical hollow cathode plasma source and its internal parts are shown in figure 2.5. It consists of a conical hollow cathode (i.e. part #1) having minor/major radii (i.e. R_i/R_o) 10mm/ 35mm, length 100mm and a planar disk-shaped anode (i.e. part #2) of diameter 20 mm. This planar anode having a 3 mm central hole is sandwiched between two ceramic insulators (i.e. part #9) and it is placed at the minor end of the conical cathode.

In both the above plasma sources, the electrical connections are taken out from the backside of the Teflon flange using insulated cables and the neutral gas in the system is introduced from a 3 mm anode hole.

2.2.1 Electrical Discharge Circuit

The DC discharge is produced using the electrical circuit shown in figure 2.6. In this circuit R_M is the current measuring resistance, V_{dis} is the discharge voltage measured across the floating hollow cathode and the constricted anode. The common point of resistors R_1 and R_2 is connected to the grounded chamber. The series resistor R_L is provided to restrict the discharge from going into an arc mode.

Using the floating discharge circuit in figure 2.6, the diffusion current lost from the bulk plasma to the grounded vessel can be accounted as, $I_{diff} = I_2 - I_1$. Also,

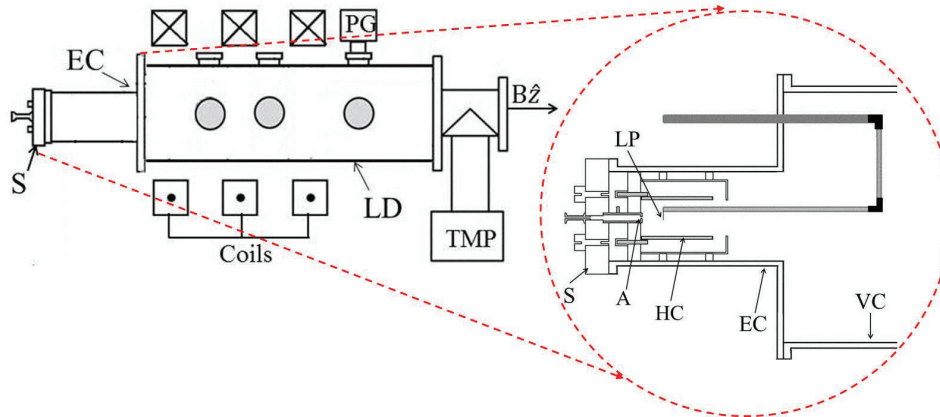


Figure 2.7: Schematic of experimental linear device, PG =Absolute pressure Gauge, TMP =turbo-molecular pump, S = Plasma source, EC = Extension chamber, LD = Linear device, LP = Langmuir Probe. The enlarged view indicates the arrangement of plasma source in the experimental device and LP arrangement for axial plasma measurement inside the source.

individual electrode potential w.r.t grounded vessel can be measured for different experimental conditions.

2.3 Experimental Setup

The experimental setup is shown in figure 2.7. It comprises of a cylindrical vessel made of Stainless steel (SS304) having length 1.5 m and internal diameter 0.3 m. The chamber is equipped with a 700 l/s Pfeiffer turbo molecular pump TMP (Turbo Hipace 700), providing an effective pumping speed of 300 l/s at the vessel. The chamber can be evacuated to a base pressure of 2.5×10^{-5} mbar. This linear vacuum device is equipped with three electromagnet coils. The coils are made by winding copper bus-bars in double pan-cake configuration. These coils are capable to resist the maximum coil current up to 140 A, giving a peak magnetic field approximately 40 mT along the axis of the linear device. In the schematic figure 2.7, the 'dot' and 'X' represents the direction of the coil current to generate axial B-field in the system.

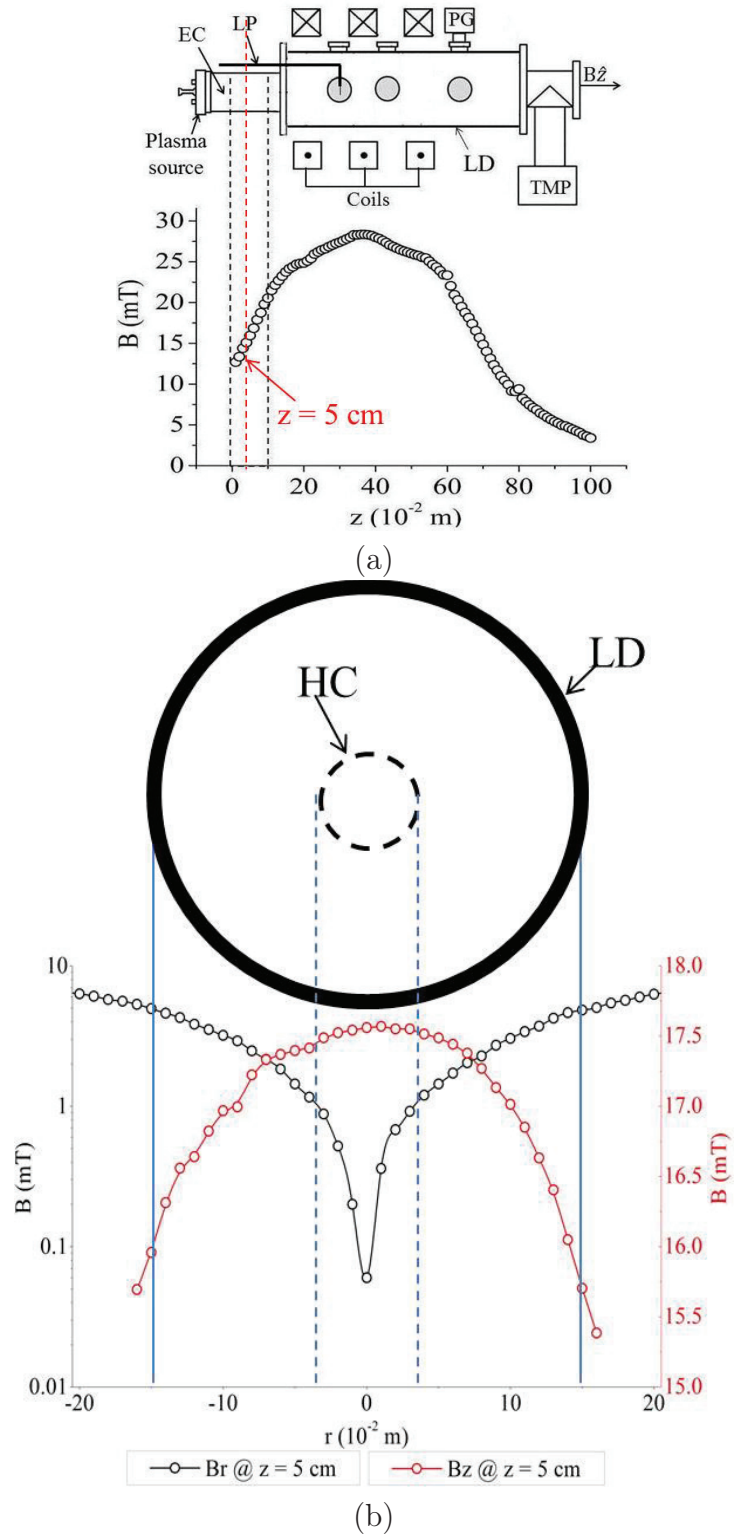


Figure 2.8: (a): Axial B-field profile in the system for coil current ~ 100 A. (b) Radial profile of B-field at the location of plasma source for coil current ~ 100 A.

2.3.1 Linear Device and Magnetic Field Topology

As shown in figure 2.7, the plasma sources are mounted one at a time on the cylindrical linear device inside an extension chamber (i.e. EC, inner diameter ~ 15 cm). In figure 2.8a, the axial magnetic field for the coil current ~ 100 A has a peak B-field ~ 28.6 mT at $z = 40$ cm from the anode. The position of the HC source relative to the magnetic field is indicated by the vertical dashed line. The plasma source is positioned in the low magnetic field region, which allows the discharge to operate at low pressure. In figure 2.8b, the radial as well as axial component of B-field is shown at the source region (i.e. at $z = 5$ cm). It is found that the axial field dominates over the radial field at the location of the HC. Also, the radial variation in B_z is almost negligible across the dimensions of the plasma column / HC diameter.

As indicated in figure 2.7 and figure 2.8a, special feedthrough is designed to insert the cylindrical Langmuir probe for measuring the axial and radial plasma parameters inside the hollow cathode and in the downstream region away from the source. The extension chamber (i.e. EC) equipped with a cylindrical Langmuir probe is shown in figure 2.9a. The spatial movement of the probe is controlled from the backside of the extension chamber. Figure 2.9b highlights the radial movement of a cylindrical probe across the plasma column at an axial distance $z = 30$ cm in figure 2.8a.

2.4 Langmuir probe and measurement circuit

Figure 2.7 and figure 2.9 show the cylindrical Langmuir probe (i.e. LP) arrangement for axial plasma measurements inside the source and in the downstream region. The probe tip is made of tungsten wire having a diameter of 0.25 mm and length 6.0 mm inserted in a ceramic capillary. To allow maximum electron collection, the probe tip is aligned perpendicular to the magnetic field lines [54]. As indicated in figure 2.9b, considering that the discharge is azimuthally symmetric, the radial measurements are performed by moving the probe across the plasma column.

The layout of the probe measurement circuit is shown in figure 2.10. The LP

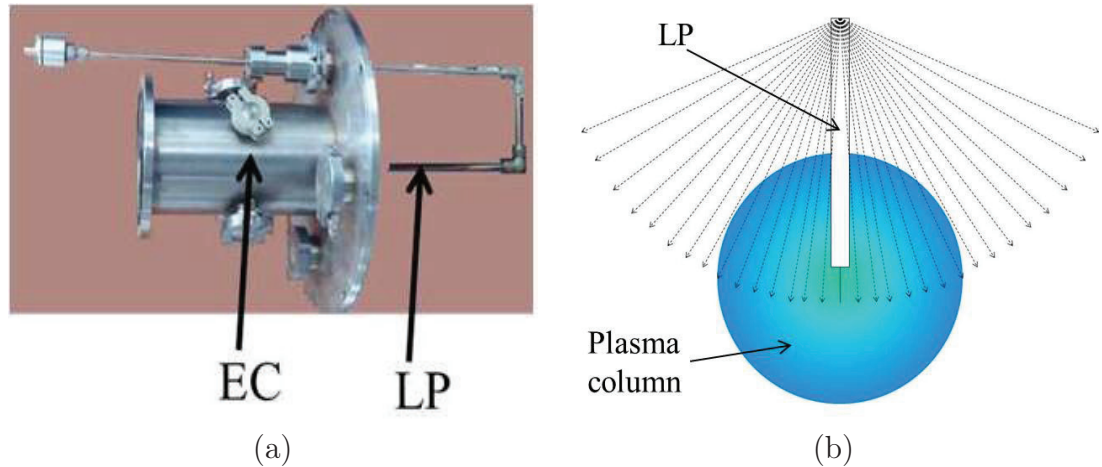


Figure 2.9: (a): Extension chamber (i.e. EC) equipped with cylindrical Langmuir probe. (b): Schematic showing the radial probe movement across the plasma column.

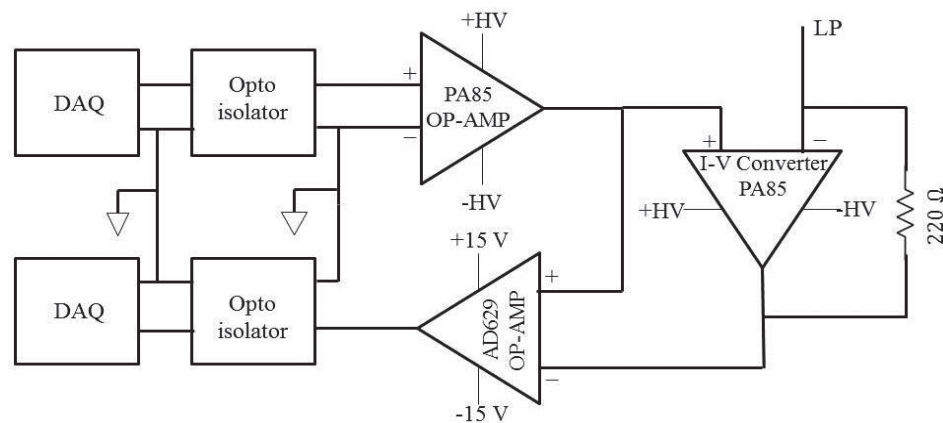


Figure 2.10: Schematic diagram for Langmuir probe (LP) measurement circuit, DAQ= Data acquisition, OP-AMP = Operation amplifier.

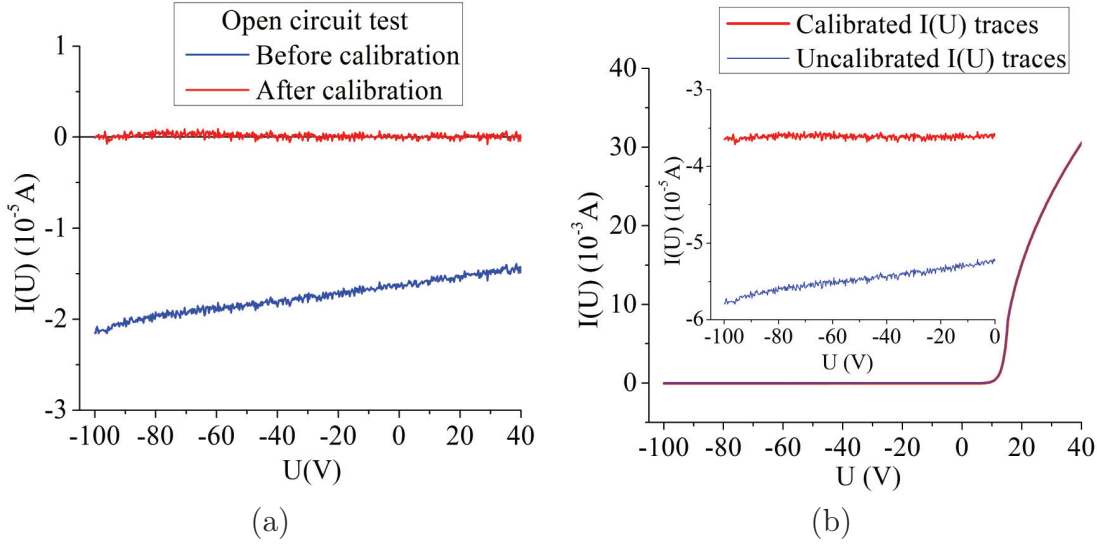


Figure 2.11: (a): The probe current due to noise signals recorded by the probe circuit in absence of plasma for a given sweep of the voltage bias. (b): Comparison of calibrated and uncalibrated probe $I(U)$ traces.

characteristic is obtained by biasing the probe from $U = -100V$ to $U = +40V$ w.r.t the grounded vacuum vessel. The probe bias is provided using an operational amplifier (PA85) in steps of $0.25V$. The probe current $I(U)$ is measured across 220Ω resistor using a current to voltage converter (PA85) and difference amplifier (AD629). The entire data acquisition is done using NI-DAQ which is controlled by Lab-View [54].

2.4.1 Measurement circuit calibration

The probe circuit is calibrated with a known non-inductive resistor $R = 120\text{ k}\Omega$ by applying a voltage sweep through this resistor. The measured current using the probe circuit is in excellent agreement with the calculated current (i.e. $I = U/R$). Also, an open circuit test is performed in the absence of plasma. Ideally, in the absence of plasma, the probe current should be zero. However, in figure 2.11a, we observe a finite open circuit current during application of a voltage sweep $-100V \leq U \leq +40V$ insteps of $0.25V$. These are the noise signals that are sensed by the probe circuit owing to the capacitive loading of the cables connected to the probe. These noise signals are recorded and removed by subtracting it from the final $I(U)$ trace obtained in the presence of plasma. Therefore, as shown in

figure 2.11a, after calibration the current collected by the probe reduces to zero as expected for open circuit test in the absence of plasma. Figure 2.11b compares the measured $I(U)$ traces with and without calibration. It can be seen that without calibration the measured $I(U)$ traces result in the overestimated values of the ion current.

Summary and Conclusion

In summary, this chapter gives the technical details of cylindrical and conical hollow cathode plasma sources; which are designed for the present study. Also, the importance of the floating discharge circuit in sustaining DC plasma in both the above sources is provided. The floating discharge circuit helps to ensure that the discharge in the above plasma sources is sustained in between the respective discharge electrodes and the plasma column stays isolated from the grounded vessel. It has been shown that a cylindrical Langmuir probe is used to characterize the plasma in the above devices. The probe current has been measured with the help of an operational amplifier (PA85) working in a current-voltage conversion mode. Also, the probe measurement circuit is essentially calibrated to ensure the reproducibility of the measured $I(U)$ traces.

3

Langmuir Probe Application in Magnetized Plasma Column

Langmuir probe is an important plasma diagnostic technique that is widely applied in scientific research and a wide range of industrial, space and fusion plasma applications [55, 56]. The technique was originally invented by Sir Irvin Langmuir in 1926-1929 [57, 58]. The main advantage of this technique is that local plasma parameters can be obtained around a small electrode introduced inside the plasma. Since it was introduced, there has been significant progress in the development of this technique to address specific challenges [55, 59–63]. This chapter mainly focuses on the application of the Langmuir probe for characterization of the magnetized plasma column. The primary focus is to evolve a methodology for determining the actual plasma parameters from the measured Langmuir probe characteristics, as it gets modified by the influence of the magnetic field and the probe reference electrode. The important aspect that has been addressed here is the effect on electron collection to the probe for the case where probe reference is in poor / partial contact with the bulk plasma [54].

The chapter is organized as follows: Section-3.1 gives a brief introduction to the Langmuir probe. The basic equations applied for a cylindrical probe is presented in Section-3.2. This section also describes the technique to determine effective electron temperature for the case of two temperature electron population in the discharge. The role of the magnetic field and the reference electrode on the probe

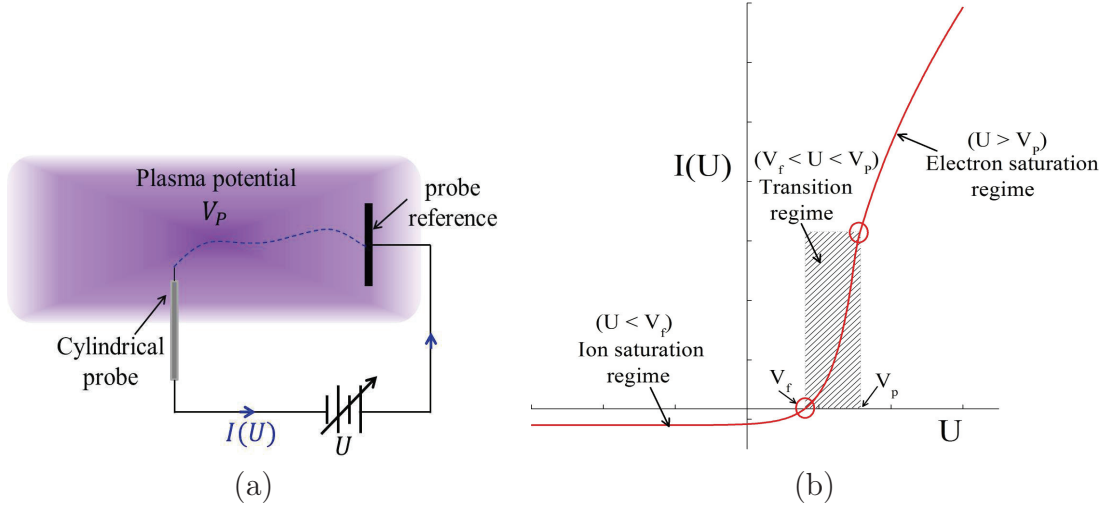


Figure 3.1: (a): Schematic of cylindrical Langmuir probe setup. (b): Current-voltage characteristics of a cylindrical Langmuir probe, floating potential V_f , plasma potential V_p .

characteristics is presented in section 3.3 and its application is demonstrated in Section-3.4.

3.1 Langmuir Probe characteristics

Langmuir probe is usually a piece of conducting electrode / wire inserted in the plasma and an electrical characteristic is obtained by biasing this probe w.r.t a reference electrode, assumed to be in good electrical contact with the plasma. This experimental arrangement is schematically shown in figure 3.1a. The current I constituted through the probe circuit is plotted against the applied potential U as shown in figure 3.1b.

The $I(U)$ characteristics contains all the information of local plasma properties around the probe surface. A number of important plasma parameters like the electron temperature (i.e. T_e), electron / ion density (i.e. n_i/n_e), the space / plasma potential (i.e. V_p) and the electron energy distribution function (i.e. $EEDF$) can be obtained from the analyses of probe $I(U)$ characteristic curve. Figure 3.2a shows a typical current-voltage characteristic of a Langmuir probe. The probe theory is based on the assumption that the electrons are having a Maxwellian

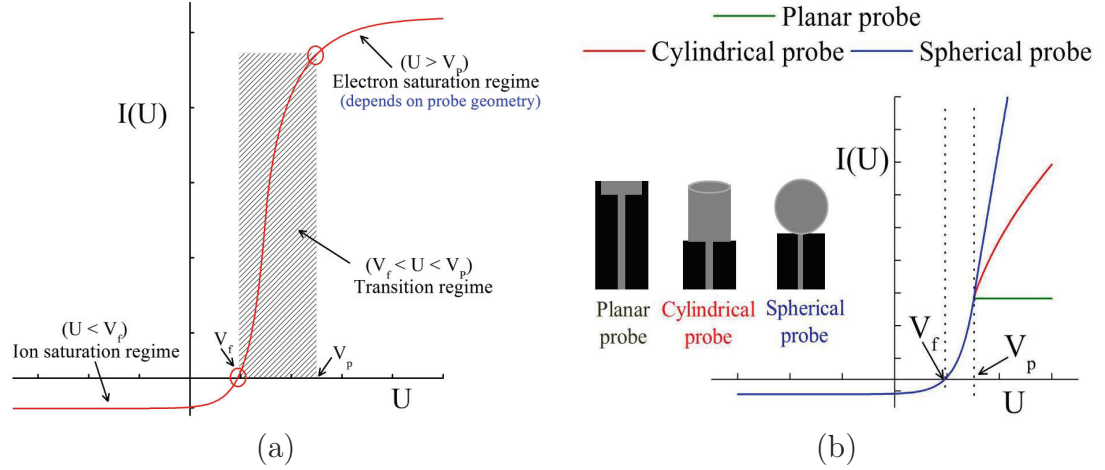


Figure 3.2: (a): Typical current-voltage characteristics of a single Langmuir probe, floating potential V_f , plasma potential V_p . (b) Ideal current-voltage characteristics of a Langmuir probe with planar, cylindrical and spherical probe geometries.

distribution, which is described by a unique temperature T_e . The positive ions also have a Maxwellian distribution but they flow towards the probe with a Bohm velocity (i.e. U_B) at the sheath edge [55, 64].

An isolated probe when inserted in the plasma gets quickly charged to a negative potential relative to the plasma. At equilibrium the net electron flux and the positive ion flux at the probe surface becomes equal (i.e the probe current becomes zero). In this condition the probe is said to be at floating potential V_f as shown in the figure 3.2a. If the probe is biased to a positive value (i.e $U > V_f$), probe current increases exponentially until a saturation value is reached corresponding to the potential $U = V_p$ (i.e. space / plasma potential). At this potential the net electric field between the probe and the plasma vanishes and the net current at the probe is purely constituted by the thermal fluxes of the charge particles. For bias $U > V_p$ the electron current collected by the probe saturates and it is expressed as $I_{esat} = en_e V_{the} A_p$. If $U < V_f$ the probe repels electrons and a saturation value of current is reached for a large negative bias which corresponds to the positive ion saturation, $I_{+sat} = \alpha_0 en_+ U_B A_p$.

The probe current in the transition region corresponding to biased voltage, $V_f <$

$U < V_p$ is mainly due to electrons. The electrons feel a retarding potential in the transition region up to the electron saturation. The electron saturation regime can vary for various probe geometries such as planar, cylindrical or spherical probes as shown in figure 3.2b.

3.2 Single Langmuir probe theory

The basic assumptions behind a single probe applied for a non-thermal laboratory plasma are considered below. Here the theory applies for the case of electropositive, collisionless and un-magnetized plasma [55, 56, 65].

- The bulk plasma is quasi-neutral (i.e. $n_e = n_i$) and plasma volume is infinitely large homogeneous and stationary compared with probe dimension.
- Electron and ions are described by Maxwellian distributions of velocities. Also the kinetic temperature of electrons is much higher than that of ions and neutrals. (i.e. $T_e \gg T_i$ and T_n).
- The electron-neutral collisional mean free path λ_e is much greater than probe radius r_p and electron plasma Debye length λ_D .
- The charged particle fluxes that are collected by the probe only contribute to the probe current $I(U)$. (i.e. no chemical reaction with the probe material or thermal emission is considered.)
- The perturbations introduced by the probe immersed in the plasma are confined to a space charge layer termed as *sheath*. Outside this region, the bulk plasma potential is assumed to be uniform.
- The sheath thickness d is small in comparison with the characteristic probe dimension and therefore sheath edge effects can be neglected.
- The potential profile $U(r)$ around the probe (i.e. between the sheath edge and the probe surface) preserves the symmetry in accordance with the probe geometry and results in a linear electric field in the sheath region.

The relationship between the plasma parameters (i.e. density and temperature) and probe $I(U)$ characteristics depends on several factors such as probe geometry,

relative magnitudes of collision length and plasma Debye length, Larmor radius, probe dimensions, etc.

3.2.1 Cylindrical probe characteristics

The net current collected by the probe is admixture of electron and ion current (i.e. I_e and I_i) which varies according to the applied potential U on the probe surface. Below are the main governing equations that describes the individual current due to electron and positive ions under the effect of retarding electric field around the probe (i.e. $e(U - V_p) > 0$) [55, 65].

$$I_i = \frac{1}{4}en_0\sqrt{\frac{8eT_i}{\pi m_i}}A_p \exp\left(-\frac{e(U - V_p)}{K_B T_i}\right) \quad (3.1)$$

$$I_e = \frac{1}{4}en_0\sqrt{\frac{8eT_e}{\pi m_e}}A_p \exp\left(\frac{e(U - V_p)}{K_B T_e}\right) \quad (3.2)$$

In above equation, V_p is the plasma potential, A_p is the physical probe area, mass of electron is $m_e = 9.109 \times 10^{-31}$ kg, m_i is the mass of ion, electronic charge $e = 1.6 \times 10^{-19}$ C, Boltzmann constant $K_B = 1.38 \times 10^{-23}$ J/K, the equilibrium plasma density is $n_0 = n_i = n_e$, also T_e and T_i are electron and ion temperatures respectively.

The equations governing positive ion and electron current (i.e. 3.1 and 3.2) have an exponential dependence on the bias potential. When $U > V_p$, the positive ions, experience a retarding potential; whereas the electrons experience a retarding potential when $U < V_p$. The rate of exponential fall is different for electrons and positive ions due to disparity in their respective temperatures.

Conventionally the electron current is drawn on the positive scale. The electron current tends to a saturation value for $U > V_p$. A similar effect is seen for the positive ions when the probe is biased at a large negative value with respect to plasma potential $U \ll V_p$. At this condition the ion saturation current (i.e. conventionally plotted in negative y-axis) is expressed by Bohm current, given by

[55, 59–61, 64, 66];

$$I_i = \alpha_0 en_0 \sqrt{\frac{eT_e}{m_i}} A_p \left(\frac{r_s}{r_p} \right) = I_{+sat} \left(\frac{r_s}{r_p} \right) \quad (3.3)$$

Whereas, the electron saturation current is expressed as;

$$I_e = \frac{1}{4} en_0 \sqrt{\frac{8eT_e}{\pi m_e}} A_p F = I_{esat} F \quad (3.4)$$

In above equation 3.3, $\alpha_0 = \exp(-\frac{1}{2})$ is the Bohm coefficient [59, 61, 64, 66]. Also, r_s is the sheath radius, r_p is the probe radius and F is the geometric factor which relates probe bias U with r_p and r_s . For cylindrical Langmuir probe geometric factor F is given as [55, 65];

$$F = \frac{2}{\sqrt{\pi}} \left(\frac{r_s}{r_p} \right) \sqrt{\frac{r_p^2}{r_s^2 - r_p^2} \left| \frac{e(U - V_p)}{K_B T_e} \right|} + \frac{1}{\sqrt{\pi}} \sqrt{\frac{r_s^2 - r_p^2}{r_s^2} \left| \frac{K_B T_e}{e(U - V_p)} \right|} \exp \left(-\frac{r_p^2}{r_s^2 - r_p^2} \left| \frac{e(U - V_p)}{K_B T_e} \right| \right) \quad (3.5)$$

In above equation, for $r_s \gg r_p$ the geometric factor F is approximated as;

$$F = \frac{2}{\sqrt{\pi}} \left(1 + \left| \frac{e(U - V_p)}{K_B T_e} \right| \right)^{\frac{1}{2}} \quad (3.6)$$

Using above formulations, for a given values of values of plasma density n_e , electron temperature T_e and plasma potential V_p it is possible to construct an ideal probe characteristics. The total current collected by the cylindrical Langmuir probe, is the summation of currents due to electrons and positive ions i.e. $I(U) = -I_i(U) + I_e(U)$. As per the conventional approach, the current "from" the probe "to" the plasma (i.e. electron current) is considered positive.

The floating potential V_f is the case when the electron current and ion current collected by the probe balance each other. As shown in figure 3.3, at V_f , the net

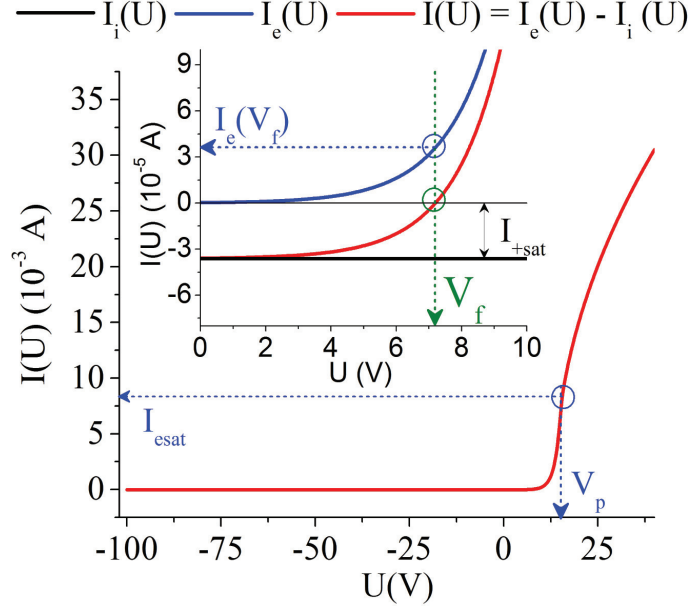


Figure 3.3: Ideal current-voltage characteristics of a cylindrical Langmuir probe for known values of n_e , T_e and V_p .

current drawn by the probe is "zero" (i.e $I(U) = 0$).

$$I_i(V_f) = I_e(V_f) \Leftrightarrow I_{+sat} = I_{esat} \exp\left(-\frac{e(V_f - V_p)}{K_B T_e}\right)$$

$$\alpha_0 e n_0 \sqrt{\frac{e T_e}{m_i}} A_p = \frac{1}{4} e n_0 \sqrt{\frac{8 e T_e}{\pi m_e}} A_p \exp\left(-\frac{e(V_f - V_p)}{K_B T_e}\right)$$

This gives a very important relation between floating potential V_f , plasma potential V_p and electron temperature T_e as;

$$\frac{V_p - V_f}{T_e} = \ln\left(\frac{1}{\alpha_0} \sqrt{\frac{m_i}{2\pi m_e}}\right) \quad (3.7)$$

3.2.2 Probe characteristics for two-temperature electron populations

In some cases, the plasma may have two temperature electron populations. Hence the total electron probe current can be given as $I_e(U) = I_{eh}(U) + I_{eb}(U)$. Here I_{eh} and I_{eb} corresponds to the hot and bulk electron current respectively [55, 63, 66].

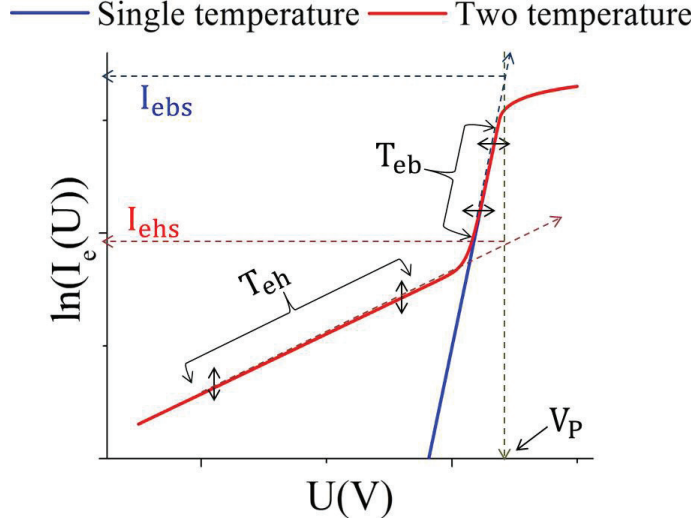


Figure 3.4: Electron current $I_e(U)$ collected by a cylindrical Langmuir probe in a plasma with single and two temperature electron population.

The semi-logarithmic plot of total electron current (i.e. $\ln(I_e(U))$) versus U in figure 3.4 shows two different slopes, which corresponds to the bulk (i.e. T_{eb}) and hot electron (i.e. T_{eh}) temperatures.

An effective electron temperature T_{eff} can be found by taking a harmonic average comprising of n_{eh}/T_{eh} as hot electron density/ temperature and n_{eb}/T_{eb} as bulk electron density/ temperature. Hence the effective electron temperature T_{eff} is given as [54, 63, 66, 67];

$$\frac{1}{T_{eff}} = \frac{1}{T_{eh}} \left(\frac{n_{eh}}{n_{eb} + n_{eh}} \right) + \frac{1}{T_{eb}} \left(\frac{n_{eb}}{n_{eb} + n_{eh}} \right) \quad (3.8)$$

For probe $I(U)$ characteristics with two temperature electron population, at floating potential V_f the net ion current is balanced by the total electron current collected by the probe which includes the current from hot and bulk populations [63, 67]. Also, in the equation of ion current at V_f (i.e. $I_i(V_f)$) the usual Bohm velocity $U_B = \sqrt{\frac{eT_e}{m_i}}$ gets modified as $U_{B^*} = \sqrt{\frac{eT_{eff}}{m_i}}$, where T_{eff} is the effective electron temperature as given in equation 3.8.

$$I_i(V_f) = I_{eh}(V_f) + I_{eb}(V_f)$$

$$\alpha_0 e n_i \sqrt{\frac{e T_{eff}}{m_i}} A_p = \frac{1}{4} e n_{eh} \sqrt{\frac{8 e T_{eh}}{\pi m_e}} A_p \exp\left(-\frac{e(V_f - V_p)}{K_B T_{eh}}\right) + \frac{1}{4} e n_{eb} \sqrt{\frac{8 e T_{eb}}{\pi m_e}} A_p \exp\left(-\frac{e(V_f - V_p)}{K_B T_{eb}}\right)$$

Therefore in the case of two-temperature electron populations, the relation between floating potential V_f , plasma potential V_p and electron temperature T_e depends on the ratio of hot to bulk electron population.

$$\frac{V_p - V_f}{T_{eb}} = \ln\left(\frac{1}{\alpha_0} \sqrt{\frac{m_i}{2\pi m_e}}\right) F\left(\frac{n_{eh}}{n_{eb}}, \frac{T_{eh}}{T_{eb}}, V_p\right) \quad (3.9)$$

In above equation, $F\left(\frac{n_{eh}}{n_{eb}}, \frac{T_{eh}}{T_{eb}}, V_p\right)$ is a complex function which is given as;

$$F\left(\frac{n_{eh}}{n_{eb}}, \frac{T_{eh}}{T_{eb}}, V_p\right) = 1 + \frac{\ln\left(\frac{1 + \frac{n_{eh}}{n_{eb}} \sqrt{\frac{T_{eh}}{T_{eb}}} \exp\left(\frac{V_f - V_p}{T_{eb}} \left(\frac{T_{eh} - T_{eb}}{T_{eh}}\right)\right)}{\sqrt{\frac{T_{eh}}{T_{eb}}} \left(1 + \frac{n_{eh}}{n_{eb}}\right)^{\frac{3}{2}}}\right)}{\frac{\sqrt{\frac{T_{eh}}{T_{eb}} + \frac{n_{eh}}{n_{eb}}}}{\ln\left(\frac{1}{\alpha_0} \sqrt{\frac{m_i}{2\pi m_e}}\right)}}$$

3.3 Magnetic field and reference electrode effects on Langmuir probe characteristics

The Langmuir probe theory described in the previous section assumes an ideal condition in which current collection by the probe is entirely determined by the probe sheath impedance [55]. However in many practical situations, the charge collection by the probe can get affected due to the presence of an external magnetic field or due to additional impedance, if the probe reference electrode is not in good contact with the plasma [54, 55, 62]. These cases are briefly discussed in the following subsections.

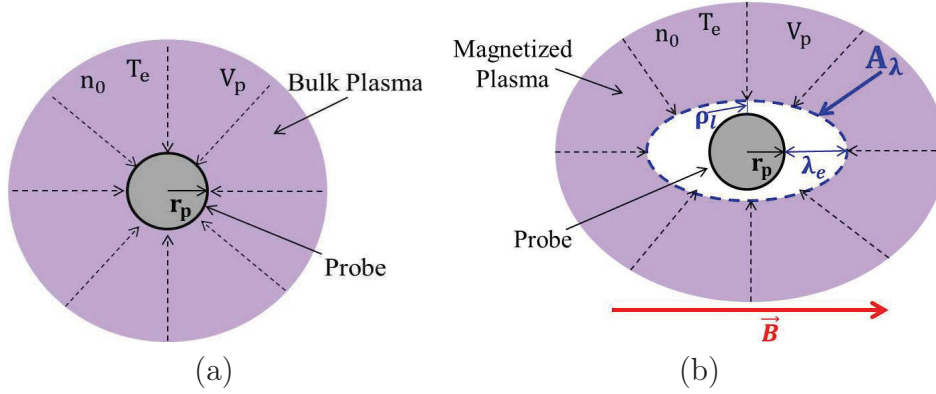


Figure 3.5: (a): Electron current collected by a cylindrical Langmuir probe biased at plasma potential in unmagnetized plasma. (b): Electron current collected by a cylindrical Langmuir probe biased at plasma potential in a magnetized plasma.

3.3.1 Magnetic field effects on Langmuir probe characteristics

In an unmagnetized case, the potential around the probe is isotropic, as a result, there is an isotropic collection of thermal electron current at the probe surface. Therefore, the electron saturation current at plasma potential is given as;

$$I_{sat}|_{B=0} = \frac{1}{4}en_0\sqrt{\frac{8eT_e}{\pi m_e}}A_p \quad (3.10)$$

In presence of a magnetic field, the charge particles are primarily constrained to flow along the magnetic field lines. Due to a significant difference in the mobility of electrons and positive ions across magnetic field lines, an anisotropic distribution of potential is created around the probe. Hence thermal electron collection at the probe surface is also affected. The anisotropy depends on the experimental conditions such as neutral gas pressure and magnetic field strength [55, 62].

As shown in figure 3.5b, there is a formation of a collisionless arbitrary shaped surface A_λ surrounding the current collecting probe under the influence of magnetic field. This depends on the electron neutral mean free path λ_e and electron larmor radius ρ_l along and across the B-field respectively. The thermal electron

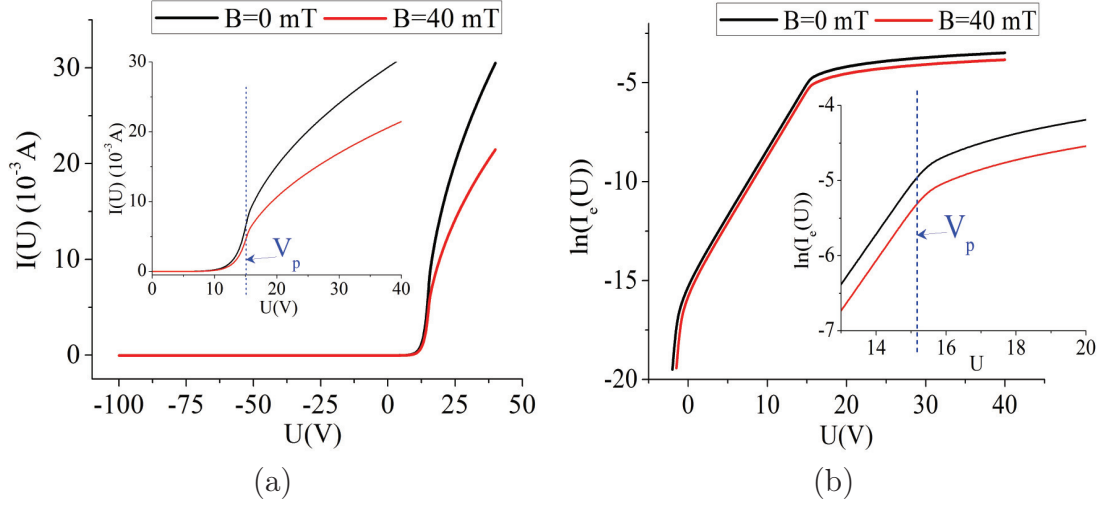


Figure 3.6: (a): $I(U)$ characteristics of a cylindrical Langmuir probe in a magnetized and unmagnetized case. (b): Electron current collected by a cylindrical Langmuir probe in a magnetized and unmagnetized case.

current collected at the surface A_λ is given by [55];

$$I_{esat}|_{A_\lambda} = \frac{1}{4} en_\lambda \sqrt{\frac{8eT_e}{\pi m_e}} A_\lambda \quad (3.11)$$

The current continuity between A_λ and the probe surface gives a very important relation between the probe dimensions, bulk plasma parameters and experimental conditions of neutral gas pressure and external magnetic field (i.e. λ_e and ρ_l).

$$n_\lambda A_\lambda = n_0 A_p \left\{ 1 + \frac{\pi r_p}{8 \lambda_e} \sqrt{1 + \frac{\lambda_e^2}{\rho_l^2}} \right\}^{-1} \quad (3.12)$$

From the above equations 3.10, 3.11 and 3.12, the net thermal electron current at the cylindrical probe surface in presence of magnetic field is given by [55];

$$I_{esat}|_{B \neq 0} = \frac{1}{4} en_0 \sqrt{\frac{8eT_e}{\pi m_e}} A_p \left\{ 1 + \frac{\pi r_p}{8 \lambda_e} \sqrt{1 + \frac{\lambda_e^2}{\rho_l^2}} \right\}^{-1} = \frac{1}{4} en_0 \sqrt{\frac{8eT_e}{\pi m_e}} A_p \beta \quad (3.13)$$

In above equation 3.13, the magnetization factor $\beta = \left\{ 1 + \frac{\pi r_p}{8 \lambda_e} \sqrt{1 + \frac{\lambda_e^2}{\rho_l^2}} \right\}^{-1}$ is related with probe radius r_p , electron larmor radius ρ_l and electron neutral mean

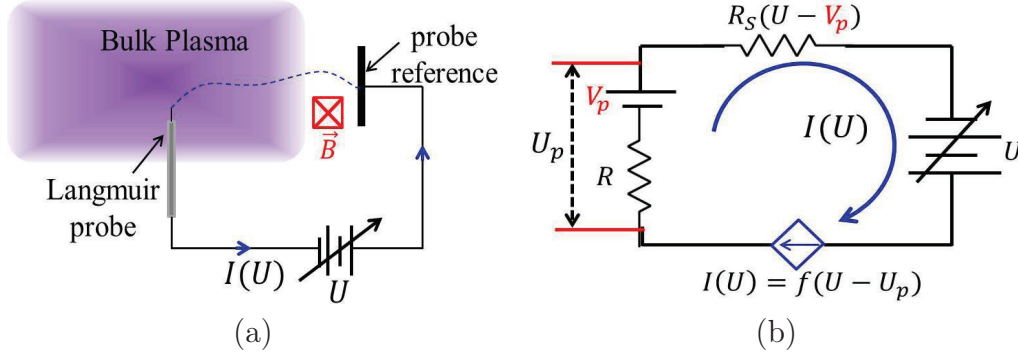


Figure 3.7: (a): Cylindrical probe measurements where probe reference is in partial contact with bulk plasma. (b): Electrical analogy of the probe current for the case where probe reference is in partial contact with bulk plasma.

free path λ_e .

The effect of magnetic field on the probe $I(U)$ characteristics is shown in figure 3.6. It is found that the net electron saturation current reduces in the presence of magnetic field as observed in the semi-logarithmic plot in figure 3.6b. Therefore, the actual electron saturation current in the presence of magnetic field is accounted by introducing a magnetic correction factor β as given in equation 3.13.

3.3.2 The effect of probe reference electrode on $I(U)$ Characteristics

Under certain conditions, the reference electrode may not be in very good contact with the bulk plasma as shown in figure 3.7a. As a result, the current drawn by the probe can be underestimated [54]. This problem can arise from contamination of chamber walls or in the case of floating discharge configurations where the magnetized plasma column remains isolated from the grounded vacuum vessel which is conveniently used as a reference electrode.

In figure 3.7b, the effect of contact resistance of the reference electrode is introduced using an equivalent electrical circuit diagram. Ideally when probe reference is in good contact with plasma, the contact resistance R in probe circuit can be approximated to zero. For this condition (i.e $R = 0$) the net probe current is en-

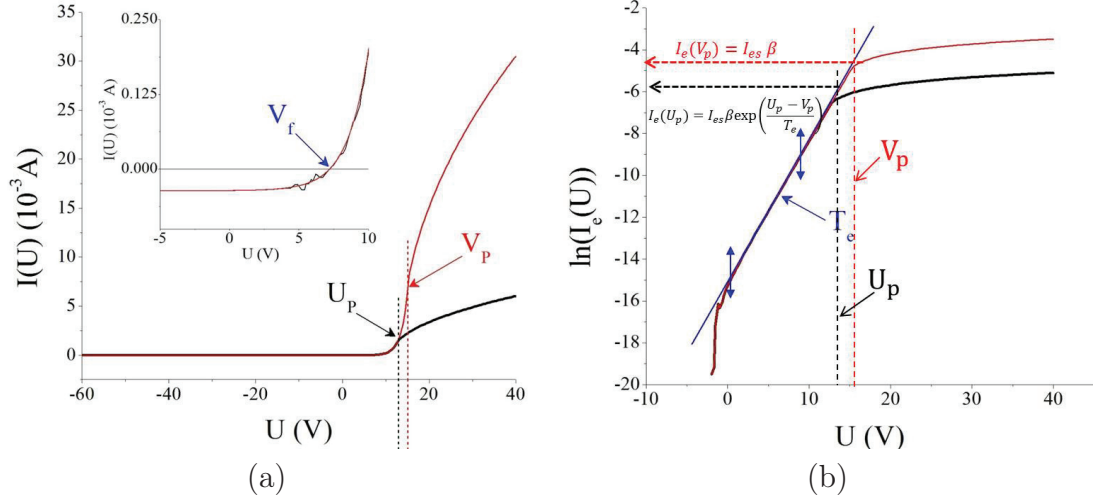


Figure 3.8: (a): Effect of probe reference on $I(U)$ characteristics of a cylindrical Langmuir probe. (b): Effect of probe reference on electron current collected by a cylindrical Langmuir probe. The Red curve corresponds to a case when probe reference is in good contact with bulk plasma.

tirely governed by the plasma sheath resistance R_s which varies accordingly with the applied probe bias. At plasma potential, the sheath resistance $R_s = 0$; hence the net current collected by the probe is the thermal current and a clear electron saturation appears in the measured $I(U)$ characteristics above the plasma potential V_p . However, for a finite value of contact resistance R , the electron saturation appears at a lower value $U_p < V_p$ due to the voltage drop across R . Therefore, $I(U)$ characteristics tends to reach an electron saturation value below the actual plasma potential as shown in figure 3.8a. Hence, electron saturation current is under estimated if the plasma is not in good contact with the reference electrode. The measured $I(U)$ traces in such cases resembles to the probe characteristics obtained from a asymmetric double probe, where electron saturation is observed before actual plasma potential [54, 68, 69].

From figure 3.8b, the relationship between the measured and actual electron saturation current can be given as;

$$I_{sat}|_{measured} = I_{sat}\beta \exp\left(\frac{U_p - V_p}{T_e}\right) \quad (3.14)$$

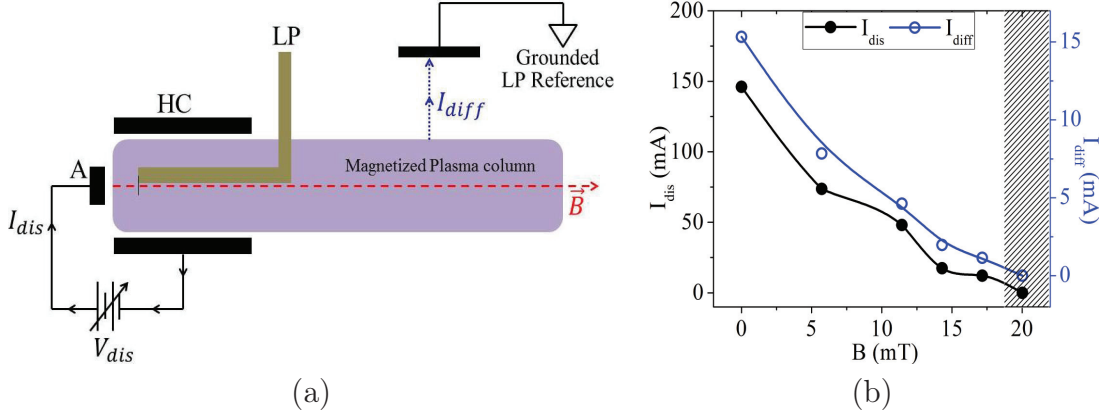


Figure 3.9: (a): Cylindrical probe measurements where probe reference is in partial contact with bulk plasma. (b): Discharge and diffusion currents, (i.e. I_{dis} and I_{diff}) measured over a range of axial B-field.

In above equation β is a magnetization factor whereas the exponential term $\alpha = \exp\left(\frac{U_p - V_p}{T_e}\right)$ is the correction factor corresponding to the reduced electrical conductivity between the bulk plasma and the probe reference.

3.4 Experimental probe $I(U)$ characteristics

A particular experimental case is presented below. The experimental data are taken using a cylindrical probe in the region inside the hollow electrode shown in the schematic figure 3.9a. This refers to the magnetized plasma column created using the cylindrical HC source shown in figure 2.4. The reference electrode is the grounded chamber which is detached from the main plasma column with the help of a voltage divider circuit 2.6. Therefore owing to the floating electrode configuration, the grounded vessel / probe reference collects only the particle current diffused from the bulk plasma to the chamber walls.

Figure 3.9b, shows the diffused particle current (i.e. I_{diff}) lost to the grounded vessel and the corresponding discharge current (i.e. I_{dis}) for a range of magnetic field strength. It is seen that the diffused current through the grounded chamber is nearly 10 – 15 times less than the discharge current. These electrical discharge characteristics indicate that there exist a high impedance between the bulk plasma and the grounded vacuum chamber which is used as the reference electrode for the

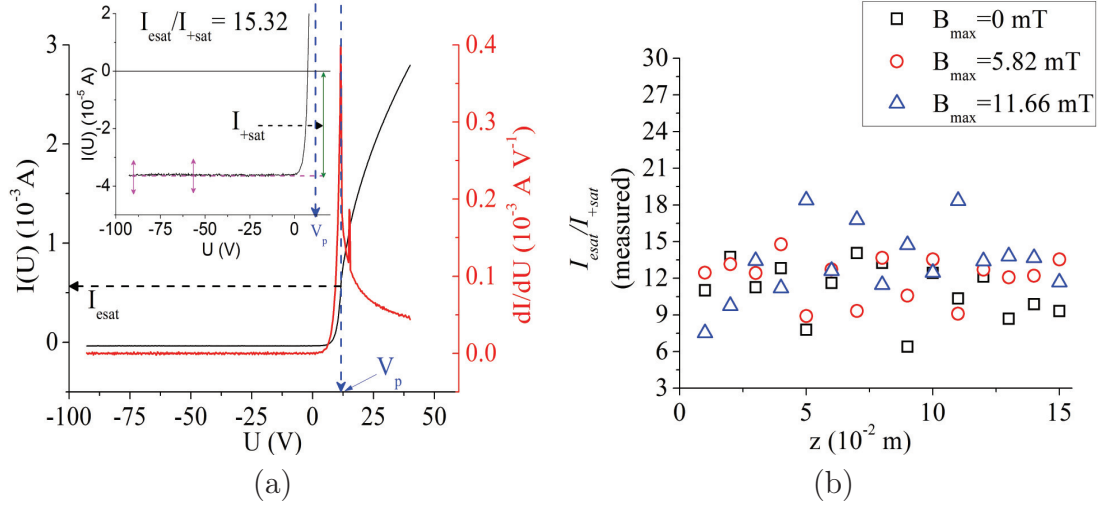


Figure 3.10: (a): Measured probe $I(U)$ characteristics inside hollow cathode source. (b): Measured electron to ion saturation current ratios from the $I(U)$ traces along the axis of hollow cathode cavity.

cylindrical probe.

In figure 3.10a, the electron saturation current appears below actual plasma potential as a result the electron to ion saturation current is underestimated. As shown in figure 3.10b, the ratio of measured electron to ion saturation current for the case of Argon plasma is about 12 – 15 times lower than the expected value ~ 178 . Therefore, conventional probe analysis with the above $I(U)$ traces eventually gives an underestimated values of plasma parameters [54].

3.4.1 Comparison of experimental and theoretically modeled probe $I(U)$ characteristics

To obtain reliable plasma parameters from probe $I(U)$ traces, an iterative approach is adopted. From the measured $I(U)$ characteristics, values of plasma density (i.e. from ion saturation current), electron temperature and floating potential is first estimated following the conventional method of probe analysis [54, 60, 66]. Thereafter, using equation 3.9, the expected value of plasma potential V_p is numerically solved. These initial values of plasma parameters are substituted in the model to generate a theoretical $I(U)$ curve for the cylindrical probe. This is shown in fig-

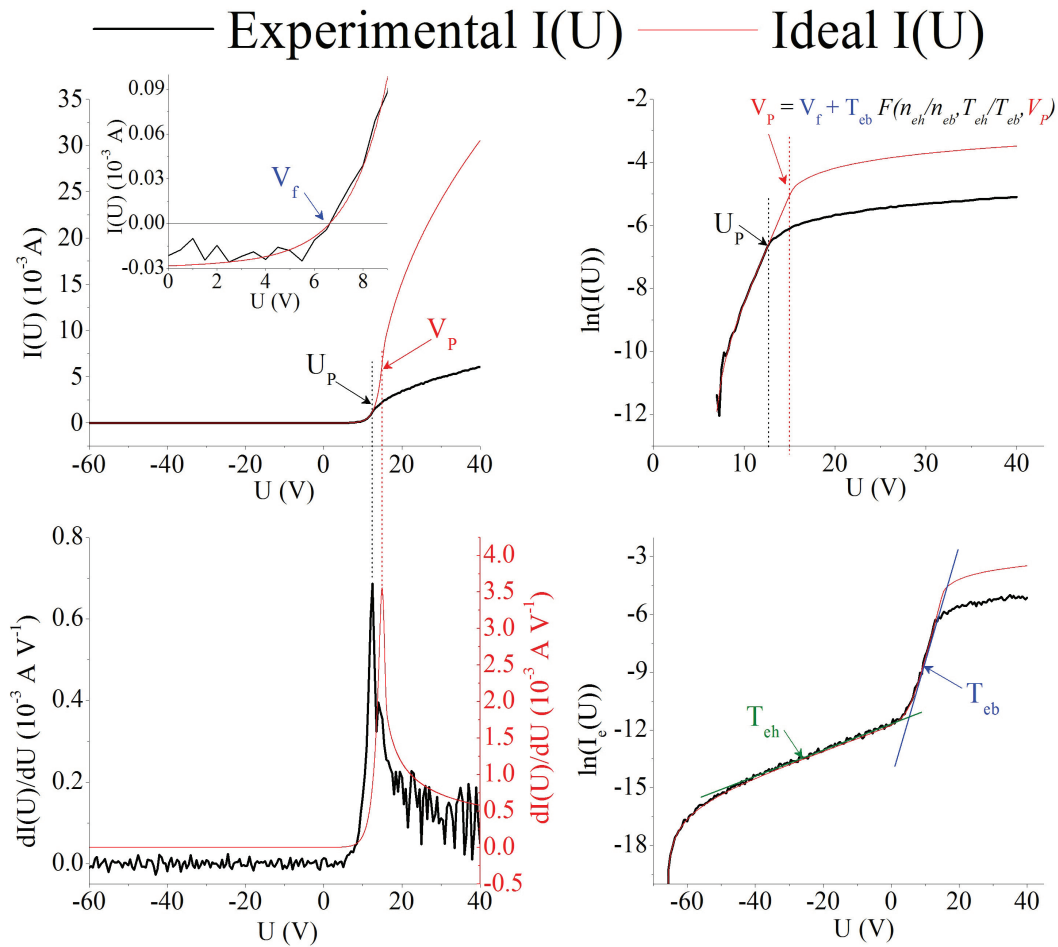


Figure 3.11: Comparison of experimental and theoretical probe $I(U)$ characteristics of a cylindrical Langmuir probe.

ure 3.11. It can be observed that the experimental and theoretical curve deviates significantly in electron saturation regime.

The comparison between experimental and theoretical curves enables us to find the appropriate correction factors for the particular experimental conditions to account for the actual plasma parameters using a cylindrical probe.

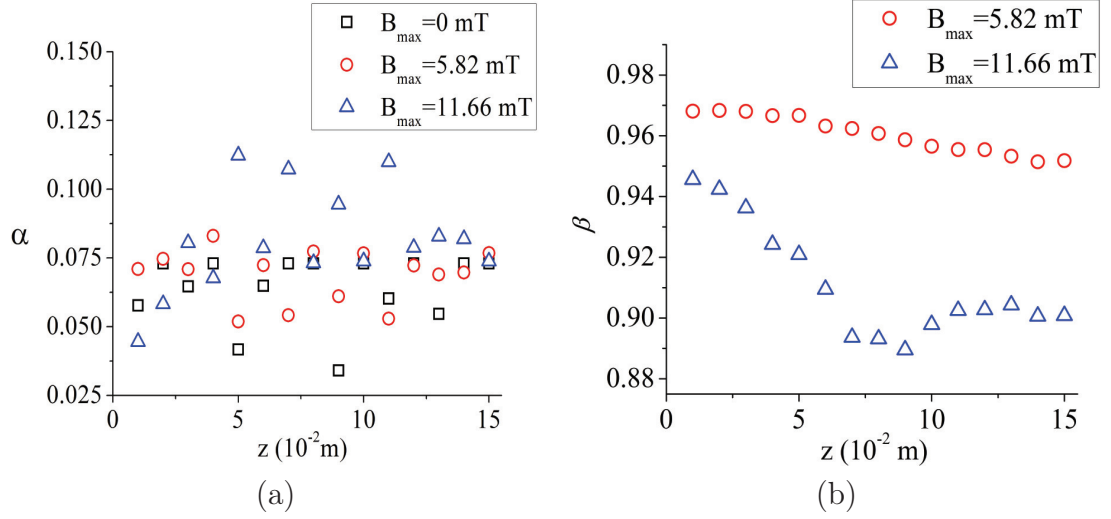


Figure 3.12: (a): Correction factor corresponding to the difference in the measured and actual plasma potential along the axis of hollow cathode cavity. (b): Magnetic correction factor along the axis of hollow cathode cavity.

3.4.2 Correction factors for determining electron saturation current

The two important limitations discussed above suggest that the electron saturation current can be underestimated due to the presence of a magnetic field as well due to the reference electrode not being in good contact with the plasma.

It is seen in the experimental $I(U)$ traces that the plasma potential is obtained at a lower value U_p and correspondingly the measured electron saturation current is underestimated. Therefore the correction factor corresponding to this effect can be found by considering the difference in the probe current; which is proportional to the difference of the actual and measured plasma potential defined by the exponential term $\alpha = \exp\left(\frac{U_p - V_p}{T_e}\right)$. The second correction term corresponds to the magnetization effects, which is given by the parameter; $\beta = \left\{1 + \frac{\pi r_p}{8 \lambda_e} \sqrt{1 + \frac{\lambda_e^2}{\rho_l^2}}\right\}^{-1}$. Figure 3.12 shows these correction factors which are obtained for all the axial probe measurements along the magnetic field.

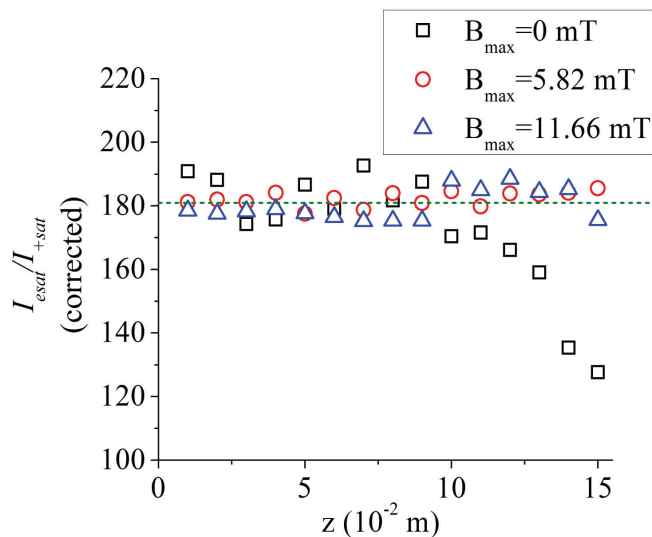


Figure 3.13: Corrected electron to ion saturation current ratios along the axis of hollow cathode cavity.

Using equation 3.14, the actual electron saturation current can be estimated as;

$$I_{esat} = \frac{I_{esat}|_{measured}}{\alpha\beta} \quad (3.15)$$

As the figure 3.13 demonstrates, the above corrections when applied to the experimental data brings the ratio of electron to ion saturation current close to ~ 178 as expected for the case of Argon plasma. Therefore, in an iterative manner, the actual values of electron saturation current is used to obtain total electron population, which finally gives the individual contributions resulting from bulk and hot electrons present in the discharge [54].

Summary and conclusion

In summary, this chapter highlights the combined effect of the magnetic field and probe reference on the current-voltage characteristics of a cylindrical Langmuir probe. By comparing the measured and theoretically modeled $I(U)$ traces, an iterative analysis approach has been recommended to estimate the reliable plasma parameters. Therefore, using this methodology actual value of electron saturation current is initially estimated and thereafter it is used to evaluate the bulk and hot

electron densities. The above probe analysis technique has been implemented in the present study to characterize the cylindrical and conical hollow cathode plasma sources operated in a floating configuration in the presence of an axial magnetic field.

4

Global Discharge Model for Cylindrical and Conical Hollow Cathode

The global discharge model is a widely popular technique for determining plasma parameters in discharge with the consideration that the plasma acts as a fluid [1, 21, 22]. The model is particularly useful for estimating the spatial distribution of plasma density and temperature inside a given discharge volume [23, 70–74]. In this chapter the global model is formulated for a DC discharge consisting of conical and cylindrical hollow cathode geometry. For benchmarking the global discharge model, the analytical results are compared with the experimental data for the unmagnetized case. Finally, the model is applied for predicting the effect of the apex angle of the conical hollow cathode on the density and the temperature variation inside the cathode cavity [23].

The chapter is organized as follows: A brief introduction to the global discharge model is presented in section-4.1. The formulation of the analytical model for cylindrical and conical hollow cathode geometry is presented in section-4.2. In section-4.3, the experimental results are discussed and they are qualitatively compared with the modeling results. Finally, the overall scope of the global model approach is presented in section-4.4.

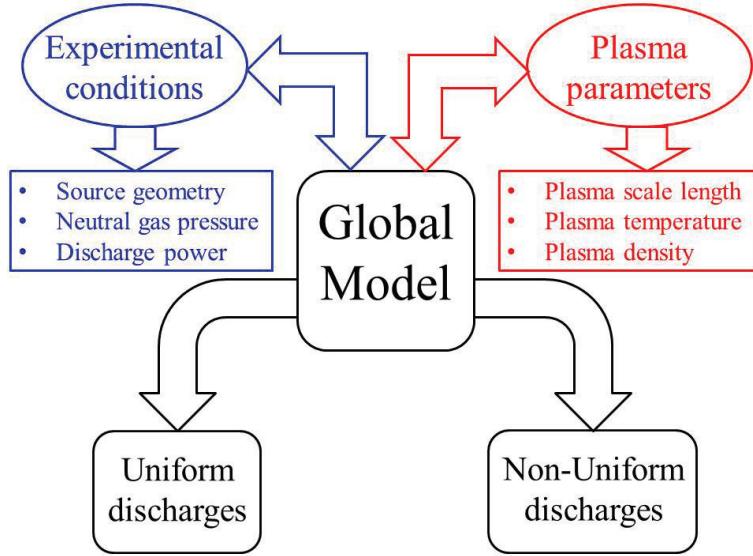


Figure 4.1: Overview of the global discharge model.

4.1 Global discharge model

The term global model is generally applied for a system that considers the externally applied parameters such as *discharge power*, *electrode geometry* and *operating gas pressure* as the input and provides the volume-averaged parameters such as *density* and *temperature* of the charge species inside the plasma as the output. The technique is computationally cheaper as compared with particle-in-cell (i.e. PIC) simulation, and very much helpful in getting direct information about the behavior of the discharge [22, 75, 76]. Therefore the global model has been widely applied for electronegative as well as electropositive discharges [23, 70, 71, 73, 75–78].

As shown in figure 4.1, the global model can be categorized into two types: *homogeneous / uniform* and *in-homogeneous / non-uniform* discharge model [1, 22]. In a uniform discharge model, since plasma density and temperature are uniform over the plasma dimension, it is easy to formulate particle and energy balance relations to estimate the plasma parameters [1]. However in the case of in-homogeneous discharge, the plasma density profile needs to be estimated with the help of fluid equations [22, 23]. The density profile can then be used to formulate particle and energy balance equations for determining the peak plasma density n_0 , plasma scale

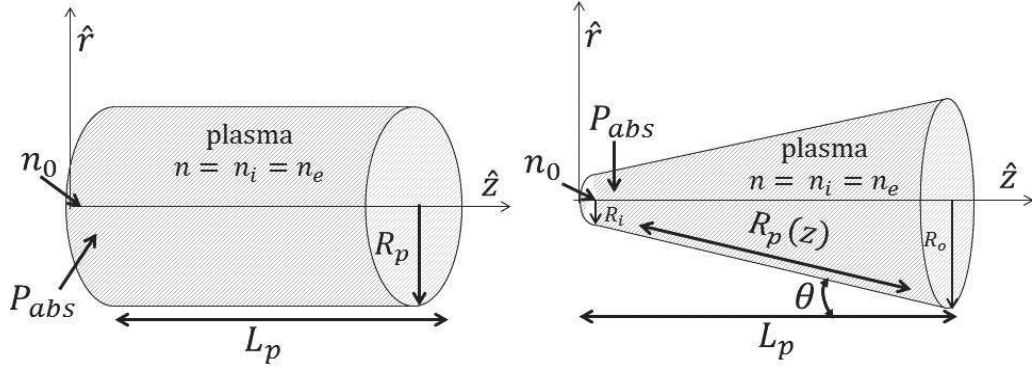


Figure 4.2: Cylindrical and conical plasma volume with peak plasma density n_0 , plasma radius R_p and plasma length L_p inside respective HC cavities.

length Λ and the average plasma temperature T_e according to the given experimental condition. In global discharge modeling, the particle and energy balance equations are formulated to study the discharge properties for given experimental conditions for both uniform and non-uniform discharges as indicated in figure 4.1.

4.2 Global model formulation

Consider the un-magnetized case ($B = 0$) for both cylindrical and conical hollow cathode devices described in figure 2.4 and 2.5. For determining the plasma density and the temperature variation inside these hollow cathode regions; a simple model of the system is shown in the schematic figure 4.2. Here the peak density (i.e. n_0) is considered at the origin, which corresponds to the position of the anode in the actual discharge setup.

Experimentally it is found that the plasma density profile has an axial variation along the z -axis. Therefore the density variation and the average temperature inside the discharge can be found by applying particle and energy balance relations for the case of inhomogeneous discharge.

4.2.1 Spatial plasma density

The spatial density inside the cathode cavity can be obtained by solving the ion continuity equation which assumes plasma quasi neutrality (i.e. $n = n_e = n_i$).

$$\nabla \cdot \Gamma_i = S \quad (4.1)$$

In the above equation, $S = n\nu_{iz}$ is the ionization source term which gives the rate of electron-ion pair created per unit volume [1]. The ionizing collision frequency is depended on electron temperature which is given by $\nu_{iz} = n_g K_{iz} = n_g K_{iz0} \exp(-\varepsilon_{iz}/T_e)$. K_{iz0} is ionization rate constant (for argon, $K_{iz0} = 5 \times 10^{-14}$ m³/s), ε_{iz} is ionization potential (for argon, $\varepsilon_{iz} = 15.75$ V), n_g is neutral gas density and T_e is electron temperature in volts.

It is important to note that the transport of ions in the plasma volume usually depends on the operating pressure regime [1, 22]. For extremely low neutral gas pressure (i.e. $\lambda_i \gg (R_p, L_p)$), the collisionless transport of ions take place inside the plasma volume depending on the variation in plasma potential (i.e. $\Gamma_i = n_i \sqrt{\frac{2e\Delta\phi_p}{m_i}}$). For intermediate pressure regime (i.e. $\lambda_i \leq (R_p, L_p)$), ion transport takes place with variable mobility (i.e. $\Gamma_i = n_i \sqrt{-U_B^2 \frac{2\lambda_i}{\pi} \frac{\nabla n}{n}}$).

However, as per the present experimental scenario, we have $\lambda_i \ll (R_p, L_p)$; hence, ambipolar flow of positive ions through the open ends of the respective HC's is expressed by diffusion equation as;

$$\Gamma_i = -D_a \nabla n_i \quad (4.2)$$

Where, $D_a = U_B^2/n_g K_{mi}$ is the ambipolar diffusion coefficient which depends on the Bohm velocity U_B and ion-neutral momentum transfer rate constant K_{mi} (for argon, $K_{mi} = 3.9 \times 10^{-15}$ m³/s) [1].

Combining equations 4.1 and 4.2 and assuming azimuthal symmetry; the conti-

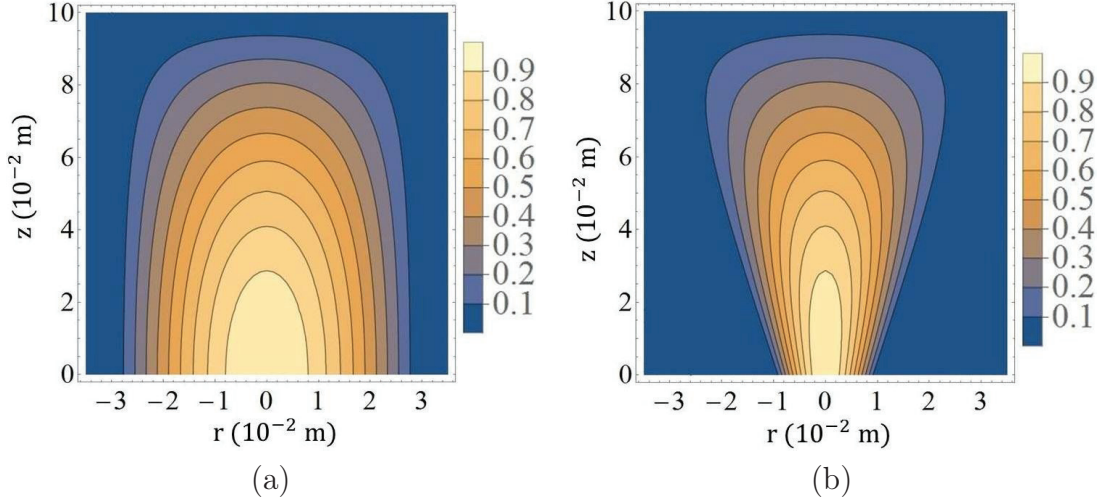


Figure 4.3: (a): Contour plot showing normalized spatial density profile inside cylindrical HC. (b): The contour plot showing normalized spatial density profile inside conical HC.

nuity equation in cylindrical coordinate reduces to;

$$\frac{\partial^2 n}{\partial r^2} + \frac{1}{r} \frac{\partial n}{\partial r} + \frac{\partial^2 n}{\partial z^2} + \left(\frac{\nu_{iz}}{D_a} \right) n = 0 \quad (4.3)$$

The solution of above equation gives the spatial density profile inside the cylindrical volume which is shown in figure 4.3a. To obtain an analytical solution of equation 4.3, the boundary conditions $n(0, 0) = n_0$ and $n(R_p, L_p) \approx 0$ has been considered; where $r = R_p$ is the radius and $z = L_p$ is the axial length of plasma column. The lowest order symmetric solution gives Bessel variation in r and Cosine variation in z [1, 22, 23];

$$n = n_0 J_0(\alpha' r) \cos(\beta' z) \quad (4.4)$$

In equation 4.4 the parameters $\alpha' = \frac{\chi_{01}}{R_p}$, $\beta' = \frac{\pi}{2L_p}$ and $\chi_{01} \approx 2.405$.

For the conical case, the axial dependence of the plasma radius is given by $R_p(z) \approx R_i + z \left(\frac{R_o - R_i}{L_p} \right)$. On considering this relation in equation 4.4, following expression is obtained [23];

$$n = n_0 J_0 \left(\frac{\chi_{01}}{R_p(z)} r \right) \cos(\beta' z) \quad (4.5)$$

With help of above equations 4.4 and 4.5, the density profile inside each plasma source can be obtained by substituting respective physical dimensions the cylindrical and conical hollow cathodes. Figure 4.3 shows the 2D plot of normalized spatial density profile (i.e. $\frac{n}{n_0}$) for the given plasma geometries.

4.2.2 Effective plasma length and the average electron temperature

The electron temperature T_e is strongly dependent on the plasma dimension Λ (i.e. Λ in-terms of R_p and L_p) which are obtained from particle conservation [1, 22, 23].

In figure 4.2 it is observed that the plasma occupies the cylindrical HC volume for $\theta = 0^\circ$; whereas it occupies a conical HC volume for $\theta \approx 14^\circ$. Therefore, a general particle and energy balance relation is formulated considering the apex angle θ . The net plasma particles generated inside the discharge volume is balanced by the particles lost at the lateral plasma boundary and open aperture at $z = L_p$. Therefore, the flux conservation equation for the conical case can be written as [23];

$$\int_0^{2\pi} \int_0^{L_p} R_p(z) \Gamma_i(R_p(z), z) d\phi dz + \int_0^{2\pi} \int_0^{R_p(z)} \Gamma_i(r, L_p) r dr d\phi = \int_0^{L_p} \int_0^{2\pi} \int_0^{R_p(z)} n_i \nu_{iz} r dr d\phi dz \quad (4.6)$$

Using equations 4.2 and 4.5, the net flux at the respective plasma boundaries can be expressed as;

$$\Gamma_i(R_p(z), z) = -D_a \frac{\partial n_i}{\partial r} \Big|_{r=R_p(z)} = \frac{\chi_{01}}{R_p(z)} D_a n_0 J_1(\chi_{01}) \cos\left(\frac{\pi}{2L_p} z\right)$$

$$\Gamma_i(r, L_p) = -D_a \frac{\partial n_i}{\partial z} \Big|_{z=L_p} = \frac{\pi}{2L_p} D_a n_0 J_0\left(\frac{\chi_{01}}{R_o} r\right)$$

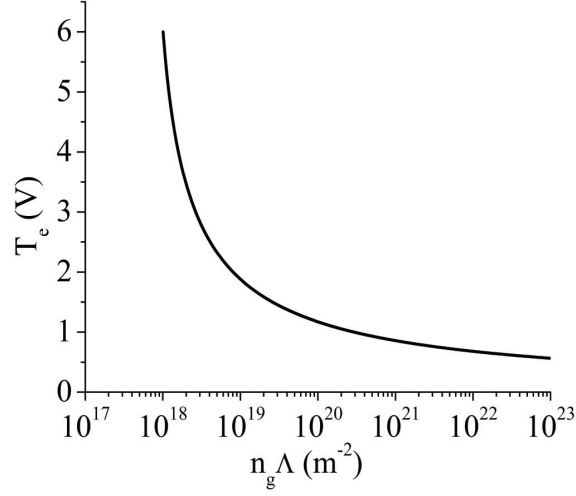


Figure 4.4: Generalized particle balance relation showing the variation of T_e versus product $n_g \Lambda$ for Maxwellian electrons in Argon.

Where, $J_1(\chi_{01})$ is the value of 1st order Bessel function at $\chi_{01} = 2.405$. On substituting these values, equation 4.6 reduces to;

$$4L_p \chi_{01} D_a n_0 J_1(\chi_{01}) + \frac{\pi^2 R_0^2}{L_p \chi_{01}} D_a n_0 J_1(\chi_{01}) = 4K_{iz} n_g \frac{L_p R_i^2}{\chi_{01}} n_0 J_1(\chi_{01}) \sec^2(\theta) \Psi \quad (4.7)$$

In above equation, Ψ is a dimensionless quantity related with R_i , θ and L_p as;

$$\Psi = \left\{ \frac{1}{2} + \frac{L_p^2}{2R_i^2} - \frac{4L_p^2}{\pi^2 R_i^2} \right\} + \left\{ \frac{1}{2} - \frac{L_p^2}{2R_i^2} + \frac{4L_p^2}{\pi^2 R_i^2} \right\} \cos(2\theta) + \left\{ \frac{L_p}{R_i} - \frac{2L_p}{\pi R_i} \right\} \sin(2\theta)$$

Therefore equation 4.7 can be reduced to a generalized particle balance relation, which gives the plasma electron temperature T_e as a product of neutral gas density n_g and effective plasma size Λ_θ , for the conical discharge.

$$n_g^2 \Lambda_\theta^2 = \frac{U_B^2}{K_{iz0} K_{mi}} \exp\left(\frac{\varepsilon_{iz}}{T_e}\right) \quad (4.8)$$

In equation 4.8, the plasma scale length Λ_θ defines the effective plasma size in terms of parameters; R_i , R_o , L_p and apex angle θ .

$$\Lambda_\theta^2 = \frac{4L_p^2 R_i^2 \sec^2(\theta) \Psi}{\pi^2 R_0^2 + 4\chi_{01}^2 L_p^2} \quad (4.9)$$

It can be seen that in the limiting case, the equation 4.9 reduces to a cylindrical geometry as $\theta \rightarrow 0 \Leftrightarrow \Psi \rightarrow 1$ or $R_i \rightarrow R_o \approx R_p$;

$$\lim_{\theta \rightarrow 0} \Lambda_\theta = \left(\frac{4L_p^2 R_p^2}{\pi^2 R_p^2 + 4\chi_{01}^2 L_p^2} \right)^{1/2} = \Lambda_0$$

Thus the effective plasma size Λ can be calculated using 4.9 by substituting L_p and R_p values of respective hollow cathode source. Finally the formulated particle balance relation (i.e. see figure 4.4) can be used to determine the average temperature inside respective HC by providing corresponding neutral gas pressure.

4.2.3 Peak plasma density

The effective plasma size (i.e. Λ) and average electron temperature T_e are the two parameters that are used to solve the energy conservation equations for determining the peak plasma density n_0 [1, 22, 23].

The power coupled to the charge particles in a discharge is lost via particle fluxes escaping the plasma boundaries and inter-particle collisions. Therefore, the particle balance relation can be written as [23];

$$\begin{aligned} P_{lost} = e(\varepsilon_i + \varepsilon_e) \int_0^{2\pi} \int_0^{L_p} R_p(z) \Gamma_i(R_p(z), z) d\phi dz \\ + e(\varepsilon_i + \varepsilon_e) \int_0^{2\pi} \int_0^{R_p(z)} \Gamma_i(r, L_p) r dr d\phi \\ + e\varepsilon_c \int_0^{L_p} \int_0^{2\pi} \int_0^{R_p(z)} n_i \nu_{iz} r dr d\phi dz \quad (4.10) \end{aligned}$$

In the above equation, $\varepsilon_i = V_s + T_e/2$ is ion kinetic energy lost at the surface, V_s is the voltage drop across the cathode sheath [1]. Since in a D.C discharge, a significant amount of the applied voltage is dropped across the cathode sheath we can approximate; $V_s \approx V_{dis}$. Also $\varepsilon_e = 2T_e$ is electron kinetic energy lost at the surface and ε_c is collisional energy lost per electron-ion pair lost from the system

which is given by [1];

$$\varepsilon_c = \varepsilon_{iz} + \varepsilon_{ex} \frac{K_{exo}}{K_{iz0}} T_e^{\frac{1}{3}} \exp\left(\frac{\varepsilon_{iz} - \varepsilon_{ex}}{T_e}\right) + \frac{3mT_e}{M} \frac{K_{el}}{K_{iz0}} \exp\left(\frac{\varepsilon_{iz}}{T_e}\right) \quad (4.11)$$

Where, K_{exo} is excitation rate constant (for argon, $K_{exo} = 2.48 \times 10^{-14}$ m³/s), K_{el} is the rate of elastic scattering (for argon it is constant, $K_{el} = 10^{-13}$ m³/s), ε_{ex} is the average excitation energy (for argon, $\varepsilon_{ex} = 12.24$ V). Considering total energy lost from the system per electron-ion pair lost i.e $\varepsilon_T = \varepsilon_i + \varepsilon_e + \varepsilon_c$, equation 4.10 reduces to [1, 23];

$$P_{lost} = \frac{en_0\varepsilon_T U_B^2 J_1(\chi_{01})}{L_p \chi_{01} n_g K_{mi}} (\pi^2 R_o^2 + 4\chi_{01}^2 L_p^2) \quad (4.12)$$

On equating the total power absorbed in the conical system to the total power lost at the surface, we get,

$$P_{dis} = \frac{en_0\varepsilon_T U_B^2 J_1(\chi_{01})}{L_p \chi_{01} n_g K_{mi}} (\pi^2 R_o^2 + 4\chi_{01}^2 L_p^2) = P_{lost} \quad (4.13)$$

Thus using the above relation, the peak density n_0 can be estimated in terms of power absorbed inside the plasma volume (i.e $P_{dis} = V_{dis} I_{dis}$), which can be expressed as;

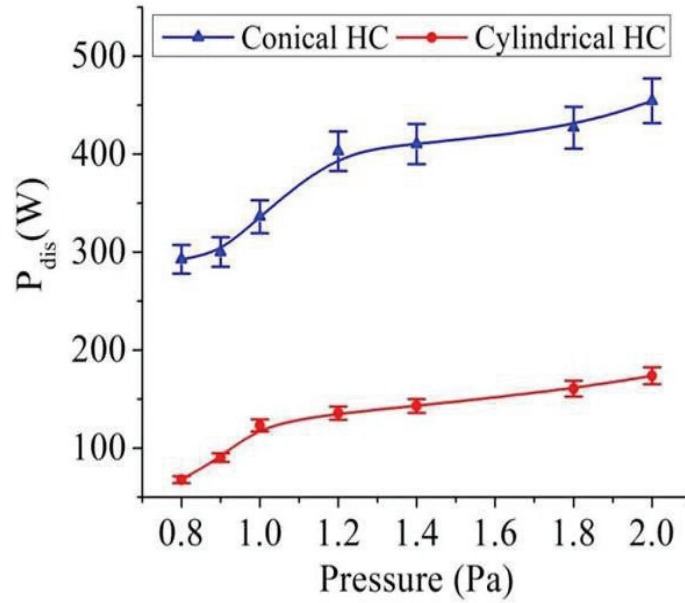
$$n_0 = \frac{n_g P_{dis} \chi_{01} L_p K_{mi}}{e \varepsilon_T U_B^2 J_1(\chi_{01})} \left(\frac{1}{\pi^2 R_o^2 + 4\chi_{01}^2 L_p^2} \right) \quad (4.14)$$

The power balance equation 4.14 indicates that the peak plasma density n_0 is directly proportional to the product $n_g P_{dis}$ and thus for a given discharge condition n_0 is indirectly related to T_e .

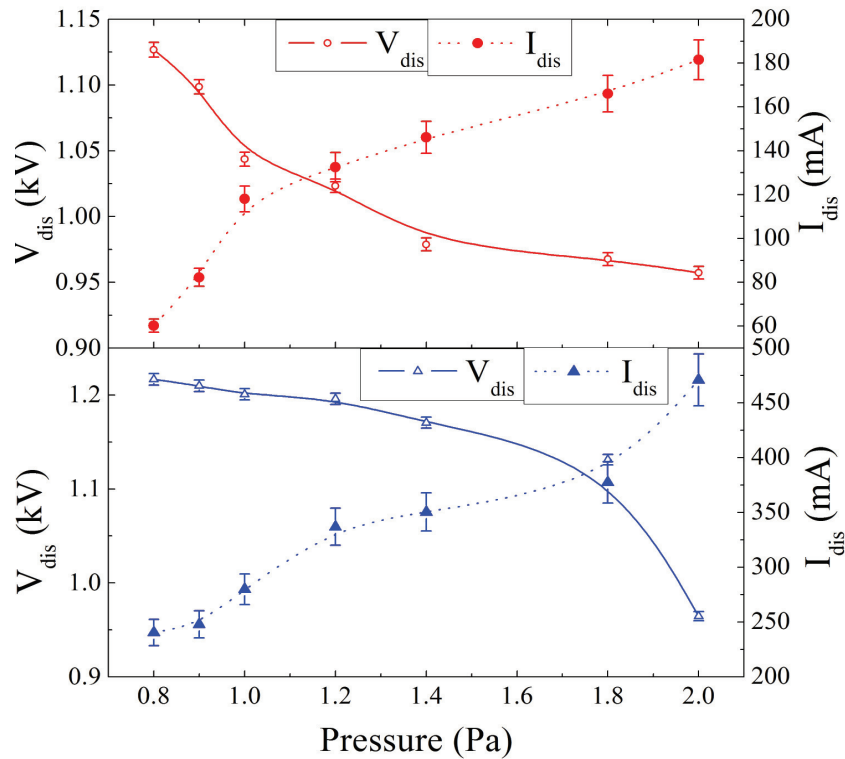
4.3 Experimental and Modeling results

In figure 4.5a, the plot of discharge power verses operating gas pressure obtained for argon discharge is shown respectively for the case of cylindrical and conical hollow cathodes.

As seen in figure 4.5a, the net power dissipated in the discharge increases with an increase in gas pressure, but the rate of rise decreases at higher operating pres-



(a)



(b)

Figure 4.5: (a): Effect of neutral gas pressure on discharge power. (b): Effect of neutral gas pressure on discharge voltage and discharge current across the discharge electrodes. Triangle represents the experimental data for the case of conical HC whereas circles represent the data for cylindrical case.

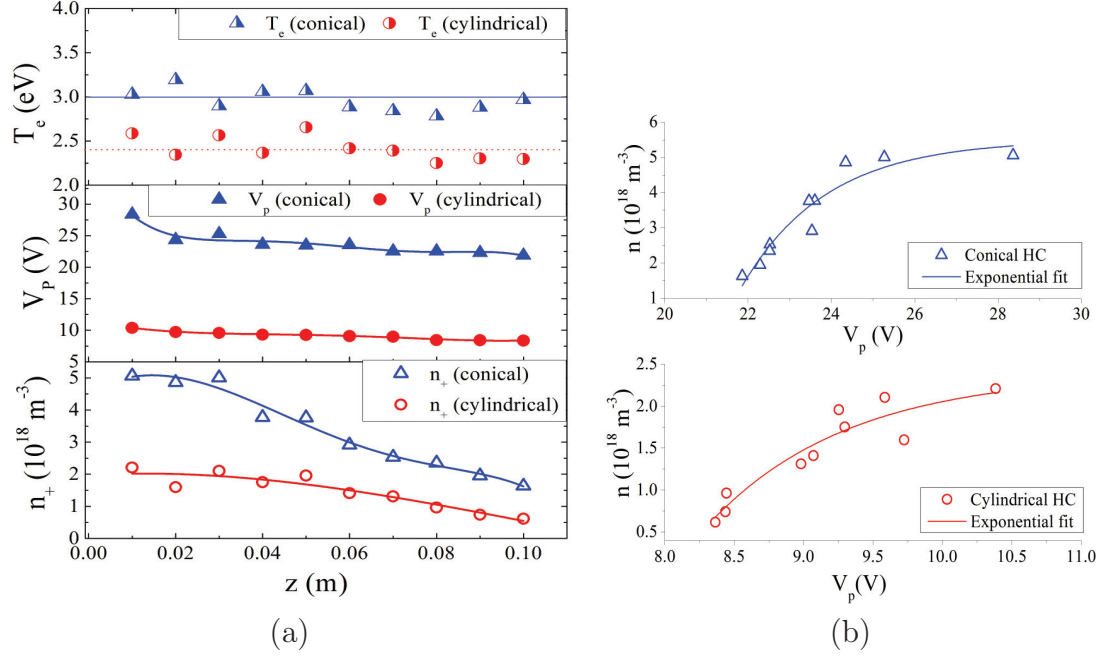


Figure 4.6: (a): Axial plasma parameters inside respective HC cavities. (b): Plasma density and potential indicating the Boltzmann distribution inside the source cavities.

tures. It is also seen that the power dissipated in the discharge is higher for the case of conical hollow cathode. With an increase in neutral gas pressure, the power dissipation increases owing to the high resistive heating caused by an increase in ionizing collisions [44, 45]. In figure 4.5b, the discharge current increases steadily with a rise in the background pressure; correspondingly the voltage across the discharge electrode decreases. The rate of voltage fall is slower in the case of conical HC than the cylindrical cathode [23].

The axial plasma parameters for the respective hollow cathodes are shown in Figure 4.6a. The electron temperature remain uniform however, the average T_e is higher in the case of conical HC for a similar operating pressure. The plasma density and axial plasma potential increases towards the anode at $z = 0$. The contour plots in figure 4.3 obtained using the global model also indicates that the plasma density is high near the anode (i.e $z = 0$) and it falls radially as well as axially from the anode surface.

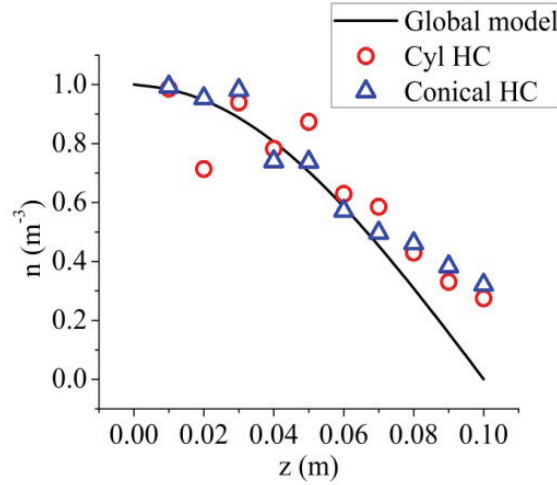


Figure 4.7: Axial profile of normalized plasma density inside HC cavity. The scattered data points represents the experimental values of plasma density which have been normalized with the peak measured density at $z = 0.01$ m.

In figure 4.6b, the plasma density is plotted against the plasma potential which shows an exponential behavior following the Boltzmann distribution. Figure 4.7 shows the axial plot of plasma density along with the results obtained using the global model.

As shown in figure 4.7, the plasma density variation is almost similar along the z -axis for both the plasma sources. This result is in qualitative agreement with the modeling results shown in figure 4.3. It can be seen that the axial profiles are found to be in good qualitative agreement with the model. However, a slight deviation is seen towards the open end of the HC owing due to the imposition of boundary condition $n(L_p) = 0$ for obtaining an analytical solution. In reality, the plasma density is not zero at the boundary, instead, it starts to fall rapidly at this location.

The electron temperature obtained using particle balance relation for both cylindrical/conical setups for a range of operating pressure is shown along with the experimental data points in figure 4.8a. The results show an excellent agreement. It is found that T_e falls monotonically as the pressure increases for both conical and cylindrical HC. The cumulative elastic scattering of the electrons with the background neutrals is primarily responsible for observing the fall in average elec-

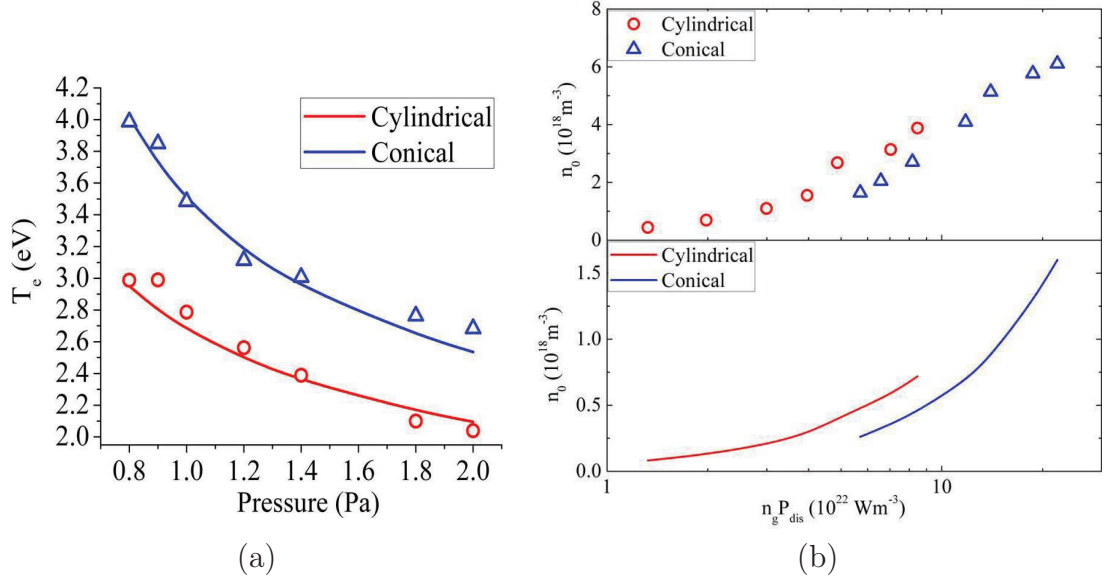


Figure 4.8: (a): Average T_e inside HC cavity for experimental values of neutral gas pressure. (b): Peak plasma density n_0 inside HC for experimental values of the product $n_g P_{dis}$. The scattered data points represent the experimental values.

tron temperature inside the discharge volume.

On the other hand in figure 4.8b, the plasma density obtained using power balance equation 4.14 shows an increasing trend with product $n_g P_{dis}$; as the ionization frequency increases with neutral gas density. Thus it can be seen from figure 4.8 that plasma parameters obtained from the experimental measurements are in qualitative agreement with the results obtained from the global model.

The peak plasma densities obtained from the model are found to be lower by a factor of ≈ 6 than in the experiments (i.e. see figure 4.8b), possibly due to 30-40% inherent error associated in probe measurements. However, the values of T_e obtained from the model show a very good match with the experiment as in figure 4.8a. Also as shown in figure 4.7, the experimental trends in the axial density variation are found to be in good qualitative agreement with the analytical model.

4.4 Overall scope of the global discharge model

Although the global models based on the particle and power balance are extensively used to understand low-temperature discharges, it is necessary to emphasize few inherent limitations with this approach [22]. One of the limitations is the underestimated values of plasma density which is obtained from power balance relation as observed in figure 4.8b. However, it has been mentioned in a few references that the power balance relation is only useful to get a qualitative estimate of the density for a given range of experimental conditions [1, 22, 23].

In the present case, the formulated model is used to investigate the effect of cathode geometry on the plasma density and temperature variation in a discharge occupying the hollow cathode cavity. As shown in section-4.3, the generalized global model is benchmarked against a range of experimental data for both cylindrical and conical hollow cathode sources. Therefore, such a model can be used to anticipate the performance of a hollow cathode source with varying cathode aperture / apex angle [23]. This variation has been shown in figure 4.9, where peak plasma density and T_e is plotted as a function of the apex angle θ for the given operating conditions of discharge power and pressure. It is found that peak plasma density decreases whereas T_e increases as the apex angle θ is increased from $\theta = 0^\circ$ to $\theta = 14^\circ$. The fall in the plasma density is attributed due to a reduction in the number of ionizing electrons inside the cathode, as the effective plasma size gets reduced owing to the angular geometry.

In the past, these models have also been developed and applied for a wide variety of plasmas including multicomponent species with complex chemistries [73, 74, 77] as well as low-pressure electropositive and electronegative discharges [23, 70, 71, 73, 75–78]. Even for the complicated discharge geometries, the global model approach is preferred over the PIC simulations as it quickly estimates the spatially averaged plasma parameters such as densities or temperatures that would otherwise be computationally difficult to design and simulate [75, 76]. Therefore, using the global discharge model an optimal operating condition can be chosen for a particular geometry of discharge electrodes that can be used to obtain the desired plasma parameters [21, 23].

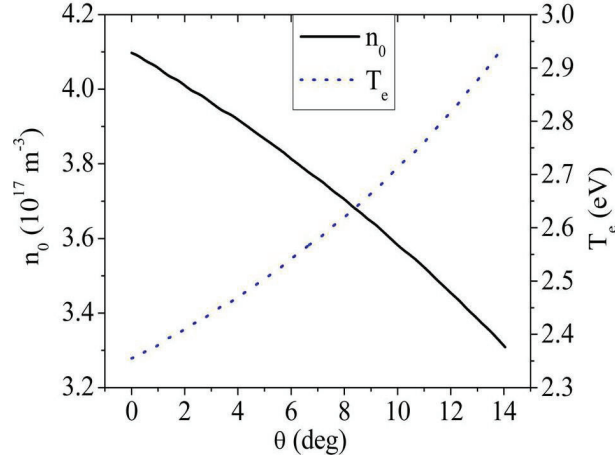


Figure 4.9: Variation in global plasma parameters as a function of apex angle θ or HC geometry under fixed discharge condition (i.e discharge power = 145 W and pressure = 1.4 Pa).

Summary and conclusion

In summary, this chapter highlights a general methodology to formulate a global discharge model employing the particle and energy conservation relations for the case of non-uniform discharge in the absence of an external magnetic field. The prime motivation of this global model study is to investigate the effect of neutral gas pressure and discharge power on the global density and temperature variation inside the conical and cylindrical plasma devices. The modeling results are in a qualitative agreement with the experimental probe measurements inside hollow cathode cavities of both the above plasma sources. This chapter also highlights the silent feature of the global model approach as a source / experiment design tool; as it helps to select the source dimensions / geometry and set the range of experimental operating conditions to achieve a discharge with the desired plasma parameters.

5

Magnetic Field Effects on Direct-Current Hollow Cathode Discharge

DC discharge, operated with a cold cathode is primarily sustained via secondary electrons emitted by positive ion bombardment at the cathode surface [1, 4, 49]. Applying an external magnetic field in the system can improve the discharge efficiency by reducing the radial loss of electrons [4, 50]; however the electron emission can be significantly hindered in a hollow cathode discharge [18, 48, 49, 51]. This chapter is primarily devoted to understand the role of the external magnetic field on secondary electron emission yield and its impact on the performance of cylindrical and conical hollow cathode discharge [18].

Section-5.1 gives a brief introduction to the breakdown and sustenance of a DC discharge. In section-5.2, the impact of the external magnetic field on secondary electron emission is addressed by formulating a phenomenological model. The experimental results are qualitatively discussed in section-5.3 along with results obtained from the analytical model. The overall results are hence summarized at the end of the chapter.

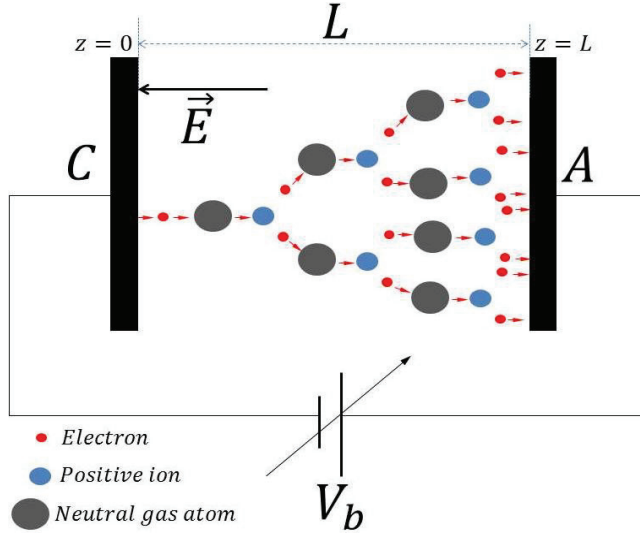


Figure 5.1: Townsend avalanche process in the breakdown of a neutral gas.

5.1 DC discharge breakdown and sustenance

As shown in schematic figure 5.1, the DC breakdown refers to an avalanche situation when electron multiplication between the discharge gap grows exponentially from an initial flux of electron emitted from the cathode surface [24]. This is described by the following equation [1, 4];

$$\frac{d\Gamma_e}{dz} = \alpha_i \Gamma_e \quad (5.1)$$

Where, Γ_e is the electron flux and proportionality constant α_i is the inverse of the mean free path for ionization which is also known as Townsend's first ionization coefficient. The first Townsend coefficient or ionization coefficient is a complicated function of the accelerating electric field between the discharge electrodes and neutral gas pressure. The electron flux along the direction of the electric field is then given as;

$$\Gamma_e(z) = \Gamma_e(0) \exp \left[\int_0^z \alpha_i(z') dz' \right] \quad (5.2)$$

Considering the continuity of the total charge particles (i.e creation of equal numbers of electron-ion pairs) we can write [4];

$$\Gamma_i(0) - \Gamma_i(L) = \Gamma_e(0) \left\{ \exp \left[\int_0^L \alpha_i(z') dz' \right] - 1 \right\} \quad (5.3)$$

Since the discharge is self-sustained we must have $\Gamma_e(0) = \gamma_{se}\Gamma_i(0)$ and $\Gamma_i(L) = 0$. Using this, the condition of discharge self-sustainability is obtained as;

$$\exp \left[\int_0^L \alpha_i(z') dz' \right] = 1 + \frac{1}{\gamma_{se}} \quad (5.4)$$

As shown in figure 5.1, for the vacuum breakdown, the electric field E in the discharge gap is constant and hence, the electron energy is a constant. These considerations allow us to treat α_i as constant in the above equation. This gives a breakdown condition for a DC discharge as;

$$\alpha_i L = \ln \left[1 + \frac{1}{\gamma_{se}} \right] \quad (5.5)$$

The ionization coefficient α_i is usually expressed in the form [1, 4];

$$\frac{\alpha_i}{p} = A \exp \left[-\frac{Bp}{E} \right] \quad (5.6)$$

In the above equation, the parameters A and B are determined experimentally and they are found to be roughly constant for a given neutral gas over a range of operating pressures (i.e. p) and electric fields [1, 4, 49]. If the breakdown potential required to trigger the discharge is $V_b = EL$ then using above equations we obtain a relationship between V_b , p and L as;

$$ApL \exp \left[-\frac{BpL}{V_b} \right] = \ln \left[1 + \frac{1}{\gamma_{se}} \right] \quad (5.7)$$

The above non-linear equation can be solved in terms V_b ;

$$V_b = \frac{BpL}{\ln [ApL] - \ln \left[\ln \left[1 + \frac{1}{\gamma_{se}} \right] \right]} \quad (5.8)$$

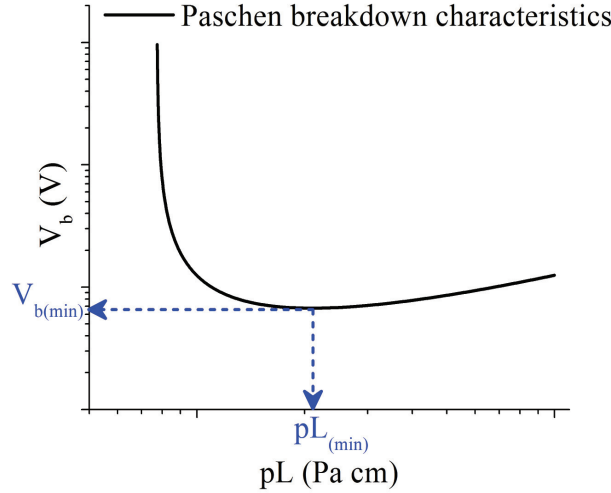


Figure 5.2: Typical Paschen characteristic curve showing the relationship between breakdown voltage V_b , operating pressure p and electrode separation L .

The characteristics curve which relates the breakdown voltage (i.e. V_b), neutral gas pressure (i.e. p) and the electrode gap length (i.e. L) is called Paschen curve. This curve shows that for a given separation L between the discharge electrodes there is an optimal range of neutral gas pressure p for plasma breakdown. This characteristics curve is different for every neutral gas used for the discharge. As shown in figure 5.2 the Paschen minima (i.e. $pL_{(min)}$) corresponds to the minimum value of breakdown voltage (i.e. $V_{b(min)}$). These values are expressed as;

$$pL_{(min)} = \frac{\exp(1)}{A} \ln \left[1 + \frac{1}{\gamma_{se}} \right] \quad (5.9)$$

$$V_{b(min)} = \exp(1) \frac{B}{A} \ln \left[1 + \frac{1}{\gamma_{se}} \right] \quad (5.10)$$

For a given neutral gas, the Paschen curve helps to estimate the optimal range of discharge voltage and operating pressure which is required to trigger the breakdown in a given discharge setup [1, 4].

5.1.1 Paschen relation for discharge sustenance

As explained in chapter-1 (i.e. section-1.2), low pressure DC discharges are sustained by the emission of secondary electrons from the cathode, under the influence

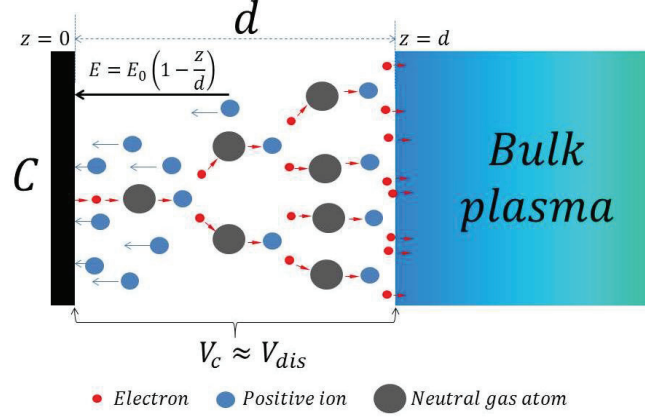


Figure 5.3: Cathode fall region after the discharge is established.

of positive ion bombardment at the cathode surface [1, 4, 24]. As shown in equation 1.4, the secondary electron emission yield γ_{se} depends on the cathode fall voltage drop V_c and the collisional energy loss ε_c (i.e. given in equation 4.11). These energetic electrons interact with the background gas atoms and eventually sustain the DC discharge undergoing ionizing collisions.

As soon as the discharge is established as shown in figure 5.3, almost all the applied voltage between the electrodes drops in the cathode fall region (i.e. $V_c \approx V_{dis}$). Therefore, after the establishment of the discharge equation 5.4 gets modified as [1];

$$\exp \left[\int_0^d \alpha_i(z') dz' \right] = 1 + \frac{1}{\gamma_{se}} \quad (5.11)$$

In the above expression, d is the length of the cathode fall region. The Townsend coefficient $\alpha_i(z')$ is a function of position within the cathode fall region. In a similar approach a Paschen like relationship can be established between cathode fall voltage V_c and cathode sheath thickness d , for a given neutral gas pressure p [1]. Assuming the linear variation of the electric field in the cathode sheath region, V_c can be expressed as;

$$V_c = \frac{1}{2} \left[\frac{Bpd}{\ln [Apd] - \ln \left[\ln \left[1 + \frac{1}{\gamma_{se}} \right] + (Apd) \left(\frac{Bpd}{2V_c} \right) \Gamma \left(0, \frac{Bpd}{2V_c} \right) \right]} \right] \quad (5.12)$$

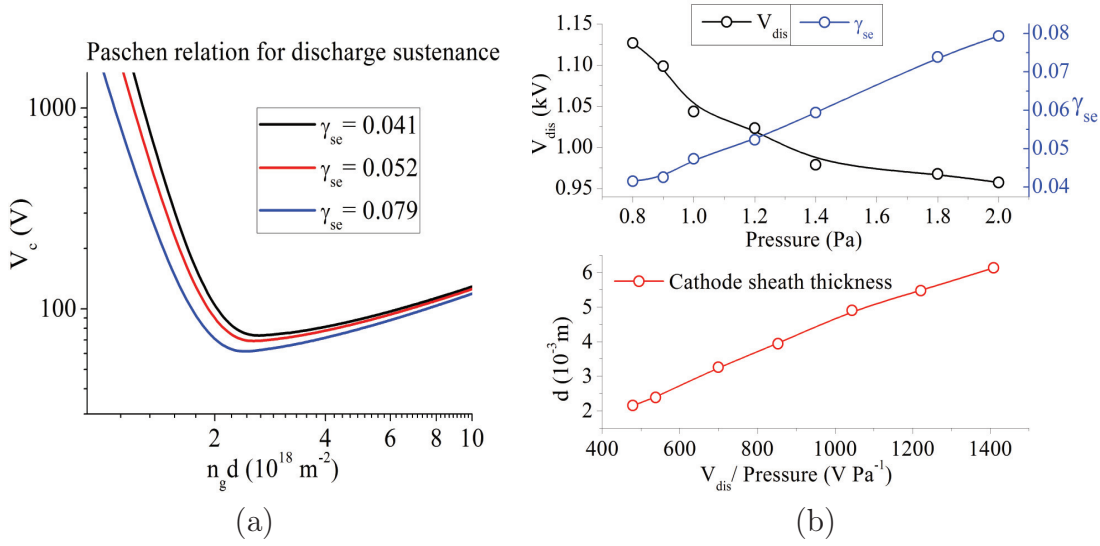


Figure 5.4: (a): Paschen like characteristics for discharge sustenance using Argon gas. (b): Cathode sheath thickness " d " estimated from the characteristic curve for the experimental values of discharge voltage V_{dis} , $\gamma_{se} \approx \varepsilon_c/V_{dis}$ and neutral gas pressure for cylindrical HC source.

In equation 5.12, $\Gamma\left(0, \frac{Bpd}{2V_c}\right)$ is an incomplete Gamma function. This complex equation can be numerically solved for obtaining the discharge sustenance condition, which gives a Paschen like characteristics as shown in figure 5.4a. The above relationship can be used to estimate the cathode fall thickness " d " for a set of experimental values of discharge voltage and neutral gas pressure. As shown in figure 5.4b, it is found that with an increase in neutral gas pressure, secondary electron emission yield $\gamma_{se} = \frac{\varepsilon_c}{V_{dis}}$ increases, hence lower values of cathode sheath thickness and cathode fall voltage drop is observed.

5.2 Magnetic field effects on discharge sustenance

If an external magnetic field is introduced in a DC discharge, the electrons are constrained to follow along the magnetic field lines [17, 41]. If the magnetic field is parallel to the cathode surface, then owing to sheath electric field \vec{E} being transverse to the magnetic field, it gives rise to a $\vec{E} \times \vec{B}$ drifts of electrons released from the cathode surface [18, 47–49, 51]. For a stronger magnetic field, a fraction of secondary electrons can be recaptured at the cathode surface before completing its

orbit [48, 52]. Hence, the recapture is more pronounced in the case if the magnetic field is parallel to cathode surface, as a result the net secondary electron emission yield is effectively reduced to γ_{eff} where; $\gamma_{eff} < \gamma_0$ (here $\gamma_0 = \gamma_{se}|_{B=0}$ is the net secondary electron emission yield in absence of magnetic field) [18, 47, 49]. The recapture of secondary electrons at the cathode surface reduces gradually as the direction of the magnetic field becomes parallel to the sheath electric field, hence the secondary electron emission characteristics strongly depend on the angle between the sheath electric field and the magnetic field at the cathode surface [18].

In the case of a cylindrical hollow cathode, the sheath electric field is perpendicular to the axial magnetic field, whereas in the case of conical HC, the axial magnetic field makes an oblique angle θ with the sheath electric field. The individual effects of the above HC geometries on secondary electron emission and discharge characteristics are presented below.

5.2.1 Secondary electron emission from cylindrical hollow cathode surface

For the case of cylindrical cathodes, two popular geometries are shown in figure 5.5 which consist of a solid cylindrical cathode with an axial magnetic field and a hollow cylindrical cathode pertaining to our present study. The solid cylindrical cathode is popular in magnetron sputtering targets [7].

As shown schematically in figure 5.5, the secondary electrons undergo cycloidal trajectories under the influence of $\vec{E} \times \vec{B}$ drifts. The path is epicycloidal for the case of solid cylindrical cathode [48]; whereas for the hollow cylinder in figure 5.5b hypocycloidal trajectories is seen inside the hollow cylindrical cavity. Depending on the magnetic field strength, the secondary electrons can return back to the cathode surface, eventually resulting in either a recapture or reflection [47, 48, 52].

If ρ_l is the electron larmor radius and hollow cathode radius is R_C , the hypocycloidal path length "a" traveled by a magnetized electron under the influence of

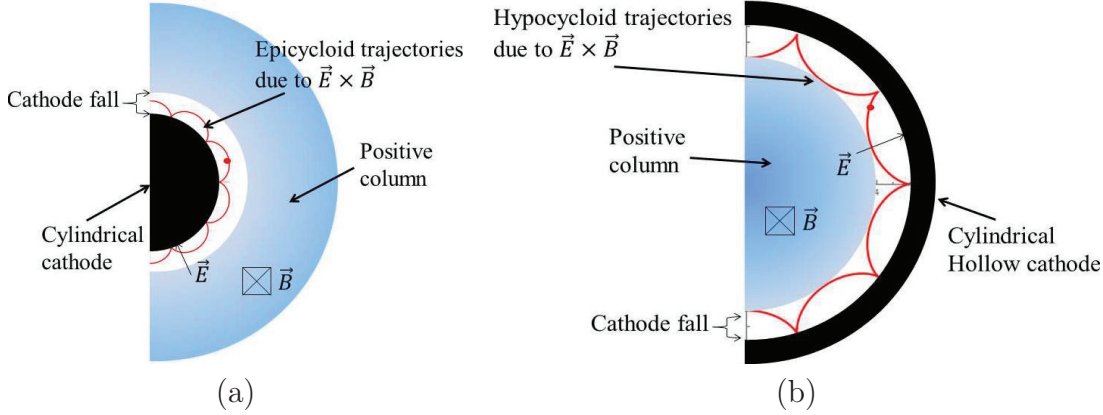


Figure 5.5: (a): Effect of transverse magnetic field on the trajectories of secondary electrons emitted from solid cylindrical cathode. (b): Effect of transverse magnetic field on the trajectories of secondary electrons emitted from hollow cylindrical cathode.

cross-field drifts is given as [48];

$$a = 8\rho_l^2 \left(\frac{1}{\rho_l} - \frac{1}{R_C} \right) \approx \frac{8Em_e}{eB^2} \quad (5.13)$$

In equation 5.13, B is magnetic field strength, m_e is the mass of electron, e is the charge of electron and $E \approx V_c/d$ is the cathode fall electric field. If λ is the mean free path for electron neutral collisions, cathode recapture probabilities R_{cap} is defined as [18, 48];

$$R_{cap} = \exp\left(-\frac{a}{\lambda}\right) \quad (5.14)$$

In above equation $\lambda = \frac{1}{n_g\sigma}$; where n_g is neutral gas density and σ is the total electron collision cross-section. Using equation 5.14, recapture probabilities are calculated as a function of axial magnetic field for a given range of neutral gas pressure. In figure 5.6, it is found that the recapture probability increases monotonically with increase in magnetic field and reach a saturation value.

The effective secondary electron emission yield γ_{\perp} for the case of a cylindrical hollow cathode with magnetic field along its axis (i.e. see figure 5.7) can be given

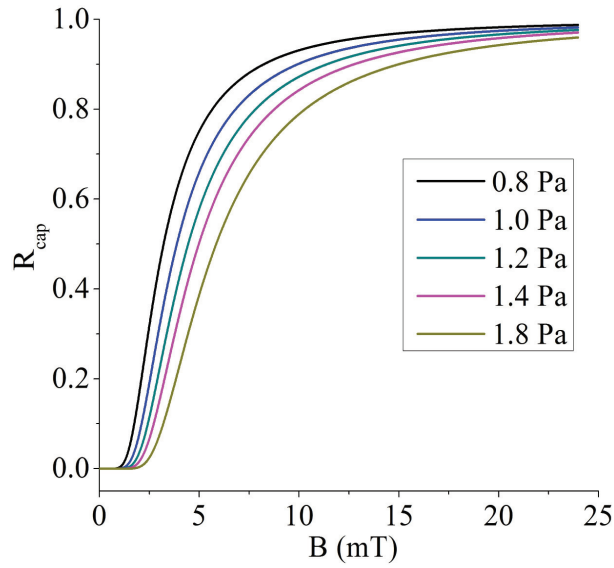


Figure 5.6: Cathode recapture probabilities as a function of axial magnetic field for different neutral gas pressure.

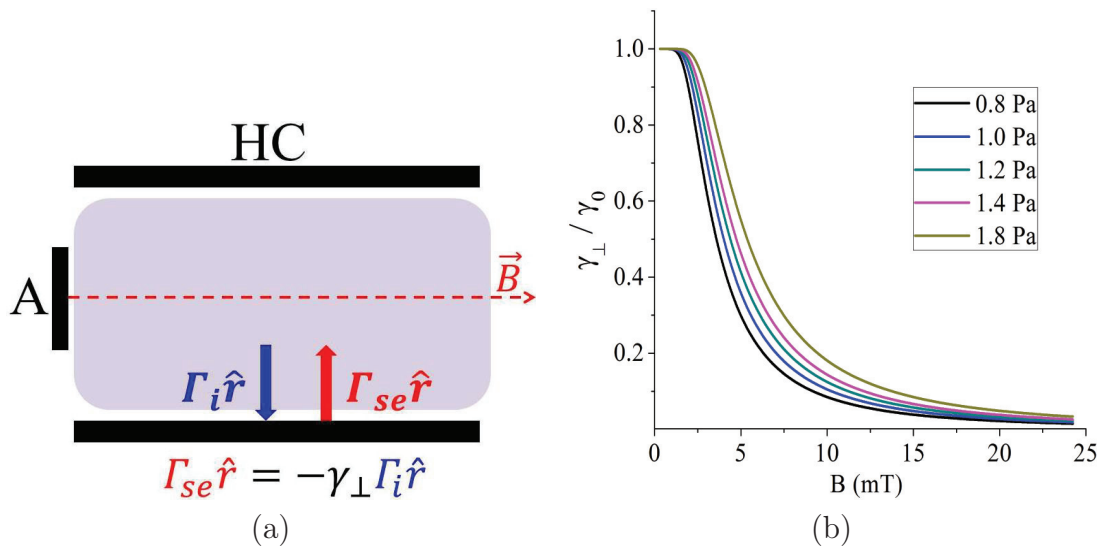


Figure 5.7: (a): Effect of tangential B-field on the flux of secondary electrons from cylindrical HC surface. (b): Effect of tangential B-field on the secondary electron emission yield.

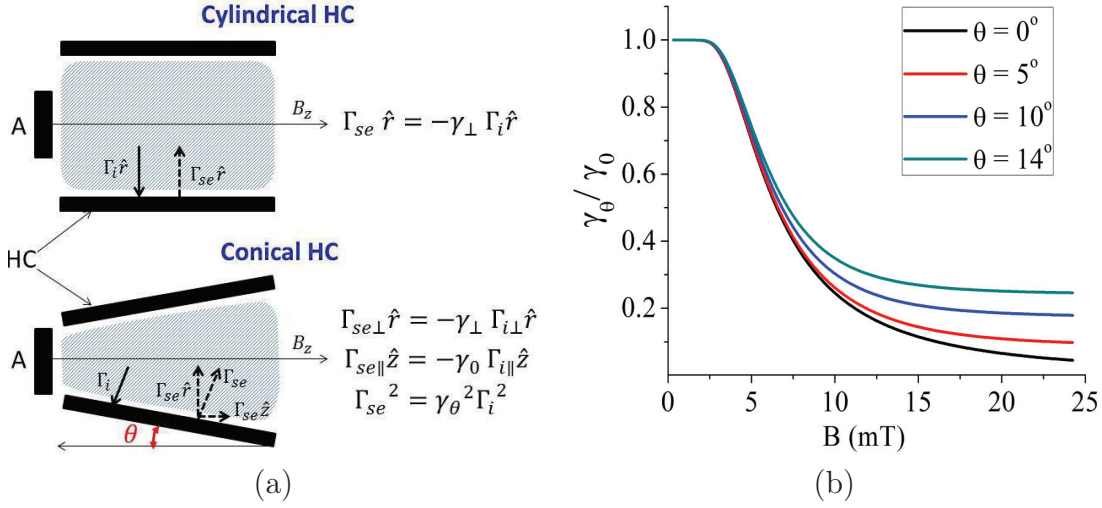


Figure 5.8: (a): Phenomenology to show the effect of oblique B -field on the flux of secondary electrons from HC surface. (b): Effect of oblique angle θ on the secondary electron emission yield.

as [18, 49];

$$\gamma_{\perp} = \gamma_0 \left[\frac{1 + R \left(\frac{\omega_{ce}}{\nu_m} \right)^2}{1 + \left(\frac{\omega_{ce}}{\nu_m} \right)^2} \right] \quad (5.15)$$

In equation 5.15, γ_0 is secondary electron emission yield in absence of magnetic field, ω_{ce} is electron cyclotron frequency, ν_m is total electron neutral collision frequency and reflection coefficient is given as $R \approx 1 - R_{cap}$. As seen in figure 5.7b the secondary electron emission yield fall drastically with increase in the magnetic field corresponding to the given neutral gas pressure.

5.2.2 Secondary electron emission yield from an oblique cathode sheath

For the case of conical cathode, the magnetic field makes a finite angle θ with respect to the cathode surface as shown in figure 5.8a. In this situation, the flux of secondary electrons emerging from the cathode can be resolved in two components, i.e. parallel and perpendicular to the magnetic field. The effective secondary

electron emission yield γ_θ in terms of γ_0 and γ_\perp is given as [18];

$$\gamma_\theta^2 = \frac{2\gamma_0^2\gamma_\perp^2}{\gamma_0^2 + \gamma_\perp^2} - \frac{\gamma_0^2(\gamma_\perp^2 - \gamma_0^2)}{\gamma_0^2 + \gamma_\perp^2} \sin^2(\theta) - \frac{\gamma_\perp^2(\gamma_0^2 - \gamma_\perp^2)}{\gamma_0^2 + \gamma_\perp^2} \cos^2(\theta) \quad (5.16)$$

The variation in γ_θ with axial magnetic field strength shown in figure 5.8b is similar as in the case of cylindrical cathode (i.e see figure 5.7b). However, γ_θ show a strong dependence on the angle θ between the cathode surface and magnetic field lines. The variation in γ_θ for a range of oblique angle θ is shown in figure 5.8b. The case $\theta = 0$ corresponds to cylindrical HC, which show a sharp fall in the secondary electron emission than conical cathode cases for three different apex angles.

5.2.3 Cathode fall characteristics in presence of magnetic field

Since the magnetic field impacts the secondary electron emission γ_{se} , it can be combined with the Paschen like relationship in section-5.1 (i.e. equation 5.12) to estimate the cathode fall thickness in the magnetized case.

As seen in figure 5.9, the characteristic curve shifts toward the right-hand side for higher magnetic field strengths. This observation is due to a considerable fall in γ_{se} as both cathode fall voltage and cathode sheath thickness increases with increase in the magnetic field. Such a discharge behavior in the presence of a magnetic field can be qualitatively related to the discharge characteristics obtained for cylindrical and conical HC source.

In figure 5.10a, it is found that the discharge current I_{dis} falls monotonically with increase in magnetic field strength for the case of cylindrical HC; whereas, I_{dis} remain almost constant up to ~ 25 mT for conical HC. In the experiment, it was found that the discharge could be sustained for a limited range of B-field for the case of a cylindrical HC source corresponding to a neutral gas pressure of 1.4 Pa. It is also found that above a critical magnetic field (i.e. $B = 17.16$ mTesla), the discharge could not be sustained for this case. This region is shown by shaded region in figure 5.10.

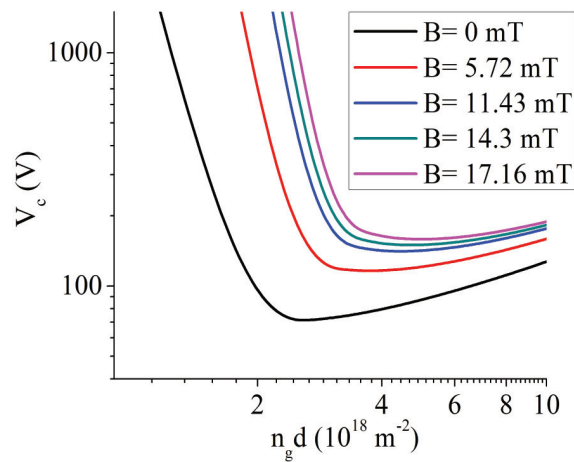


Figure 5.9: The Paschen relation indicating the effect of magnetic field on the cathode fall characteristics of an Argon discharge.

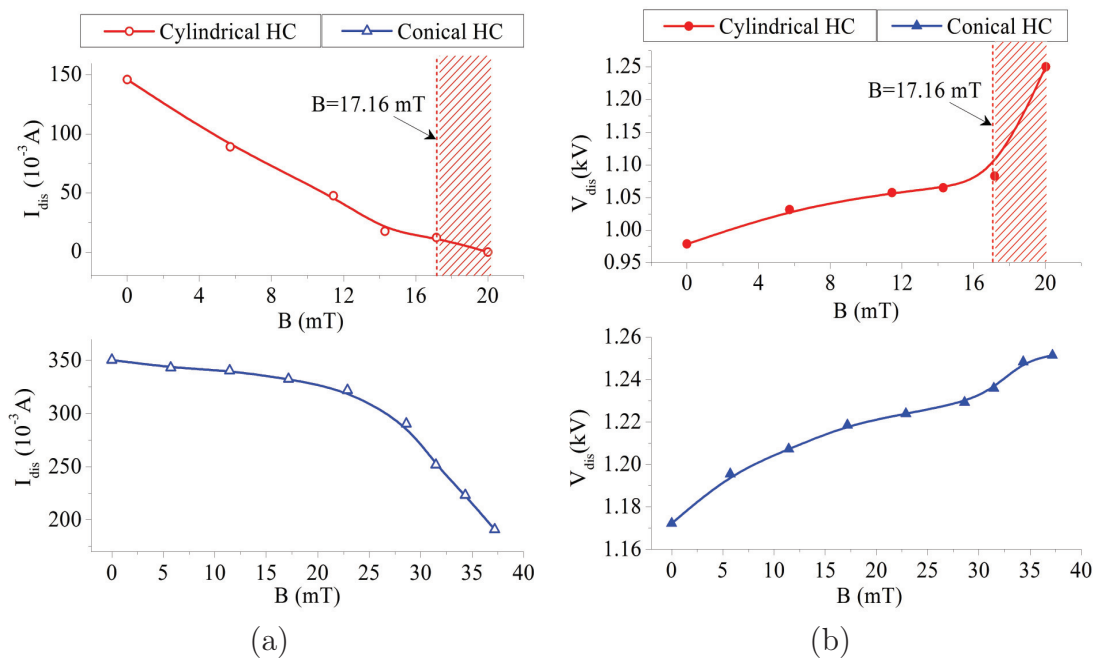


Figure 5.10: (a): Variation in discharge current at 1.4 Pa with an axial magnetic field. (b): Variation in discharge voltage at 1.4 Pa with an axial magnetic field.

The fall in I_{dis} with increase in B-field is caused due to reduction in net secondary electron emission yield γ_{se} and increase in cathode sheath thickness " d " as inferred from the characteristic curve in figure 5.9. Also, as the secondary electron emission is hindered by the application of a magnetic field, correspondingly a higher value of cathode fall voltage drop V_c is required for extracting the secondary electrons.

As seen in figure 5.10b, the sustenance voltage V_{dis} between the discharge electrodes increases with increase in B-field. Hence variations in electrical discharge characteristics observed in experiments are in qualitative agreement with the Paschen like curve shown in figure 5.9. Here the characteristic curve shift towards the right-hand side for increasing values of magnetic field strength. Therefore, it can be inferred that an optimal balance between the gas neutral pressure and B-field is required to sustain the discharge for the case of cylindrical HC source specially for higher magnetic field strengths.

For the case of conical cathode, secondary electron emission yield gets enhanced as the apex angle θ is increased (i.e see figure 5.8b). This fact can be observed in figure 5.10, where the conical HC source sustains the discharge over a broader range of magnetic field as compared to the cylindrical HC for a similar operating gas pressure of 1.4 Pa.

5.3 Results and Discussion

In figure 5.11, it is observed that the sustenance / discharge voltage V_{dis} for the conical hollow cathode increases, whereas discharge current I_{dis} reduces with the increase in magnetic field strength for a range of neutral gas pressure.

The net current density at the cathode surface can be expressed in terms of cathode sheath thickness " d " and secondary electron emission yield γ_{se} as [1, 18];

$$j_{dis} = \frac{2\epsilon_0 V_c V_i}{d^2} (1 + \gamma_{se}) \quad (5.17)$$

The discharge current density at the cathode can be estimated as $j_{dis} = I_{dis}/A_C$ (where A_C is cathode area). Considering the cathode fall voltage $V_c \approx V_{dis}$; then

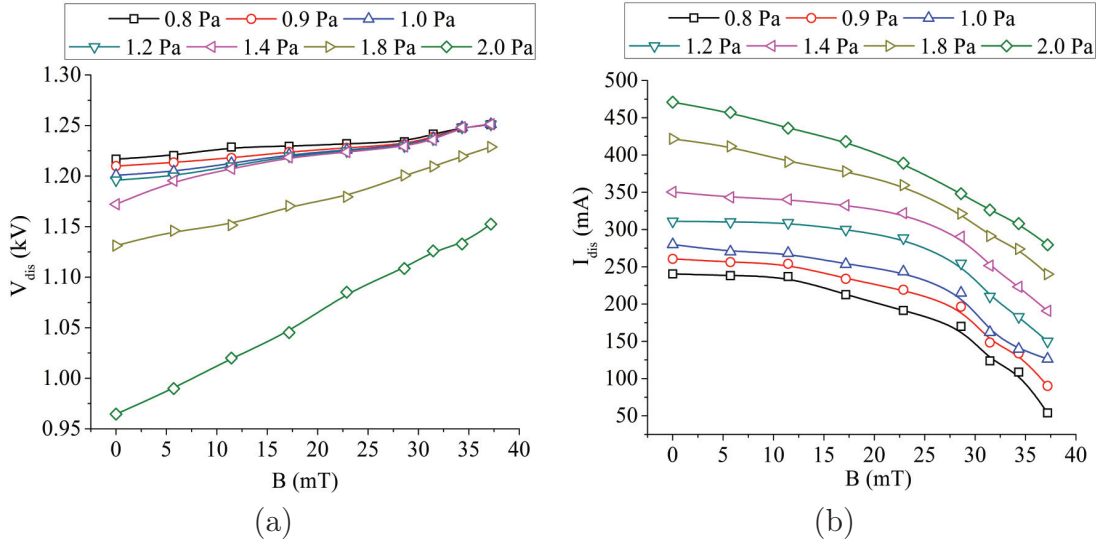


Figure 5.11: (a): Discharge voltage as a function of axial magnetic field for a range of neutral gas pressure. (b): Discharge current as a function of axial magnetic field for a range of neutral gas.

the non-linear equations 5.12 and 5.17 can be numerically solved to obtain the values of the cathode sheath thickness " d " and secondary electron emission yield γ_{se} corresponding to the given experimental conditions of neutral gas pressure and magnetic field strength.

The effects due to external magnetic field strength and neutral gas pressure is intrinsic in the observed experimental trends of discharge voltage and current in figure 5.11. Also, to obtain the numerical solution the ion velocity V_i is assumed in the range; $\sqrt{eT_e/m_i} \leq V_i \leq \sqrt{2eV_C/m_i}$.

The experimental values of secondary electron emission yield γ_{se} and cathode sheath thickness " d " are shown in figure 5.12. It can be seen that over a given range of operating gas pressure, the cathode sheath width increases with a corresponding fall in secondary electron emission yield. These results are in qualitative agreement with the phenomenological model presented in the previous section-5.2 that considers a similar reduction in γ_{eff} because of increase in recapture of electrons at the cathode for the case of tangential/oblique magnetic field at the hollow cathode surface.

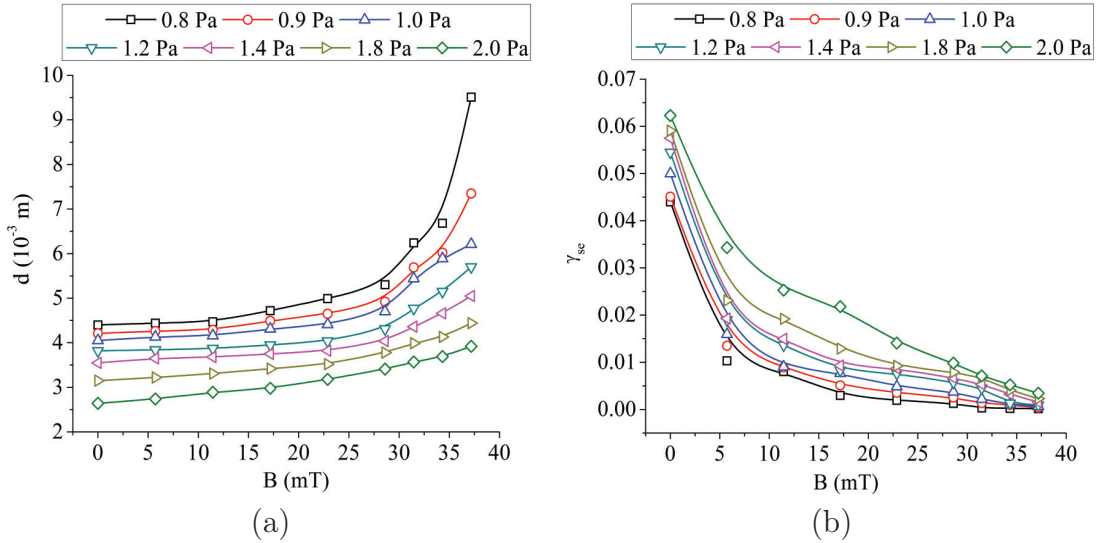


Figure 5.12: (a): Cathode fall thickness as a function of axial magnetic field for a range of neutral gas pressure. (b): Secondary electron emission yield as a function of axial magnetic field for a range of neutral gas pressure.

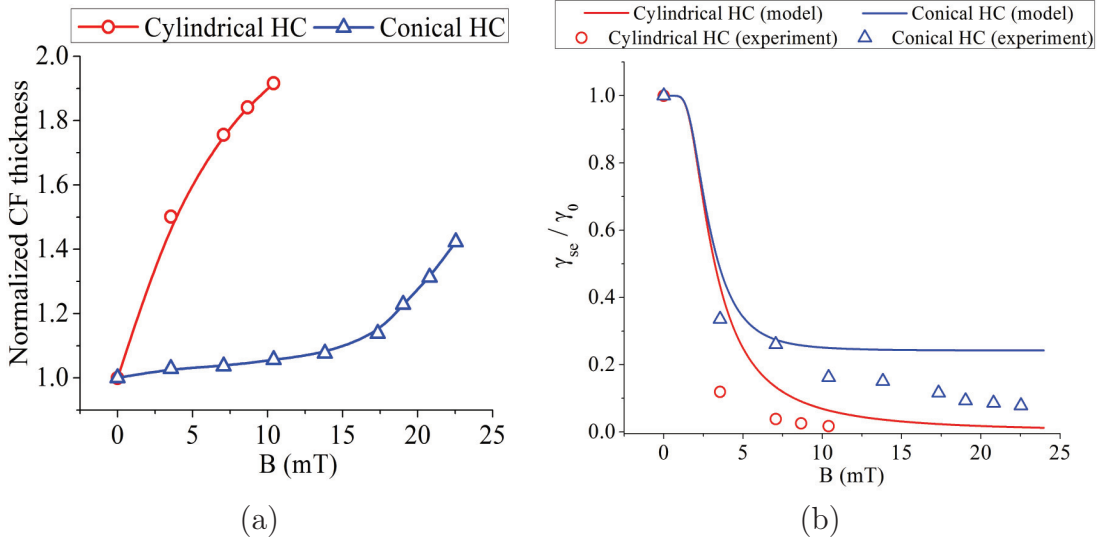


Figure 5.13: (a): Cathode fall thickness as a function of an axial magnetic field at a neutral gas pressure 1.4 Pa. (b): Effective secondary electron emission yield as a function of an axial magnetic field at a neutral gas pressure of 1.4 Pa. All the parameters are normalized with the respective experimental values in absence of magnetic field.

The electrical discharge properties in figure 5.10 depicts that the effect of axial magnetic field is different for the case of cylindrical and conical HC source. The experimental and modeling results of the cathode fall characteristics are shown in figure 5.13 for the respective plasma sources.

It is found that for given neutral gas pressure, the magnetization effect on cathode fall thickness " d " is significantly higher for the case of cylindrical HC as the magnetic field lines are tangential to the HC surface. Whereas, for the conical HC, the cathode sheath thickness has a marginal increase with the magnetic field. It can be observed in figure 5.13b that oblique magnetic field at conical cathode results in higher values of γ_{se} relative to the cylindrical case. Therefore, a conical HC source can sustain the discharge over a wide range of axial magnetic field strength as compared to the cylindrical hollow cathode at similar operating gas pressure [18].

Summary and conclusion

In summary, the effect of the axial magnetic field and neutral gas pressure on secondary electron emission characteristics is obtained for the cylindrical and conical hollow cathode. The experimental results obtained in this study have been explained with help of a phenomenological model that has been developed to study the behavior of secondary electron emission yield from an oblique cathode surface w.r.t an axial magnetic field. Using the model the electron recapture probabilities at the cathode surface, the behavior of cathode fall thickness and secondary electron emission yield has been studied for a range of neutral gas pressure and axial magnetic field strength for respective hollow cathode geometries (i.e. cylindrical and conical hollow cathodes in presence of axial B-field). For both the plasma sources, it is experimentally demonstrated that the sustenance voltage across the discharge electrodes increases whereas, the discharge current reduces as a function of the axial magnetic field. This experimental information is further used in the model to estimate the variation in secondary electron emission yield and cathode fall thickness for both the above plasma sources.

6

Radial Characteristic of Hollow Cathode produced Magnetized Plasma Column

Magnetized plasma column confined in a linear plasma device has significance in both fundamental research [16, 17, 79, 80]; as well as applications towards high heat flux experiments on plasma-facing components related to fusion technology [81, 82]. The well-known plasma source used in such devices is a reflex arc, which is based on hot cathode electron emitter [14]. The life-time of such sources is limited due to erosion of the filament cathode; beside significant power loss takes place due to radiation and heating of the chamber walls [15]. Cold hollow cathode discharge can be used as a substitute for the hot electron emitter for the production of a stable magnetized plasma column in linear device [20, 83].

This chapter devotes to the magnetized plasma production using a cold hollow cathode discharge and its characterization in a linear plasma device [16–18]. In particular, the effect of the hollow cathode geometry on the radial properties of the downstream plasma column is investigated and its performance is qualitatively interpreted with the help of a phenomenological model [18].

In section-6.1, the underlying concept behind the ionization inside the hollow cathode cavity is introduced. Experimental results on radial plasma characteristics are

presented in section-6.2. A phenomenological model based on plasma fluid approximation is developed in section-6.3 for the radial plasma characteristics in the downstream plasma region. The experimental and modeling results are qualitatively compared and discussed in section-6.4. Finally, the summary and conclusion of this study are provided at the end of the chapter.

6.1 Ionization mechanism inside cylindrical and conical hollow cathode

In figure 6.1, the schematic shows the lateral cross-section for cylindrical and conical hollow cathode geometries along with the constricted anode. The magnetic field is assumed along the z-axis. A high voltage applied between the Anode (A) and the Cathode (HC) results in a discharge that is primarily concentrated inside the respective hollow cavities. Note that in presence of an axial magnetic field, the secondary electrons emerging from the cathode sheath undergo $\vec{E} \times \vec{B}$ drift in the azimuthal direction w.r.t the magnetic field lines. The axial magnetic field lines will limit the cross-field transport of the electrons towards the central region. Therefore, for the case of cylindrical HC in figure 6.1a; these energetic electrons are primarily concentrated in the off-central region, i.e, closer to the HC surface. However, in the case of a conical cathode (i.e. see figure 6.1b), the concentration of these off-centered energetic electron groups will vary with axial distance from the anode. As a result, these electrons are more populated in the entire region of the conical hollow cathode than the cylindrical case.

As the energetic electrons undergo elastic / inelastic / ionizing collisions with background neutrals, it crosses the magnetic field lines and finally returns to the centrally located anode by flowing along the magnetic field [17, 18]. In the case of a conical cathode, a component of the sheath electric field $E\hat{z}$ along the magnetic field line facilitates the escape of secondary electrons from the cathode surface unlike the case of the cylindrical cathode. Therefore the radial plasma characteristics in the downstream plasma region are expected to be different for the cylindrical and the conical hollow cathode sources.

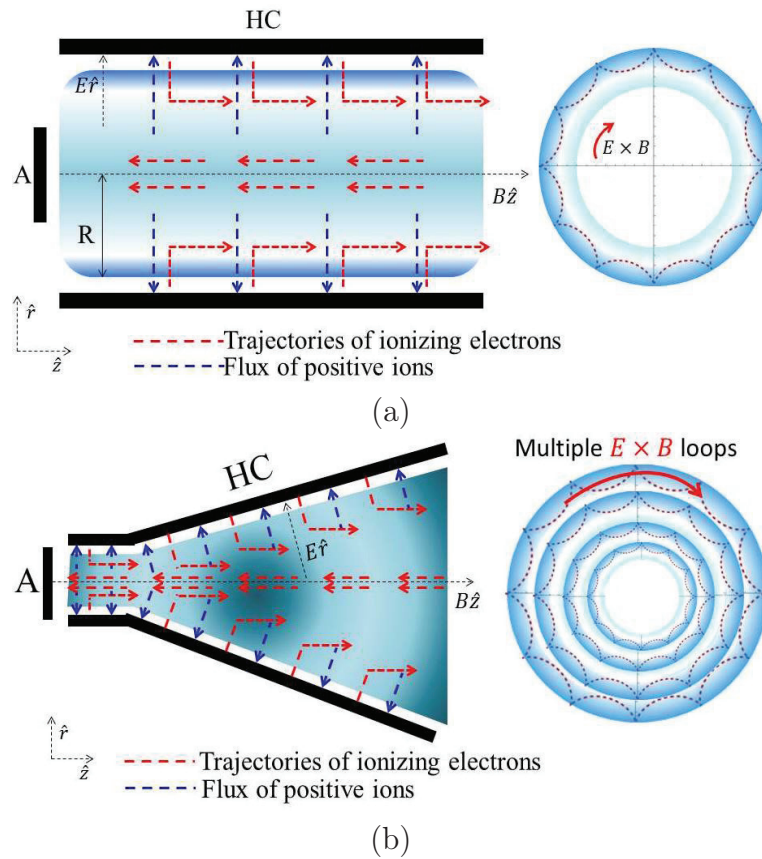


Figure 6.1: (a): Possible ionization mechanism inside a cylindrical hollow cathode cavity in presence of axial magnetic field. (b): Possible ionization mechanism inside a conical hollow cathode cavity in presence of axial magnetic field.

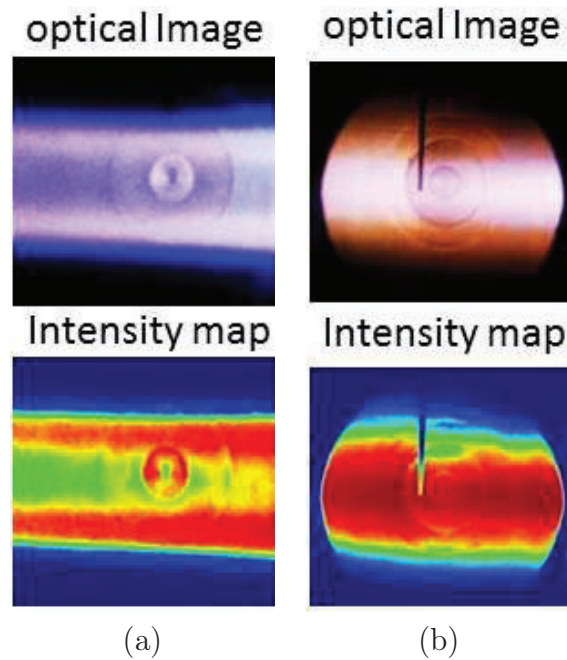


Figure 6.2: (a): Optical image and intensity map of magnetized plasma column by a cylindrical HC source at 17.16 mT and operating pressure of 1.4 Pa. (b): Optical image and intensity map of magnetized plasma column by a conical HC source at 17.16 mT and operating pressure of 1.4 Pa.

Figure 6.2 present the optical image of downstream plasma column taken from the lateral window of the linear plasma device (i.e. at $z = 30$ cm in schematic figure 2.8a). As observed in the case of a cylindrical cathode, the image of the plasma column is more intense in the off-centered region, highlighting the presence of energetic electrons close to the cathode surface inside the cylindrical HC cavity. On the other hand, the light intensity is uniform in the downstream plasma column when the conical HC source is used. This observation suggests that the energetic ionizing electrons are present in the entire volume inside the conical hollow cathode cavity.

6.2 Radial plasma characteristics in the downstream region

The radial plasma characteristics measured at $z = 30$ cm distance from the anode (i.e. see schematic figure 2.8a and 2.9b) in the downstream plasma region outside the respective HC's are presented. The experiments are carried at a fixed neutral pressure of 1.4 Pa in pure Argon gas.

6.2.1 Radial plasma characteristics of a cylindrical hollow cathode source

The collage of radial profile of ion plasma density, bulk electron temperature and radial plasma potential are all shown in figure 6.3a; whereas figure 6.3b plots the radial density and temperature distribution for the hot electron population in the downstream plasma column. These experimental results can be summarized as follows:

In figure 6.3a, the positive ion density show a maxima in the central region when the magnetic field is absent, while the density peak shift to off-central region with the application of magnetic field. On the other hand the overall bulk electron temperature and plasma potential show a peak in the central part for $B=0$ case, which eventually reduces with increase in magnetic field.

However in figure 6.3b the electron density corresponding to the hot electron fraction show some interesting characteristics. It is found that the plasma column consists of a significant population of hot electrons in the downstream region. In the figure 6.3b, the off central region is found to be hotter than the center, whereas the population of hot electrons seems to be larger in the center than at the edge. The peak temperature is found to be near the outer periphery of the plasma column, i.e $r = \pm 3.5$ cm (i.e. in the source region, this location corresponds to the inner surface of the hollow cathode cylinder). Also with an increase in the axial magnetic field, the hot electron temperature in the central region gets reduced.

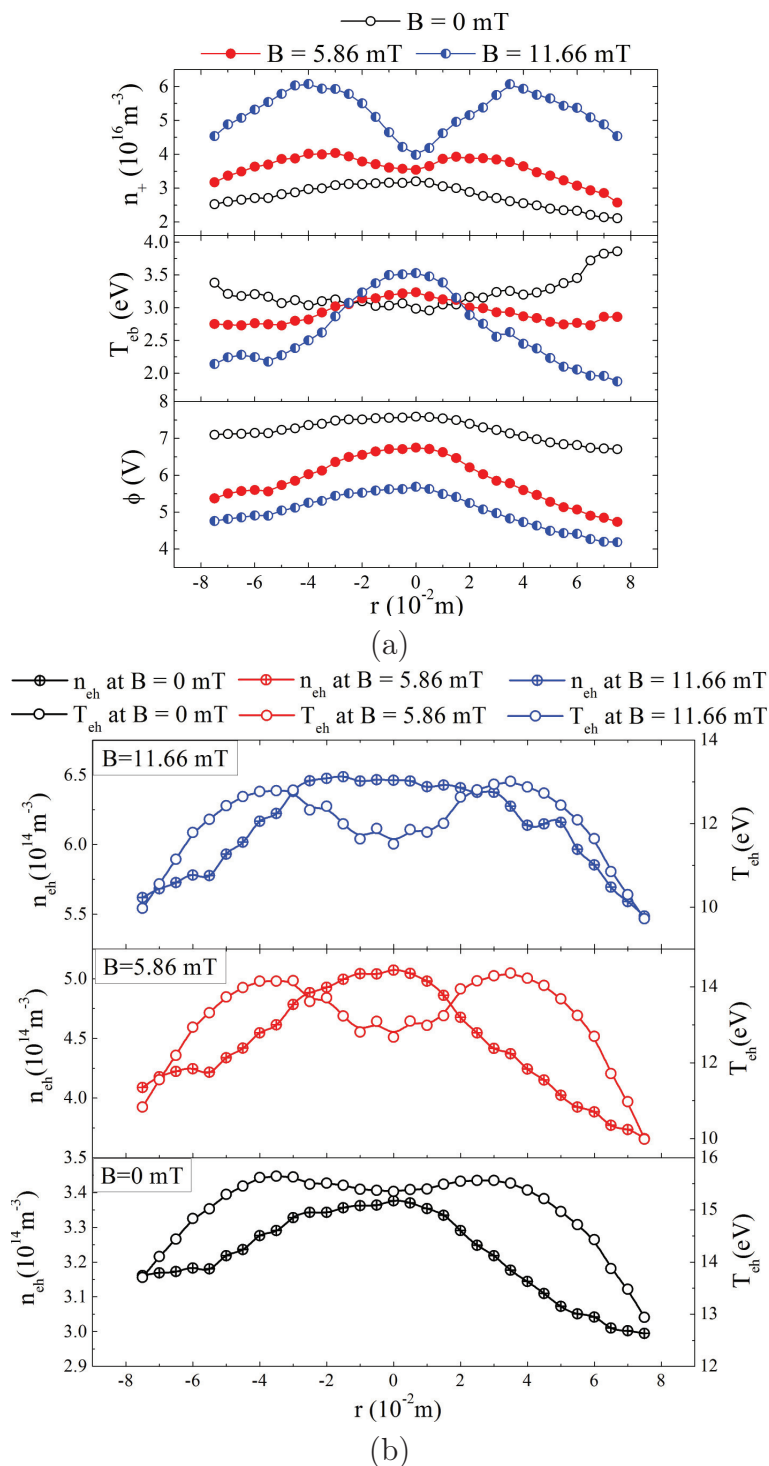


Figure 6.3: (a): Radial profile of ion density n_+ , bulk electron temperature T_{eb} and plasma potential ϕ at axial location $z = 30$ cm for cylindrical HC plasma source. (b) Radial profile of hot electron density n_{eh} / temperature T_{eh} at axial location $z = 30$ cm for cylindrical HC plasma source.

The above observation in figure 6.3 throws light on a possible mechanism by which the downstream plasma column is sustained under the application of an axial magnetic field to the hollow cylindrical cathode. As the concentration of secondary electrons is more in the peripheral region, it gives rise to intense excitation of the background gas, hence the plasma column appears brighter as evinced in figure 6.2a. A fraction of these energetic electrons will flow along the magnetic field leading to ionization along the magnetic field lines closer to the HC surface. Thus the positive ion density shows an off-centered peak in figure 6.3a. The energetic electrons constitute a current through the plasma column by flowing along an axial electric field towards the centrally located anode. The hot electron population is higher in the central region but their temperature T_{eh} is smaller in magnitude as compared with the peripheral region. This observation suggests that these electrons reach the axis of the plasma column by undergoing a random walk process via collisions with background neutrals [17, 18]. Therefore the energy of these hot electrons decreases in the central region inside the plasma column as evinced in figure 6.3b. Hence a hollow plasma column is observed with a cylindrical hollow cathode source in the downstream region (i.e. observed in figure 6.2a).

6.2.2 Radial plasma characteristics of a conical hollow cathode source

In figure 6.4, the radial characteristics are presented for the conical hollow cathode source. Unlike the cylindrical case, the plasma column produced by conical HC has a single temperature electron population. This observation clearly suggests the presence of a hot electron component is in the region inside the HC cavity as they emerge at an oblique angle from the entire conical cathode surface. Since these energetic electrons are responsible for carrying out the ionization in the discharge, a radially uniform ionization takes place inside the conical HC cavity [18]. As a result, the bulk plasma temperature and plasma potential are radially uniform in the absence of a magnetic field (i.e. $B=0$ case). However, as the axial magnetic field is introduced there is a gradual formation of temperature and potential peak at the center of the plasma column along with the peak in plasma density. Therefore, as observed in 6.2b the downstream plasma column is more intense at the center and its intensity reduces marginally in the peripheral region.

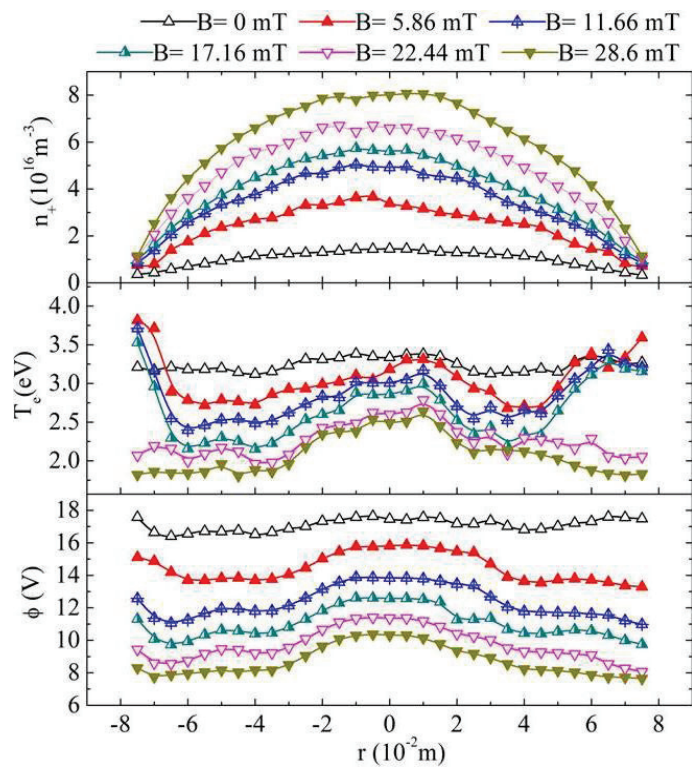


Figure 6.4: Radial profile of ion density n_+ , bulk electron temperature T_{eb} and plasma potential ϕ at axial location $z = 30$ cm for conical HC plasma source.

6.3 Phenomenological model: Radial plasma properties

For obtaining the radial plasma density, the ionization caused by the energetic electrons inside the cylindrical plasma volume is described by the ion continuity and momentum equations [6, 18, 53];

$$\frac{1}{r} \frac{\partial}{\partial r} r(n_i V_i) = S \quad (6.1)$$

$$m_i \frac{\partial}{\partial r} (n_i V_i^2) = e n_i E \quad (6.2)$$

In equation 6.1, n_i and V_i represent the positive ion density and its velocity, S is the ionization source term expressed as $S = n_i \nu_{iz} = n_e \nu_{iz}$, where ν_{iz} is the frequency of ionization [1]. Considering that ions are un-magnetized in the system, the ion momentum equation reduces to equation 6.2, where m_i is the ion mass, e is the electron charge and E is the local electric field inside the plasma volume. The radial component of this electric field can be derived from the plasma potential ϕ as $E = -\frac{\partial \phi}{\partial r}$.

Introducing the ion current density $j_i = e n_i V_i$ in equations 6.1 and 6.2; the equation for the radial ion current and the ion density are expressed respectively as;

$$\frac{\partial j_i}{\partial r} + \frac{j_i}{r} = e S \quad (6.3)$$

$$\frac{\partial n_i}{\partial r} + \frac{2n_i}{r} = \left(\frac{n_i}{j_i} \right)^2 \left[\frac{2e S j_i}{n_i} + \frac{e^3 n_i}{m_i} \frac{\partial \phi}{\partial r} \right] \quad (6.4)$$

For the magnetized electrons the radial current density j_e is obtained using the drift-diffusion equation;

$$j_e = e n_e \mu_{\perp} E + e D_{\perp} \frac{\partial n_e}{\partial r} \quad (6.5)$$

In the above equation D_{\perp} and μ_{\perp} are respectively the diffusion and mobility perpendicular to the axial magnetic field. These quantities are related using Einstein equation i.e. $D_{\perp} = \mu_{\perp} (kT)/e$; where, $(kT)/e$ is equivalent to temperature T_e in Volts [1].

The electron mobility is expressed as, $\mu_{\perp} = \frac{e}{m\nu_m} [1 + \frac{\omega_{ce}^2}{\nu_m^2}]^{-1}$, where ν_m is the electron-neutral collision frequency and $\omega_{ce} = \frac{eB}{m}$ is electron gyro-frequency; B is the axial magnetic field strength and m is the electron mass. On substituting $D_{\perp} = \mu_{\perp}(kT)/e$ in equation 6.5, a differential equation governing radial density variation can be written as follows:

$$\frac{\partial n_e}{\partial r} - \frac{1}{T_e} \frac{\partial \phi}{\partial r} n_e = \frac{H}{T_e} j_e \quad (6.6)$$

In equation 6.6, J_e is the net electron current density inside the discharge and H is the magnetization parameter which is approximated from Bohm diffusion as, $H = \frac{m\nu_m}{e^2} [1 + \frac{\omega_{ce}^2}{\nu_m^2}] \approx 1.6 \frac{B}{e}$; where it is assumed that $\omega_{ce} \gg \nu_m$ according to the present experimental condition [18].

The potential distribution inside the discharge can be obtained by using the Poisson's equation;

$$\frac{\partial^2 \phi}{\partial r^2} + \frac{1}{r} \frac{\partial \phi}{\partial r} = \frac{e}{\epsilon_0} (n_e - n_i) \quad (6.7)$$

The above formulated ion and electron transport equations (i.e. 6.3, 6.4 and 6.6) coupled with the Poisson's equation (i.e. 6.7) can be solved numerically to obtain the radial plasma density profile for the case of cylindrical HC under the effect of axial magnetic field.

In contrast to the cylindrical HC case, the phenomenological model assumes that the ionization is radially uniform for the case of conical cathode. Assuming the ionization source term as $S_0 = n_0 \nu_{iz}$, with n_0 as the central plasma density and ν_{iz} as ionization frequency; the radial variation in j_i and n_i given in equations 6.3 and 6.4 can be rewritten with a constant source term S_0 for conical case. The electron continuity equation can be written as;

$$\frac{1}{r} \frac{\partial}{\partial r} r(j_e) = eS_0 \quad (6.8)$$

Combining the electron transport and continuity equations (i.e. equations 6.5 and 6.8), a second order differential equation can be obtained which governs the radial

Table 6.1: Experimental values J_e , ϕ_0 , n_0 and T_e for different axial magnetic field in the case of cylindrical HC.

B (mT)	$T_{e(hot)}$ (V)	$n_{0(hot)}$ (m^{-3})	ϕ_0 (V)	n_0 (m^{-3})	$j_e \approx en_{0(hot)} \sqrt{\frac{8eT_{e(hot)}}{\pi m}}$ (Am^{-2})
0	14.98	3.37×10^{14}	7.59	3.2×10^{16}	69.83
5.86	13.12	5.07×10^{14}	6.75	3.54×10^{16}	98.16
11.66	11.95	6.46×10^{14}	5.68	3.98×10^{16}	119.38

Table 6.2: Experimental values ϕ_0 , n_0 and S_0 for different axial magnetic field in the case of conical HC.

B (mT)	ϕ_0 (V)	n_0 (m^{-3})	S_0 ($m^{-3}s^{-1}$)
0	17.46	1.44×10^{16}	1.2×10^{21}
5.86	15.81	3.38×10^{16}	3.5×10^{22}
11.66	13.83	4.91×10^{16}	5.2×10^{22}
17.16	12.57	5.6×10^{16}	6.2×10^{22}
22.8	11.36	6.58×10^{16}	7.5×10^{22}
28.6	10.31	7.98×10^{16}	9.3×10^{22}

electron distribution in the magnetized plasma;

$$\frac{\partial^2 n_e}{\partial r^2} + \left(\frac{1}{r} - \frac{1}{T_e} \frac{\partial \phi}{\partial r} \right) \frac{\partial n_e}{\partial r} - \frac{1}{T_e} \frac{\partial \phi}{\partial r} \frac{n_e}{r} = \frac{1}{T_e} \left(\frac{\partial^2 \phi}{\partial r^2} n_e - eS_0 H \right) \quad (6.9)$$

In a similar approach to the cylindrical case, the above fluid equations with constant ionization source term can be solved to obtain the radial plasma density profile for conical HC case under the effect of axial magnetic field.

These fluid equations can be simultaneously solved with the values of external parameters and required boundary conditions obtained from the experiments using cylindrical and conical HC source respectively. The above fluid model is phenomenologically correlated with the ionization process taking place inside the source cavity. Therefore, the model qualitatively includes the effect of HC geometry and axial magnetic field on the radial density profile of the plasma column.

6.4 Results and Discussion

For the case of cylindrical HC source, the formulated fluid equations (i.e. 6.3, 6.4, 6.6 and 6.7) can be numerically solved with the experimental boundary conditions and the parameters listed in table 6.1. Similarly for the case of conical cathode, the respective fluid equations (i.e. equations 6.3 and 6.4 with constant ionization source term S_0 along with equations 6.7 and 6.9) can be numerically solved with the required experimental parameters given in table 6.2.

In figure 6.5, the modeling results are shown along with the scattered experimental data points for each case. In the case of cylindrical HC as observed in figure 6.5a, the plasma density shows a transition from a centrally peaked profile to a saddle-like structure with an increase in magnetic field strength. In presence of an axial magnetic field, the hollow/or a saddle-like density profile is more eminent as ionization gets localized near the cylindrical HC surface. This experimental and modeling results along with the optical image of the plasma column in figure 6.2a suggests that the energetic electrons from the inner wall of the cylindrical cathode have to undergo several ionizing collisions along the magnetic field lines before it reaches to the discharge axis.

However as observed in figure 6.5b for the conical case, both modeling and experimental results show a centrally peaked density profile. In presence of an axial magnetic field, the tapered cathode geometry enables the injection of ionizing electrons from the entire cathode surface and they eventually flow along the magnetic field lines and contribute to the ionization process in the entire volume. Therefore, owing to the uniform ionization inside the conical hollow cathode cavity a centrally peaked plasma density profile is observed in its plasma column. This fact is also evinced from the image of the magnetized plasma column in figure 6.2b, where intensity marginally reduces in the peripheral region.

In figure 6.5 it can be seen that the radial plasma density decays rapidly and in the downstream region, as the plasma diverges, the plasma column spreads beyond the cathode diameter. Although these results are in qualitative agreement, it can be observed that experimental results deviate from the modeling plots near

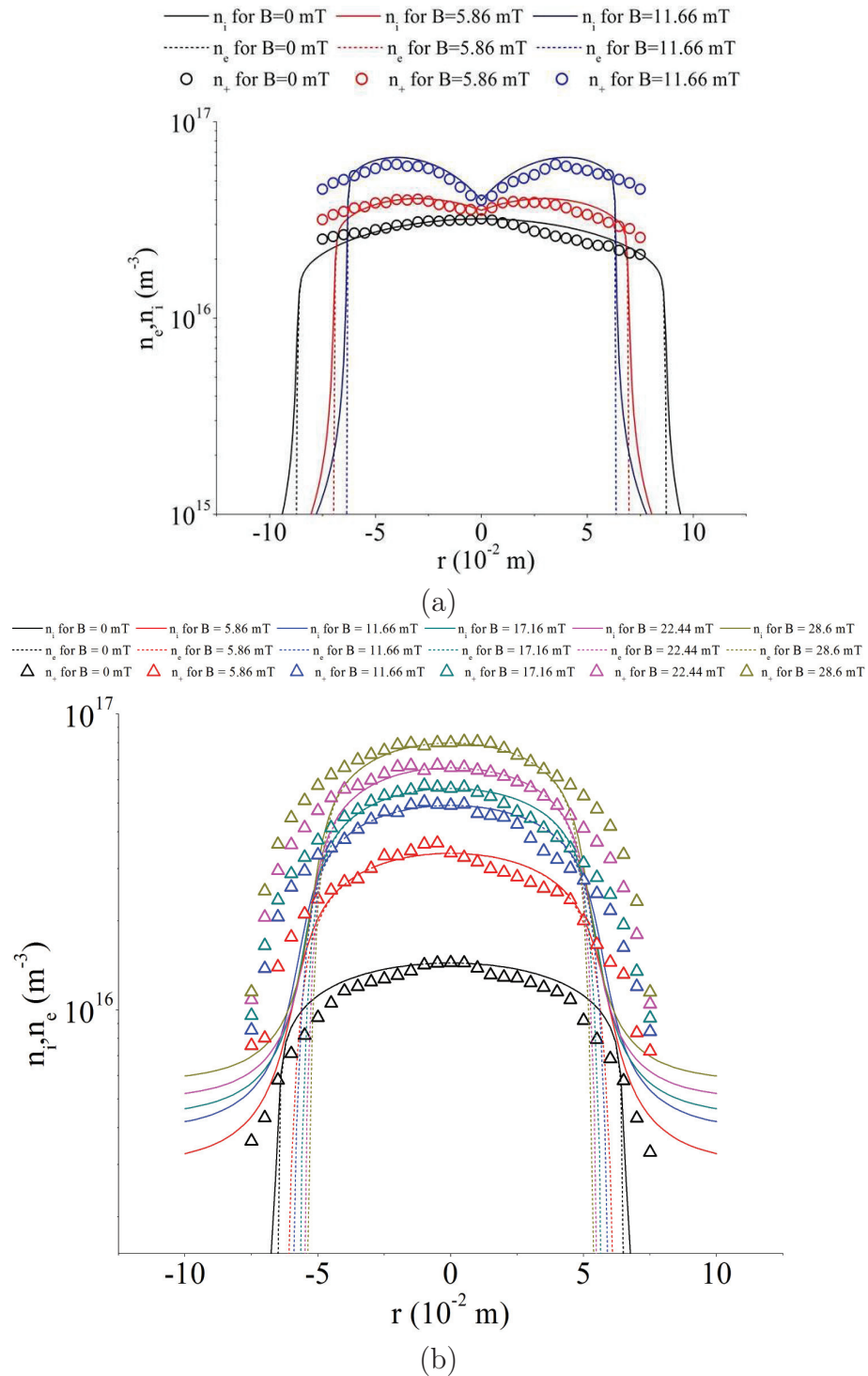


Figure 6.5: (a): Radial density profile for cylindrical HC for boundary conditions and experimental parameters given in table 6.1. (b): Radial density profile for conical HC for experimental parameters given in table 6.2. The scattered points represents the experimental values for each case.

the edge of the plasma column for respective cases (i.e. the point where quasi neutrality break). It is also found that with the increase in the axial magnetic field, the plasma column appears to shrink radially for each case. The decrease in the radius of the plasma column can be directly correlated with cathode fall thickness, which tends to increase inside respective cathode cavities as secondary electron emission yield gets reduces under the effect of axial B-field. These observations are in qualitative agreement with the experimental and modeling results of the cathode fall region presented in previous chapter (i.e. plots in figures 5.12 and 5.13).

Summary and conclusion

In summary, the radial properties of the magnetized plasma column produce by a different type of hollow cathode geometry are presented along with a phenomenological model to support the experimental trends. It is concluded that the choice of particular electrode geometry and the axial magnetic field can control the radial electron temperature and density inside the magnetized plasma column. Also, the experimental results suggest that the ionizing electrons from the cathode can be steered along the magnetic field to produce an elongated plasma column in the downstream plasma region. The oblique magnetic field at the cathode surface also enables better extraction of secondary electrons from the cathode surface through a component of the electric field that injects the electrons axially along the magnetic field lines. As a result, an elongated plasma column having a central density peak can be achieved. Furthermore, the discharge can be sustained at stronger magnetic field strengths using a conical hollow cathode geometry as discussed in chapter-5.

7

Elongated Plasma production using Magnetized Hollow Cathode

The present chapter unravels the dynamics behind the creation of an elongated plasma column by a beam of energetic plasma electrons provided from the HC plasma source. In particular, a configuration of a cylindrical hollow cathode with a centrally located constricted anode at one end of the cathode axis is presented. It is shown that this configuration allows the secondary electrons from the hollow cathode to follow an elongated trajectory along the axial magnetic field lines. These energetic electrons provide the necessary $I_{dis}^2 R_p$ Ohmic heating for sustaining the magnetized plasma column at low operating pressures [17].

The experimental findings are corroborated by formulating a phenomenological model. It is established that the primary electrons constituting the discharge current expand throughout the downstream region, giving rise to the ionization in the entire plasma column. Using the phenomenological model an empirical relationship between the characteristic plasma column length and the axial magnetic field is established [17].

Section-7.1 presents an equivalent electrical circuit model of the discharge using which the gross plasma parameters are estimated. The detailed measurements of axial plasma parameters are presented in section-7.2. The discharge mechanism inside the plasma column is depicted through a phenomenological model in section-

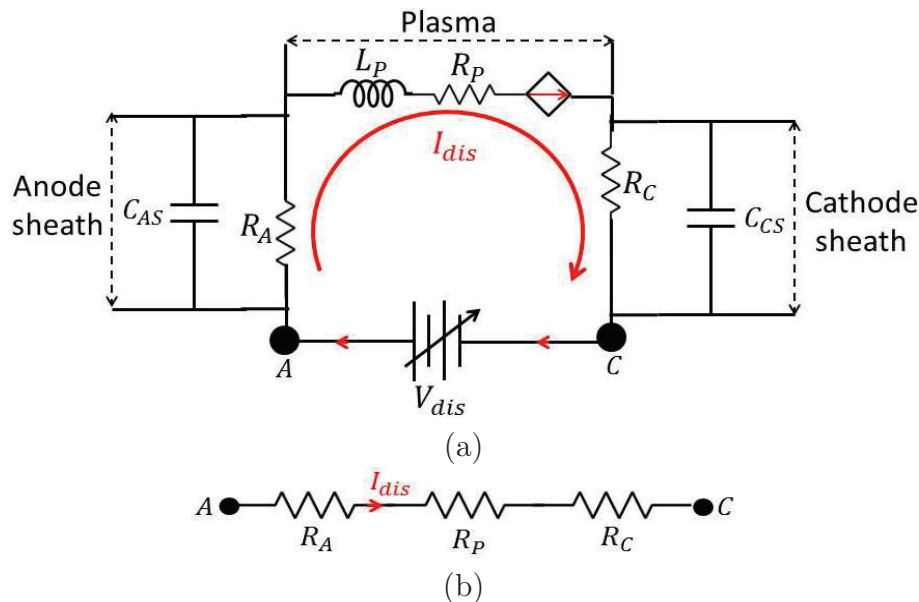


Figure 7.1: (a): Electrical analogy of a discharge between anode "A" and cathode "C". (b): Equivalent electrical circuit of a DC discharge in equilibrium state.

7.3. The experimental and the modeling results are finally discussed in section-7.4, and summarized at the end of the chapter.

7.1 The discharge circuit model

Consider the electrical analogy of the discharge circuit shown in figure 7.1a. The circuit is a complex network of lumped electrical components corresponding to the individual sheath (i.e. cathode "C" and anode "A" sheaths) and plasma region. The sheath capacitance across the anode and the cathode are represented as C_{AS} and C_{CS} respectively. The plasma inductance is L_p and resistance corresponding to bulk plasma is R_p and sheath region is R_A and R_C respectively. In steady-state equilibrium, the reactive components (i.e. sheath capacitance and plasma inductance) vanishes such that the discharge can be represented as a series combination of resistive components corresponding to the sheath region and a bulk plasma region as shown in figure 7.1b. The net discharge current I_{dis} flows through the anode sheath resistance R_A , bulk plasma resistance R_p and cathode sheath resistance R_C . The net power $I_{dis} * V_{dis}$ dissipated in the discharge is a summation of the power dissipated across the individual sheaths and inside the plasma column.

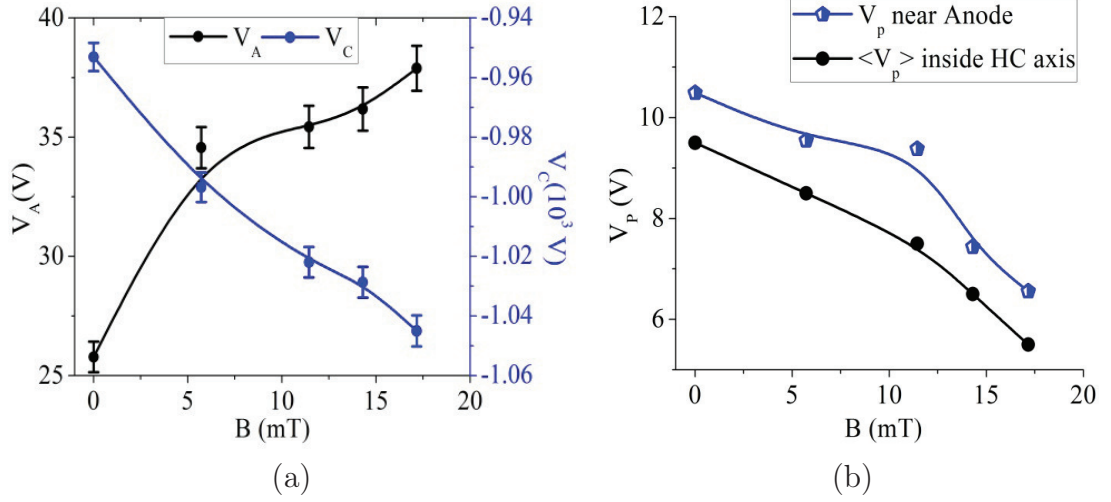


Figure 7.2: (a): Effect of axial B-field on cathode and anode potential measured w.r.t the ground. (b): Plasma potential in the discharge as a function of axial magnetic field for a neutral gas pressure of 1.4 Pa.

The experiment is carried out using the cylindrical HC setup shown in figure 2.4 and figure 3.9a. The operating gas is Argon and the experimental results reported here corresponds to a fixed neutral pressure of 1.4 Pa. As shown in figure 7.2a, with increase in axial B-field, the individual electrode potential (i.e. V_A = anode potential and V_C = cathode potential) measured w.r.t ground increases. The variation in the plasma potential V_P inside HC cavity is shown in figure 7.2b. The variations in individual electrode potentials and plasma potential in figure 7.2 indicates that the cathode fall voltage drop (i.e. $\langle V_p \rangle - V_C$) increases with increase in magnetic field. The corresponding variation in discharge current I_{dis} and discharge voltage V_{dis} is provided in figure 5.10 of chapter-5.

From figure 7.1b, the anode sheath resistance R_A and cathode sheath resistance R_C can be estimated as;

$$R_A = \frac{V_A - V_P}{I_{dis}} \quad (7.1)$$

$$R_C = \frac{\langle V_P \rangle - V_C}{I_{dis}} \quad (7.2)$$

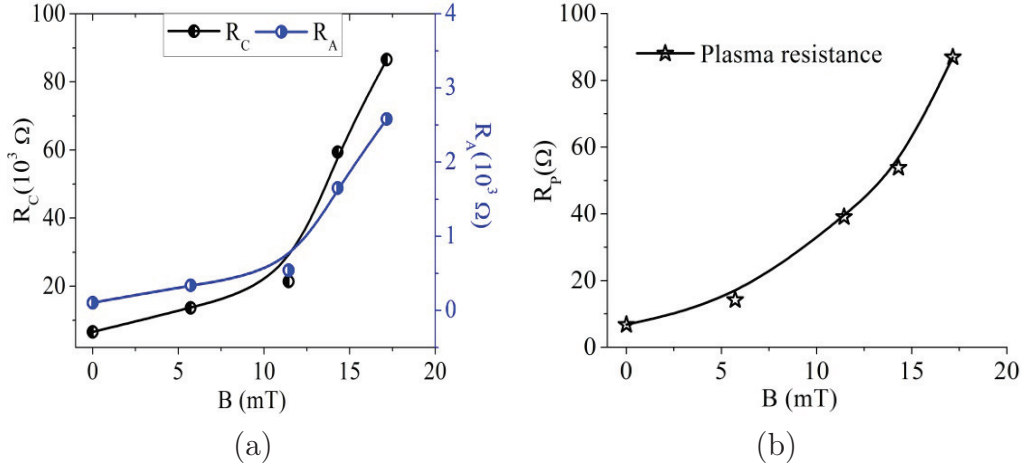


Figure 7.3: (a): Effect of axial B -field on anode sheath resistance R_A and cathode sheath resistance R_C . (b): Effect of axial B -field on Plasma resistance R_p .

In equation 7.2, $\langle V_P \rangle$ corresponds to the mean plasma potential in the bulk plasma measured w.r.t ground. The overall discharge resistance R_{dis} can be obtained as [17];

$$R_{dis} = \frac{V_{dis}}{I_{dis}} = R_A + R_p + R_C \quad (7.3)$$

Therefore, knowing $R_{dis} = \frac{V_{dis}}{I_{dis}}$ from experiment, the net plasma resistance R_p can be estimated using equation 7.3. Since R_p corresponds to the bulk plasma region and R_A , R_C corresponds to the sheath region, their variations with external electrical parameters can be grossly determined to predict the discharge behavior without relying on intrinsic plasma measurements that includes the temperature and the spatial plasma density in the discharge.

Using the data plotted in figure 5.10 and figure 7.2, above electrical parameters can be estimated under various experimental conditions. In figure 7.3a, the sheath resistances R_A and R_C are plotted as a function of magnetic field strengths. It is seen that the resistances increase with axial magnetic field strengths. The increase in R_C is quite significant, since the magnetic field lines are tangential to the cylindrical HC surface; whereas a marginal variation in R_A is observed since the magnetic field lines are normal to the anode surface. The net plasma resistance R_p obtained using equation 7.3 is plotted in figure 7.3b. It is found that the net plasma resistance increases as the magnetic field strength is increased.

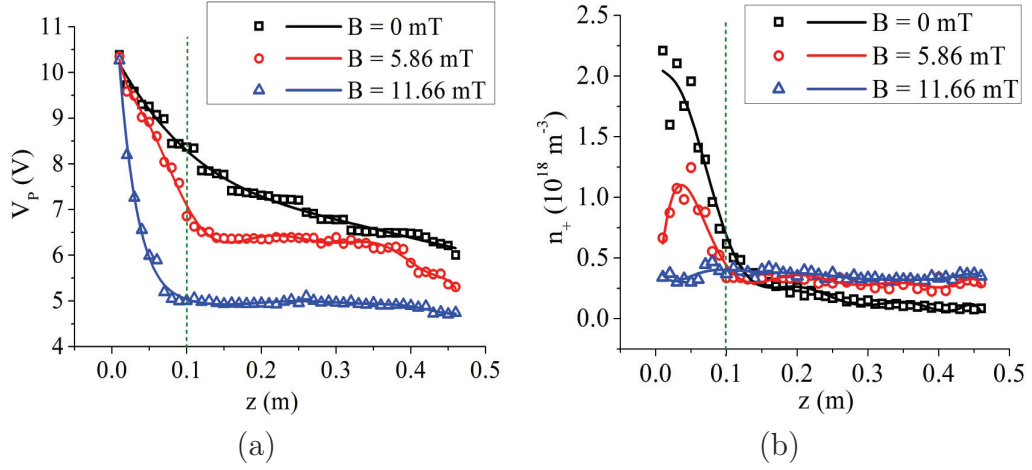


Figure 7.4: (a): Axial plasma potential along the axis of the magnetized plasma column at neutral gas pressure of 1.4 Pa. (b): Axial plasma density along the axis of the magnetized plasma column at neutral gas pressure of 1.4 Pa.

7.2 Experimental results

The variation in axial plasma potential V_P and the plasma density with reference to the anode position at the origin (i.e. at $z = 0$) is shown in figure 7.4. The dotted line at $z = 10$ cm indicates the edge of hollow cathode source.

From figure 7.4a, it is can seen that the axial electric field inside the hollow cathode region (i.e. $z < 10$ cm) increases sharply with the rise in magnetic field. Also in figure 7.4b, the peak plasma density is higher near the anode surface whereas in the downstream region (i.e. $z > 10$ cm) the plasma density show a sharp fall, more prominent in the absence of magnetic field. However as the magnetic field is applied, the density fall in downstream plasma take place gradually.

The electron population corresponding to the hot and the bulk fraction are shown in figure 7.5. As discussed in chapter-3, the effective plasma temperature T_{eff} can be calculated by equation 3.8 considering the harmonic average of bulk and hot electron populations [17, 55, 66, 67].

As shown in figure 7.5, the effective plasma temperature T_{eff} increases towards anode. However, the hot electron density n_{eh} and hot electron temperature T_{eh}

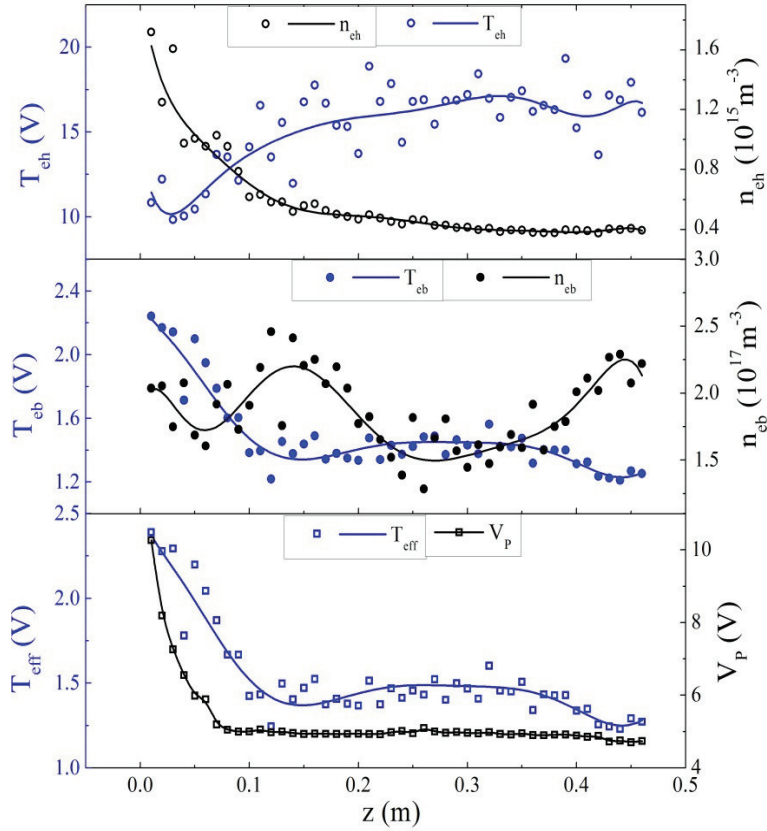


Figure 7.5: Axial profile of hot and bulk electron populations for axial B -field 11.66 mT and at neutral gas pressure of 1.4 Pa .

show a contrasting behavior in the entire plasma column. The hot electron temperature in the downstream region is higher while it falls marginally towards the anode. The hot electron density n_{eh} and plasma potential V_P show an increasing trend towards the anode from the downstream plasma region (i.e their distribution is in accordance with Boltzmann distribution). On the other hand, the bulk electrons density n_{eb} remain fairly uniform along the z -axis whereas, its corresponding bulk electron temperature T_{eb} is found to be higher inside the hollow cathode region than in the downstream plasma column.

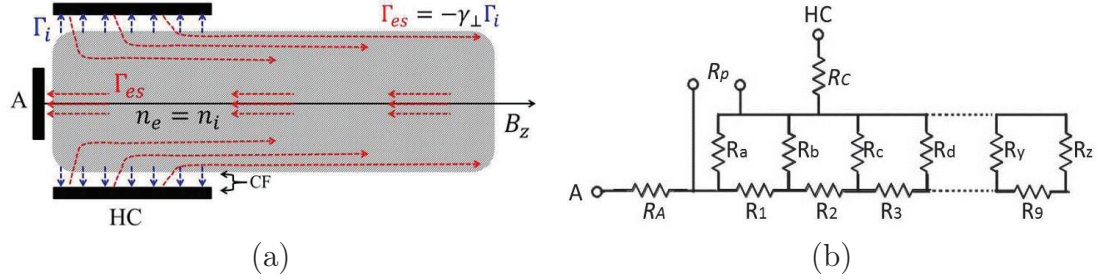


Figure 7.6: (a): Primary electron current paths in presence of magnetic field. (b): Plasma equivalent impedance circuit in presence of magnetic field with $R_A =$ Anode sheath resistance, $R_p =$ Plasma resistance having parallel components $R_{\parallel} \approx$ (ie $R_1, R_2, R_3, \dots, R_9$) and perpendicular components $R_{\perp} \approx$ (ie $R_a, R_b, R_c, \dots, R_z$), $R_C =$ Cathode sheath resistance.

7.3 Phenomenological model of a magnetized plasma column

In chapter-6, the dynamics behind secondary electron emission from the HC surface in the presence of an axial magnetic field was presented. These energetic electrons are scattered along the axial magnetic field lines and undergo an elongated trajectory to enter the central region by collisions induced random walk process [17, 18]. As shown in figure 7.6a, these ionizing electrons can be present at a sufficiently large distance from the hollow cathode.

Figure 7.6b, depicts this mechanism by assuming an electric circuit network consisting of parallel and series resistors corresponding to cross-field and parallel flow of electrons along the length of the magnetized plasma column. The arrows indicate the path of current carrying electrons that are initially emerged from the hollow cathode surface. These electrons will give rise to ionizing collisions along their way and enable the sustenance of downstream plasma over elongated lengths [17]. The energetic electrons will eventually reach the discharge axis after undergoing a random walk process and will eventually flow towards the anode due to the accelerating axial electric field.

In figure 7.6b, the individual resistors along the B-field (i.e. R_1, R_2, \dots etc..) represents the parallel resistance (i.e. R_{\parallel}). Whereas, all the resistive components across

the B-field (i.e. R_a, R_b, \dots etc..) represents the perpendicular resistance (i.e. R_\perp). Therefore with increase in axial magnetic field, the length of the plasma column and all the individual components of R_\parallel and R_\perp adjust in such a manner that there is a net flow of discharge current I_{dis} through the plasma column. In view of the above model, the equivalent resistor R_p in figure 7.6b is responsible for the ohmic dissipation of power $I_{dis}^2 R_p$ in the entire plasma column.

The equivalent resistance of the plasma column (i.e. R_p) can be estimated from D.C conductivity of the plasma $\sigma_{dc} = (\bar{n}e^2)/m\nu_m$, where \bar{n} is the average plasma density corresponding to the primary current carrying electrons.

$$R_p = \frac{1}{\sigma_{dc}} \frac{L_p}{A_p} \quad (7.4)$$

In the magnetized case, the parallel component of plasma conductivity, $\sigma_\parallel = \sigma_{dc}$ whereas the perpendicular component σ_\perp is given by [1, 17];

$$\sigma_\perp = \frac{\bar{n}e^2}{m\nu_m} \left(\frac{1}{1 + \omega_{ce}^2/\nu_m^2} \right) \quad (7.5)$$

In the limit when $\omega_{ce}/\nu_m \gg 1$, σ_\perp reduces to;

$$\sigma_\perp \approx \frac{\bar{n}e^2}{m\omega_{ce}^2} \nu_m \approx \varepsilon_0 \frac{\omega_{pe}^2}{\omega_{ce}^2} \nu_m \quad (7.6)$$

As seen in equation 7.6, the role of ν_m in σ_\perp is reversed as compared to σ_\parallel . Also, one observes that $\sigma_\parallel \approx \omega_{ce}^2 \sigma_\perp$ such that $\sigma_\parallel \gg \sigma_\perp$. Therefore the radial current across the magnetic field lines is drastically reduced. Hence current carrying primary electrons follows a long trajectory along the magnetic field lines to complete the discharge circuit as shown in figure 7.6a. The longer path length will allow more number of collisions and enables the electrons from the lateral surface to reach the central line by cross-field diffusion [17].

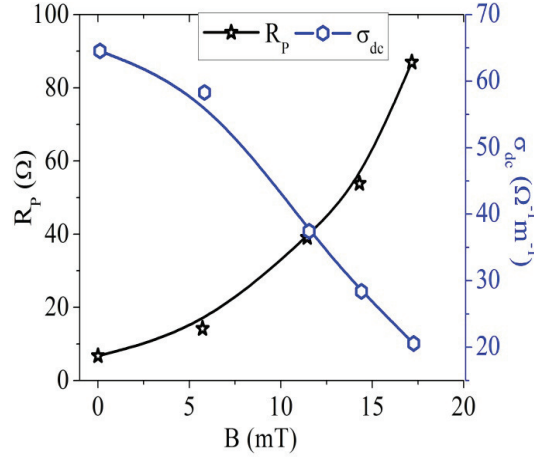


Figure 7.7: Effect of magnetic field on plasma resistance R_p and plasma conductivity σ_{dc} at a neutral gas pressure of 1.4 Pa.

7.3.1 Model to determine the length of magnetized plasma column

From the electrical analogy presented above, the plasma column length can be estimated. This characteristic length corresponds to an equilibrium case when equivalent resistance across and along the magnetic field balances each other [17].

Assuming an average electron density \bar{n}_{eh} for the primary electrons, the conductivity of the plasma channel can be estimated for different magnetic field strengths. In figure 7.7, the obtained values of plasma resistance R_p and plasma conductivity σ_{dc} have been plotted as a function of axial magnetic field. It can be seen that the plasma resistance and plasma conductivity are inversely related. If L_p and A_p are considered as the overall length and the cross-sectional area of the conducting plasma channel, then the ratio $L_p/A_p \approx R_p\sigma_{dc}$.

Therefore, it is qualitatively found that the ratio $L_p/A_p \approx R_p\sigma_{dc}$ increases with the increase in axial magnetic field. This phenomenology can be modeled considering the continuity of radial and axial currents in the plasma column [17].

As shown in figure 7.8, the parallel electron flux $\Gamma_{||}$ in the central line is collected at the anode, while the axial loss is compensated by the perpendicular electron

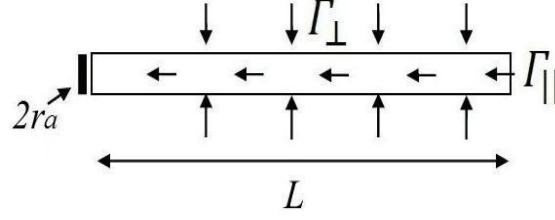


Figure 7.8: Perpendicular and parallel electron fluxes entering and leaving magnetized plasma tube assuming the plasma column to be homogeneous. Here r_a is the radius of anode which is assumed to be the radius of magnetized plasma column and L_p is the length of magnetized plasma column.

flux Γ_{\perp} from the lateral surface of the cylindrical column. Hence, considering the current continuity we can write;

$$(2\pi r_a L_p) e \Gamma_{\perp} = (\pi r_a^2) e \Gamma_{\parallel} \quad (7.7)$$

Where r_a is the radius of the anode. Again Γ_{\perp} and Γ_{\parallel} can be expressed as follows;

$$\Gamma_{\perp} = -D_{\perp} \frac{\partial n}{\partial r} \approx -\frac{kT_{eh}}{m\nu_{iz}(1 + \omega_{ce}^2/\nu_{iz}^2)} \left(\frac{n_0}{r_a} \right) \quad (7.8)$$

Whereas along the magnetic field, the electron current is mainly governed by the drift due to axial electric field E . Assuming Boltzmann distribution for hot electrons; $n = n_0 \exp(-e\phi/kT_{eh})$ and also using Einstein equation; $D_{\parallel}/\mu_{\parallel} = kT_{eh}/e$, one can express [1, 17];

$$\Gamma_{\parallel} = -n\mu_{\parallel} E_z \approx -\frac{kT_{eh}}{m\nu_{iz}} \frac{\partial n}{\partial z} \approx -\frac{kT_{eh}}{m\nu_{iz}} \left(\frac{n_0}{L_p} \right) \quad (7.9)$$

In the above equations, n_0/L_p and n_0/r_a has been approximated as axial and radial density gradient respectively. Thus equation 7.7 can be reduced to a scaling expression of L_p in terms of magnetic field as [17],

$$L_p \approx \frac{r_a}{\sqrt{2}} \sqrt{1 + \left(\frac{\omega_{ce}}{\nu_{iz}} \right)^2} \quad (7.10)$$

From the above equation, it can be seen that the length of the plasma column L_p is directly related to the magnetic field via ω_{ce} , while it is inversely proportional

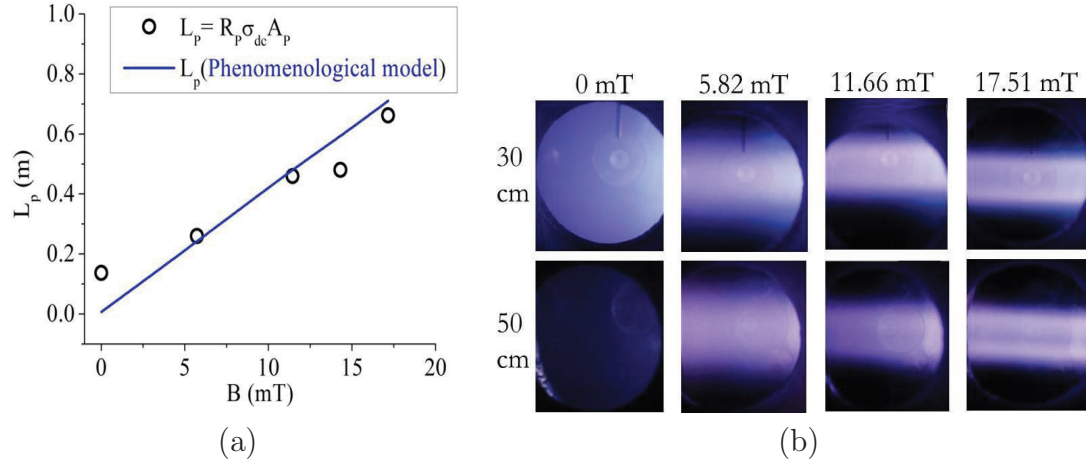


Figure 7.9: (a): The estimated length of plasma column for different axial magnetic field strengths. (b): Side view of magnetized plasma column at a neutral gas pressure of 1.4 Pa.

to the ionizing collision frequency (i.e. ν_{iz}) / or neutral pressure [17]. Therefore the length of the plasma column increases with magnetic field while it is expected that the length will get shorter with increase in pressure because the collisions will enhance the cross-field diffusion across the magnetic field. As shown in figure 7.9a the approximate length of plasma column estimated from the electrical analogy and from the phenomenological model are in qualitative agreement. It is also evinced from the visual images of the plasma column (i.e figure 7.9b) that the length of the plasma column gradually increases with increase in axial magnetic field [17].

7.4 Results and Discussion

The phenomenological model provides an insight into the role of secondary electron transport in the downstream plasma region for the sustenance of elongated plasma column in presence of axial magnetic field in a HC plasma source [17]. Mainly, the secondary electrons after being liberated from the HC surface flows along the magnetic field lines; therefore a high resistance is developed between the HC and the centrally located anode. Since the journey of these electrons to the anode is mostly along the field lines, the effective plasma resistance R_p in the electrical model is mostly governed by the DC conductivity of hot primary electrons that constitutes the return current towards the anode by following along the B-field [17].

In figure 7.5, the density distribution of hot / primary electron population show a contrasting trend as compared with its temperature distribution. The temperature of these electrons is observed to be consistently higher away from the anode. This is because the energetic primary electrons are constrained to flow along the field lines as they travel a long distance via the cross-field diffusion process towards the anode. Hence the temperature/ energy of these primary electrons is expected to fall systematically towards the anode as they undergo ionizing collisions with the background neutrals all along its path [17].

To account for the observed density/ temperature profile of hot primary electrons, we consider the discharge current at anode as;

$$I_{dis}/A_{anode} = e\Gamma_{||} \approx J_{dis} \quad (7.11)$$

Where, A_{anode} = area of anode and J_{dis} = discharge current density at anode. Assuming Boltzmann distribution, primary electron flux can be given as $\Gamma_{||} = -n\mu_{||}E \approx -\frac{kT_e}{m\nu_m} \frac{\partial n}{\partial z} \approx -\frac{kT_e}{m\nu_m} \left(\frac{n_{eh}}{L_p} \right)$. Hence one can arrive at an approximate expression for hot electron flux [17];

$$[n_{eh}T_{eh}] \approx \frac{(J_{dis}L_p)}{\mu_{||}} \quad (7.12)$$

Where T_{eh} is expressed in eV and density of hot electrons n_{eh} in m^{-3} .

Since the discharge current, magnetic field and neutral gas pressure are constants, therefore the product $[n_{eh}T_{eh}] \sim \text{constant}$; implies an inverse relationship between density and temperature of primary electrons as evinced in figure 7.5. In view of the above facts, it can be concluded that the magnetic field steers the primary electron current through the bulk plasma and hence it helps in sustaining an elongated plasma column.

Summary and conclusion

In summary, this chapter provides a basic insight into one of the fundamental properties of a HC sustaining an elongated magnetized plasma column. In particular, the role of primary electrons in carrying out the ionization along the magnetized plasma column is illustrated. The current closure through the plasma column is depicted through an equivalent electrical analogy of the discharge. The phenomenological model provides a semi-empirical relationship between the length of the plasma column and the experimental conditions of neutral gas pressure and magnetic field strength. The concept can be useful for the understanding of radial and axial transport of the primary electrons in magnetized plasma physics experiments.

8

Conclusions and Future Scope

8.1 Summary and conclusion

The thesis presents some unique behavior of cold hollow cathode discharges operated under the influence of an external magnetic field. In particular, it investigates how the electrode geometry and the applied magnetic field affect the properties of the downstream plasma column produced outside the source. The investigation has been meticulously carried out using an electrical probe diagnostic, which is improvised specifically for application in a magnetized plasma system; where the discharge electrodes and the bulk plasma is electrically isolated from the grounded chamber. Along with the experiments, a substantial part of the thesis devotes to the development of phenomenological models of plasma produced by cold hollow cathode discharge. Some elegant results obtained from the analytical modeling are the secondary electron emission yield under the influence of the oblique magnetic field at the cathode surface. The secondary electrons are not only vital for the sustenance of DC discharge, but they are the ones that primarily govern the plasma characteristics (both axial as well as radial) in the downstream plasma region. This fact has been elucidated by comparing the radial plasma characteristics of cylindrical and conical hollow cathode plasma sources. It is shown that if the magnetic field is tangential at the hollow cathode surface, then the secondary electrons give rise to an elongated hollow plasma column by inevitably flowing along the magnetic field lines close to the cathode surface. However, by providing an oblique angle between the cathode surface and axial magnetic field; the above

hollow profile of the plasma column can be tuned to a solid plasma profile. In both the above plasma devices, since the location of anode is at the center, the current carrying electrons flow along the magnetic field lines in an elongated trajectories to constitute the return current at anode.

In the entire investigation, along with the development of above experimental devices, some unique phenomenological models are also formulated. In Chapter-7, the elongation in the length of the magnetized plasma column is shown by considering an electrical analogy of the discharge. Here, a simple resistive network represents the plasma column and using the radial and axial current continuity in the discharge, a relationship between the characteristic plasma column length versus the axial magnetic field strength is established. Likewise in Chapter-5, the effect of the magnetic field on cathode fall thickness and secondary electron emission yield has been derived. The combination of these analytical results and experimental data obtained for a fixed set of electrode geometries are useful for benchmarking the formulated models. Also, as demonstrated in Chapter-4 the phenomenological model is further used for predicting how the apex angle of the conical cathode would affect the peak plasma density and average electron temperature inside the hollow cathode cavity. The formulated models also explain the contrasting nature of the radial plasma characteristics observed for cylindrical and conical cathodes.

In conclusion, the thesis offers a broad physical understanding about the DC operated hollow cathode discharge for producing intense plasma column in linear devices; how the electrode geometries and the magnetic field can be utilized for obtaining unique plasma features and how the modeling can help in the optimization of the design of a plasma source. Not only the above mentioned results are demonstrated for the hollow cathode discharges, but some of the findings pertaining to current closure between a pair of electrodes placed across magnetic field lines are also relevant in applications such as cascaded arc sources used for high heat flux experiments [81, 84, 85]; electrically biased plasma facing components [82, 86], the filter field region of a negative ion source and magnetron sputtering discharges wherein the magnetic filter field is transverse to the sheath electric field. The secondary electron emission from a target in the presence of an oblique magnetic

field at the sheath is also relevant for the diverter and limiter in contact with the strongly magnetized plasma of a fusion device [85]. The transport of charge particles across the magnetic field is also important during the application of electric probes in magnetized plasma. The thesis also provides a comprehensive discussion on how global modeling based on experimental observation can be comprehended together to obtain an in-depth insight into the discharge dynamics without having to rely on expensive computational techniques. The physical understanding gathered from this study can be helpful in designing and optimization of the plasma source based on cold hollow cathode discharges and all other sources based on a similar concept.

8.2 Future Scope

The thesis presented here considers a 1-Dimensional fluid approach for a geometrically symmetric system of electrodes. This experimental and modeling study provided a qualitative insight into the phenomenology behind the magnetized hollow cathode DC discharge for a particular set of electrode configuration. The axial variation in plasma parameters, though it was grossly marginal in the present experiments; can be often relevant in discharges where a double layer can exist which can alter the positive ion dynamics along the magnetic field lines. Hence comprehensive modeling of DC hollow cathode discharge should be extended for a 2-Dimensional case also. Secondly, the present study has been focused on a partially magnetized case in which the electrons inside the hollow cavity are the ones that are magnetized. However, for application in strongly magnetized linear devices, the entire dynamics of charge particles inside as well as outside the hollow cathodes can be substantially different. Hence the above model can very well be revisited for the strongly magnetized case in which the ions are also magnetized. It is also important that the hollow cathode discharge can also be operated with the application of RF as well as by pulsed DC. The discharges operated using RF can operate at low pressures and are very much relevant for material processing applications. Another unique feature observed in the experiments is the role of cathode geometry and the external magnetic field in achieving radial density and temperature variation inside the magnetized plasma column. The radial tempera-

ture gradient inside plasma has some interesting applications such as in negative ion sources where the negative ion species are formed by a two-step process which requires the presence of both hot as well as a cold population of electrons inside the discharge [87]. The hollow cathode source in conjunction with the constricted anode presented in this thesis can also be extended to an array of hollow cathode sources to generate large area plasmas with easily tunable plasma profiles with the help of an axial magnetic field in the system. The arrangement of multiple hollow cathodes (i.e. with cylindrical / conical geometry) helps to generate large diameter plasma; whose spatial plasma characteristics (i.e. typically density and temperature profile in the system) can be controlled independently by controlling the individual hollow cathodes. Such a magnetoplasma device has a potential application in the manufacturing of the advanced ultra large scale integrated circuit (ULSI) to carry out plasma processing on large diameter wafers [88, 89].

The intuitive observations presented above can form the basis for a comprehensive study on the applications of DC discharges operated with hollow cathodes under the influence of the magnetic field.

Abstract

An experimental and modeling study of a magnetized cold hollow cathode DC discharge is presented. In particular, two distinct plasma sources having electrode configurations; (1): a cylindrical hollow cathode with an axially placed constricted anode and (2): a cone-shaped hollow cathode with a constricted anode at its minor end has been designed and investigated. It is found that the magnetic field has a phenomenal effect on the gross discharge performance of these plasma devices as well as it also impacts the radial properties of the plasma column resulting from each hollow cathode source. A detailed characterization of the plasma column has been performed using a single Langmuir probe, which provides key insight into the role of primary electrons in the sustenance of the magnetized plasma column. It is demonstrated that the secondary electron emission yield can be enhanced by providing an oblique cathode surface w.r.t magnetic field lines instead of applying it tangential to the cathode. The current closure through the plasma column to the opposing electrode by the primary electrons has been depicted through an equivalent electrical analogy of the discharge. Based on electrical discharge parameters, a phenomenological model has been formulated for explaining the formation of an elongated plasma column under the application of an axial magnetic field in a linear device. Moreover, an in-depth analysis of Langmuir probe characteristics to extract the information of the hot and bulk electron population has been recommended for the case when the probe reference electrode is partially conducting to the ground.

A significant part of the work is focussed on the development of phenomenological models to characterize the DC hollow cathode discharges for cylindrical / conical cathodes. These modeling results are found to be in good qualitative agreement with the experiments. From the engineering perspective, the above experimental and modeling study provides a key insight into the design and optimization of the plasma sources based on the concept of magnetized hollow cathode discharges.

Thesis Highlight

Name of the Student: Mr. Montu Prafulbhai Bhuvu

Name of the CI/OCC: Institute for Plasma Research, Gandhinagar

Enrolment No.: ENGG06201504002

Thesis Title: Magnetic field effects on Cold Hollow Cathode DC Discharge – An Experimental and Modeling Study

Discipline: **Engineering Sciences**

Sub-Area of Discipline: **Basic Plasma Physics**

Date of viva voce: 22nd February, 2021

In this thesis work, experimental and modeling investigation of a magnetized cold hollow cathode DC has been ensued. In particular, two distinct plasma sources having electrode configurations; (1): a cylindrical hollow cathode with an axially placed constricted anode and (2): a cone-shaped hollow cathode with a constricted anode at its minor end has been designed and investigated. The two hollow cathode plasma sources developed for this work are shown in Figure:1 Cylindrical hollow cathode plasma source and Figure:2 Conical hollow cathode plasma source. External magnetic field is introduced such that it remains axial w.r.t the hollow cathodes in both these sources.

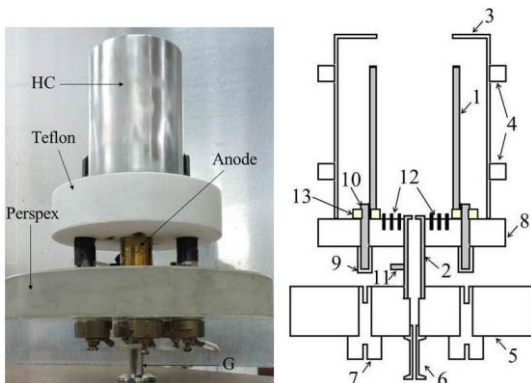


Figure 1: Image and schematic of a cylindrical hollow cathode source

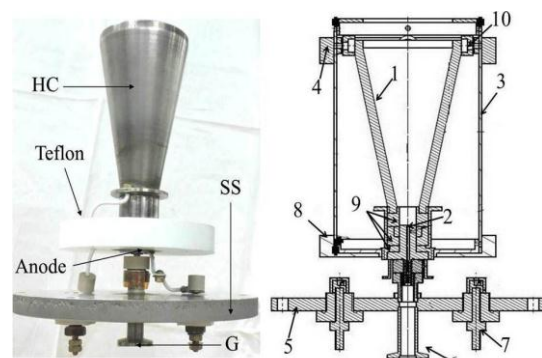


Figure 2: Image and schematic of a conical hollow cathode source

It is found that the axial magnetic field has a phenomenal effect on the gross discharge properties of these plasma devices as well as it also impacts the radial properties of the plasma column resulting from each hollow cathode source. A detailed characterization of these plasma devices has been performed using a cylindrical Langmuir probe. All the measured experimental results are substantiated by formulating the appropriate phenomenological models which provides a deep insight into the ionization mechanisms taking place inside the cylindrical and conical hollow cathode cavities. As shown in Figure:3, It is also demonstrated that the secondary electron emission yield can be enhanced by providing an oblique cathode surface w.r.t magnetic field lines instead of applying it tangential to the cathode.

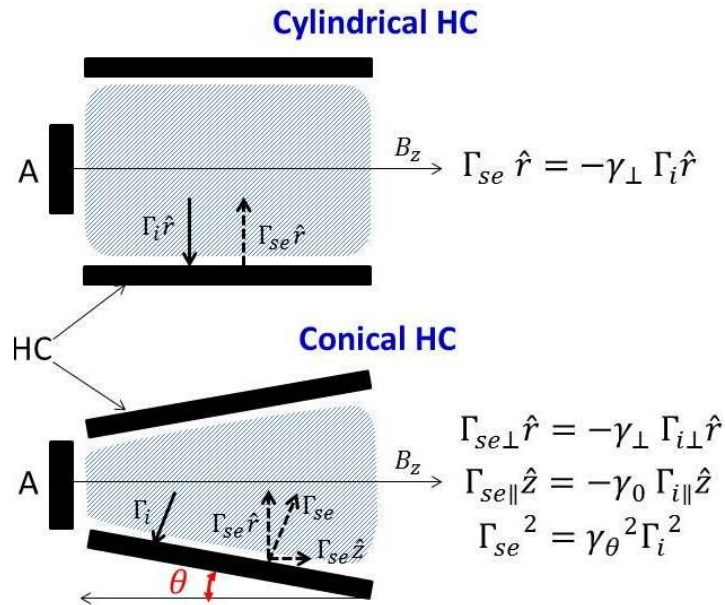


Figure 3: Secondary electron yield from a cylindrical and a conical hollow cathode source

Also, the current closure through the magnetized plasma column to the opposing electrode by the primary electrons has been depicted through an equivalent electrical analogy of the discharge. Based on electrical discharge parameters, a phenomenological model has been formulated for explaining the formation of an elongated plasma column under the application of an axial magnetic field in a linear device. Moreover, an in-depth analysis of Langmuir probe characteristics to extract the information of the hot and bulk electron population has been recommended for the case when the probe reference electrode is partially conducting to the ground.

A significant part of the work is focussed on the development of phenomenological models to characterize the DC hollow cathode discharges for cylindrical / conical cathodes. These modeling results are found to be in good qualitative agreement with the experiments. From the engineering perspective, the above experimental and modeling study provides a key insight into the design and optimization of the plasma sources based on the concept of magnetized hollow cathode discharges.

Bibliography

- [1] Michael A Lieberman and Alan J Lichtenberg. *Principles of plasma discharges and materials processing*. John Wiley & Sons, 2005. doi:[10.1002/0471724254](https://doi.org/10.1002/0471724254).
- [2] Brian N Chapman. *Glow discharge processes*. Wiley, 1980. URL <http://as.wiley.com/WileyCDA/WileyTitle/productCd-047107828X.html>.
- [3] J.R. Roth. *Industrial Plasma Engineering: Volume 2 - Applications to Non-thermal Plasma Processing*. Industrial Plasma Engineering. Taylor & Francis, 2001. ISBN 9780750305457. URL <https://books.google.co.in/books?id=ISf2Zu3ZcDAC>.
- [4] Jon Tomas Gudmundsson and Ante Hecimovic. Foundations of dc plasma sources. *Plasma Sources Science and Technology*, 26(12):123001, 2017. doi:[10.1088/1361-6595/aa940d](https://doi.org/10.1088/1361-6595/aa940d).
- [5] Robert K Waits. Planar magnetron sputtering. *Journal of Vacuum Science and Technology*, 15(2):179–187, 1978. doi:[10.1116/1.569451](https://doi.org/10.1116/1.569451).
- [6] JW Bradley. The plasma properties adjacent to the target in a magnetron sputtering source. *Plasma sources science and technology*, 5(4):622, 1996. doi:[10.1088/0963-0252/5/4/003](https://doi.org/10.1088/0963-0252/5/4/003).
- [7] John A Thornton. Magnetron sputtering: basic physics and application to cylindrical magnetrons. *Journal of Vacuum Science and Technology*, 15(2):171–177, 1978. doi:[10.1116/1.569448](https://doi.org/10.1116/1.569448).
- [8] SN Abolmasov. Physics and engineering of crossed-field discharge devices. *Plasma Sources Science and Technology*, 21(3):035006, 2012. doi:[10.1088/0963-0252/21/3/035006](https://doi.org/10.1088/0963-0252/21/3/035006).
- [9] Catherine Journet, WK Maser, Patrick Bernier, Annick Loiseau, M Lamy de La Chapelle, dl S Lefrant, Philippe Deniard, R Lee, and JE Fischer. Large-scale production of single-walled carbon nanotubes by the electric-arc technique. *nature*, 388(6644):756–758, 1997. doi:[10.1038/41972](https://doi.org/10.1038/41972).

- [10] Wenjing Lu, Yawar Abbas, Muhammad Farooq Mustafa, Chao Pan, and Hongtao Wang. A review on application of dielectric barrier discharge plasma technology on the abatement of volatile organic compounds. *Frontiers of Environmental Science & Engineering*, 13(2):30, 2019. doi:[10.1007/s11783-019-1108-5](https://doi.org/10.1007/s11783-019-1108-5).
- [11] Artem Smirnov, Yegeny Raitses, and Nathaniel J Fisch. Experimental and theoretical studies of cylindrical hall thrusters. *Physics of Plasmas*, 14(5):057106, 2007. doi:[10.1063/1.2718522](https://doi.org/10.1063/1.2718522).
- [12] A Smirnov, Y Raitses, and NJ Fisch. Electron cross-field transport in a low power cylindrical hall thruster. *Physics of Plasmas*, 11(11):4922–4933, 2004. doi:[10.1063/1.1791639](https://doi.org/10.1063/1.1791639).
- [13] P.K. Shukla and A.A. Mamun. *Introduction to Dusty Plasma Physics*. Series in Plasma Physics. CRC Press, 2015. ISBN 9781420034103. URL <https://books.google.co.in/books?id=WR5pAYrdQ9cC>.
- [14] EB Hooper Jr. Characteristics of a reflex arc: Low magnetic field mode. *Plasma Physics*, 12(11):855, 1970. doi:[10.1088/0032-1028/12/11/004](https://doi.org/10.1088/0032-1028/12/11/004).
- [15] EB Hooper Jr and Steven M Girvin. Characteristics of turbulence in a reflex-arc plasma. *Journal of Applied Physics*, 42(12):4832–4840, 1971. doi:[10.1063/1.1659862](https://doi.org/10.1063/1.1659862).
- [16] SK Karkari, SK Mishra, and PK Kaw. Sustenance of inhomogeneous electron temperature in a magnetized plasma column. *Physics of Plasmas*, 22(9):092107, 2015. doi:[10.1063/1.4930129](https://doi.org/10.1063/1.4930129).
- [17] MP Bhuvu, SK Karkari, and Sunil Kumar. Characteristics of an elongated plasma column produced by magnetically coupled hollow cathode plasma source. *Physics of Plasmas*, 25(3):033509, 2018. doi:[10.1063/1.5021309](https://doi.org/10.1063/1.5021309).
- [18] MP Bhuvu, SK Karkari, and Sunil Kumar. Influence of cold hollow cathode geometry on the radial characteristics of downstream magnetized plasma column. *Plasma Sources Science and Technology*, 28(11):115013, 2019. doi:[10.1088/1361-6595/ab53dc](https://doi.org/10.1088/1361-6595/ab53dc).

- [19] M.A. Gundersen and G. Schaefer. *Physics and Applications of Pseudosparks*. Nato Science Series B:. Springer US, 2012. ISBN 9781461537861. URL <https://books.google.co.in/books?id=xjXSBwAAQBAJ>.
- [20] André Anders. Plasma and ion sources in large area coating: A review. *Surface and Coatings Technology*, 200(5-6):1893–1906, 2005. doi:[10.1016/j.surfcoat.2005.08.018](https://doi.org/10.1016/j.surfcoat.2005.08.018).
- [21] Michael A Lieberman and Richard A Gottscho. Design of high-density plasma sources for materials processing. In *Physics of Thin Films*, volume 18, pages 1–119. Elsevier, 1994. doi:[10.1016/B978-0-08-092513-4.50006-4](https://doi.org/10.1016/B978-0-08-092513-4.50006-4).
- [22] Andrew Hurlbatt, Andrew Robert Gibson, Sandra Schröter, Jérôme Bredin, Alexander Paul Stuart Foote, Pascaline Grondein, Deborah O’Connell, and Timo Gans. Concepts, capabilities, and limitations of global models: a review. *Plasma Processes and Polymers*, 14(1-2):1600138, 2017. doi:[10.1002/ppap.201600138](https://doi.org/10.1002/ppap.201600138).
- [23] Montu P Bhuvra and Shantanu K Karkari. The role of apex angle of a cone-shaped hollow cathode on plasma parameters. *IEEE Transactions on Plasma Science*, 47(6):2929–2936, 2019. doi:[10.1109/TPS.2019.2914269](https://doi.org/10.1109/TPS.2019.2914269).
- [24] A. von Engel. *Ionized Gases*. AVS Classics in Vacuum Science and Technology. American Inst. of Physics, 1997. ISBN 9781563962721. URL https://books.google.co.in/books?id=YWfcfSe5n_EC.
- [25] P. Chabert and N. Braithwaite. *Physics of Radio-Frequency Plasmas*. Cambridge University Press, 2011. ISBN 9781139494687. URL <https://books.google.co.in/books?id=oB03j-bbNXcC>.
- [26] Y.P. Raizer, M.N. Shneider, and N.A. Yatsenko. *Radio-Frequency Capacitive Discharges*. CRC Press, 2017. ISBN 9781351419963. URL <https://books.google.co.in/books?id=RwZDDwAAQBAJ>.
- [27] VI Kolobov and LD Tsendin. Analytic model of the hollow cathode effect. *Plasma Sources Science and Technology*, 4(4):551, 1995. doi:[10.1088/0963-0252/4/4/006](https://doi.org/10.1088/0963-0252/4/4/006).

- [28] Radu Mavrodineanu. Hollow cathode discharges. *JOURNAL OF RESEARCH of the National Bureau of Standards*, 89(2):143–185, 1984. URL https://nvlpubs.nist.gov/nistpubs/jres/089/jresv89n2p143_A1b.pdf.
- [29] K Frank and J Christiansen. The fundamentals of the pseudospark and its applications. *IEEE Transactions on Plasma Science*, 17(5):748–753, 1989. doi:[10.1109/27.41195](https://doi.org/10.1109/27.41195).
- [30] Udit Narayan Pal, Niraj Kumar, Deepak Kumar Verma, Jitendra Prajapati, Mahesh Kumar, Vishnu Srivastava, Harish Kumar Dwivedi, and Ram Prakash. Development of low-pressure high-current plasma cathode electron gun and use of associated techniques. *Journal of Theoretical and Applied Physics*, 6(1):36, 2012. URL <https://link.springer.com/content/pdf/10.1186/2251-7235-6-36.pdf>.
- [31] ME Pillow. A critical review of spectral and related physical properties of the hollow cathode discharge. *Spectrochimica Acta Part B: Atomic Spectroscopy*, 36(8):821–843, 1981. doi:[10.1016/0584-8547\(81\)80064-X](https://doi.org/10.1016/0584-8547(81)80064-X).
- [32] Stephen Muhl and Argelia Pérez. The use of hollow cathodes in deposition processes: A critical review. *Thin Solid Films*, 579:174–198, 2015. doi:[10.1016/j.tsf.2015.02.066](https://doi.org/10.1016/j.tsf.2015.02.066).
- [33] Jean-Loup Delcroix and Armando Rocha Trindade. Hollow cathode arcs. In *Advances in Electronics and Electron Physics*, volume 35, pages 87–190. Elsevier, 1974. doi:[10.1016/S0065-2539\(08\)60281-4](https://doi.org/10.1016/S0065-2539(08)60281-4).
- [34] F Boeschoten, R Komen, and AFC Sens. An investigation of the positive column of a hollow cathode arc in a magnetic field. part i. *Zeitschrift für Naturforschung A*, 34(8):1009–1021, 1979. doi:[10.1515/zna-1979-0815](https://doi.org/10.1515/zna-1979-0815).
- [35] PAEM Janssen and F Boeschoten. An investigation of the positive column of a hollow cathode arc in a magnetic field. part ii. *Zeitschrift für Naturforschung A*, 34(8):1022–1028, 1979. doi:[10.1515/zna-1979-0816](https://doi.org/10.1515/zna-1979-0816).
- [36] W Knauer. Mechanism of the penning discharge at low pressures. *Journal of Applied Physics*, 33(6):2093–2099, 1962. doi:[10.1063/1.1728902](https://doi.org/10.1063/1.1728902).

- [37] E Klawuhn, GC D'Árcouto, KA Ashtiani, P Rymer, MA Biberger, and KB Levy. Ionized physical-vapor deposition using a hollow-cathode magnetron source for advanced metallization. *Journal of Vacuum Science & Technology A: Vacuum, Surfaces, and Films*, 18(4):1546–1549, 2000. doi:[10.1116/1.582382](https://doi.org/10.1116/1.582382).
- [38] Matheswaran Kiruthika and Gurusamy Shanmugavelayutham. Characteristics of anodic glow pulsed plasma. *Physics Letters A*, 384(1):126040, 2020. doi:[10.1016/j.physleta.2019.126040](https://doi.org/10.1016/j.physleta.2019.126040).
- [39] MA Mujawar, SK Karkari, and MM Turner. Properties of a differentially pumped constricted hollow anode plasma source. *Plasma Sources Science and Technology*, 20(1):015024, 2011. doi:[10.1088/0963-0252/20/1/015024](https://doi.org/10.1088/0963-0252/20/1/015024).
- [40] D Mihailova, J van Dijk, GJM Hagelaar, S Karatodorov, P Zahariev, M Grozeva, and JJAM van der Mullen. Geometrical features in longitudinal sputtering hollow cathode discharges for laser applications. *Journal of Physics D: Applied Physics*, 45(16):165201, 2012. doi:[10.1088/0022-3727/45/16/165201](https://doi.org/10.1088/0022-3727/45/16/165201).
- [41] Francis F Chen et al. *Introduction to plasma physics and controlled fusion*, volume 1. Springer, 1984. doi:[10.1007/978-1-4757-5595-4](https://doi.org/10.1007/978-1-4757-5595-4).
- [42] H Eichhorn, KH Schoenbach, and T Tessnow. Paschen's law for a hollow cathode discharge. *Applied physics letters*, 63(18):2481–2483, 1993. doi:[10.1063/1.110455](https://doi.org/10.1063/1.110455).
- [43] KH Becker, KH Schoenbach, and JG Eden. Microplasmas and applications. *Journal of Physics D: Applied Physics*, 39(3):R55, 2006. doi:[10.1088/0022-3727/39/3/R01](https://doi.org/10.1088/0022-3727/39/3/R01).
- [44] Vinitkumar J Gandhi and SM Mahajan. Effect of the inside profile of a hollow cathode on the plasma plume. *IEEE transactions on plasma science*, 20(4):410–412, 1992. doi:[10.1109/27.256768](https://doi.org/10.1109/27.256768).
- [45] Tae S Cho, Qing Han, Dongqing Yang, Soonam Park, Dima Lubomirsky, and Shankar Venkataraman. Optimization of hollow cathode discharge electrode for damage free remote plasma removal process for semiconductor

- manufacturing. *Japanese Journal of Applied Physics*, 55(5):056201, 2016. doi:[10.7567/JJAP.55.056201](https://doi.org/10.7567/JJAP.55.056201).
- [46] AD White. New hollow cathode glow discharge. *Journal of Applied Physics*, 30(5):711–719, 1959. doi:[10.1063/1.1735220](https://doi.org/10.1063/1.1735220).
- [47] C Costin, G Popa, and G Gousset. On the secondary electron emission in dc magnetron discharge. *J. Optoelectron. Adv. Mater*, 7:2465–9, 2005. URL https://old.joam.inoe.ro/rohiva/pdf7_5/Costin.pdf.
- [48] JM Somerville. Sparking potentials in a transverse magnetic field. *Proceedings of the Physical Society. Section B*, 65(8):620, 1952. doi:[10.1088/0370-1301/65/8/312](https://doi.org/10.1088/0370-1301/65/8/312).
- [49] O Baranov, M Romanov, S Kumar, XX Zhong, and K Ostrikov. Magnetic control of breakdown: Toward energy-efficient hollow-cathode magnetron discharges. *Journal of applied physics*, 109(6):063304, 2011. doi:[10.1063/1.3553853](https://doi.org/10.1063/1.3553853).
- [50] D Sriram and KK Jain. Effect of magnetic field on breakdown voltage characteristics of a multigap pseudospark. *Applied physics letters*, 70(23):3093–3095, 1997. doi:[10.1063/1.119101](https://doi.org/10.1063/1.119101).
- [51] Ing Hwie Tan, Mario Ueda, Renato S Dallaqua, Rogerio de Moraes Oliveira, and Jose O Rossi. Magnetic field effects on secondary electron emission during ion implantation in a nitrogen plasma. *Journal of applied physics*, 100(3):033303, 2006. doi:[10.1063/1.2201695](https://doi.org/10.1063/1.2201695).
- [52] Guy Buyle, W De Bosscher, D Depla, Karin Eufinger, Johan Haemers, and Roger De Gryse. Recapture of secondary electrons by the target in a dc planar magnetron discharge. *Vacuum*, 70(1):29–35, 2003. doi:[10.1016/S0042-207X\(02\)00664-4](https://doi.org/10.1016/S0042-207X(02)00664-4).
- [53] JW Bradley and G Lister. Model of the cathode fall region in magnetron discharges. *Plasma sources science and technology*, 6(4):524, 1997. doi:[10.1088/0963-0252/6/4/010](https://doi.org/10.1088/0963-0252/6/4/010).

- [54] MP Bhuva, SK Karkari, and S Kumar. Understanding langmuir probe characteristics of a magnetized plasma column in partial contact with grounded probe reference. *Journal of Instrumentation*, 14(11):T11009, 2019. doi:[10.1088/1748-0221/14/11/T11009](https://doi.org/10.1088/1748-0221/14/11/T11009).
- [55] R.H. Huddlestone and S.L. Leonard. *Plasma Diagnostic Techniques*. Pure and applied physics. Academic Press, 1965. URL <https://books.google.co.in/books?id=Eb08AAAAIAAJ>.
- [56] W. Lochte-Holtgreven. *Plasma Diagnostics*. AVS Classics Series. AIP Press, 1995. ISBN 9781563963889. URL <https://books.google.co.in/books?id=dv1AAQAAIAAJ>.
- [57] I. Langmuir and C.G. Suits. The collected works of irving langmuir: Electrical discharge, 1961. URL <https://books.google.co.in/books?id=ZG4PAQAAIAAJ>.
- [58] Harold M Mott-Smith and Irving Langmuir. The theory of collectors in gaseous discharges. *Physical review*, 28(4):727, 1926. doi:[10.1103/PhysRev.28.727](https://doi.org/10.1103/PhysRev.28.727).
- [59] JE Allen, RLF Boyd, and P Reynolds. The collection of positive ions by a probe immersed in a plasma. *Proceedings of the Physical Society. Section B*, 70(3):297, 1957. doi:[0370-1301/70/3/303](https://doi.org/0370-1301/70/3/303).
- [60] Francis F Chen. Langmuir probe analysis for high density plasmas. *Physics of Plasmas*, 8(6):3029–3041, 2001. doi:[10.1063/1.1368874](https://doi.org/10.1063/1.1368874).
- [61] Francis F Chen, John D Evans, and Donald Arnush. A floating potential method for measuring ion density. *Physics of Plasmas*, 9(4):1449–1455, 2002. doi:[10.1063/1.1462630](https://doi.org/10.1063/1.1462630).
- [62] Toshihiko Dote, Hiroshi Amemiya, and Torao Ichimiya. Effect of a magnetic field upon the saturation electron current of an electrostatic probe. *Japanese Journal of Applied Physics*, 3(12):789, 1964. doi:[10.1143/JJAP.3.789](https://doi.org/10.1143/JJAP.3.789).
- [63] Kazuya Uehara, Kiyoshi Yatsu, Shigeo Hagiwara, and Shoji Kojima. Ion saturation current of a plasma having two electron temperatures. *Japanese Journal of Applied Physics*, 14(11):1761, 1975. doi:[10.1143/JJAP.14.1761](https://doi.org/10.1143/JJAP.14.1761).

- [64] A. Guthrie and R.K. Wakerling. *The Characteristics of Electrical Discharges in Magnetic Fields*. Division I Volume 5 of National nuclear energy series. McGraw-Hill, 1949. URL <https://books.google.co.in/books?id=KyRRAAAAMAAJ>.
- [65] Luis Conde. An introduction to langmuir probe diagnostics of plasmas. *Madrid: Dept. Física. ETSI Aeronáut ingenieros Aeronáuticos Universidad Politécnica de Madrid*, 2011. URL <http://plasmalab.aero.upm.es/~lcl/PlasmaProbes/Probes-2010-2.pdf>.
- [66] Robert L Merlino. Understanding langmuir probe current-voltage characteristics. *American Journal of Physics*, 75(12):1078–1085, 2007. doi:[10.1119/1.2772282](https://doi.org/10.1119/1.2772282).
- [67] SB Song, Choong-Seock Chang, and Duk-In Choi. Effect of two-temperature electron distribution on the bohm sheath criterion. *Physical Review E*, 55(1):1213, 1997. doi:[10.1103/PhysRevE.55.1213](https://doi.org/10.1103/PhysRevE.55.1213).
- [68] K Günther. Theoretical study of a biased single probe in the presence of a strong magnetic field. *Contributions to Plasma Physics*, 30(1):51–57, 1990. doi:[10.1002/ctpp.2150300110](https://doi.org/10.1002/ctpp.2150300110).
- [69] K Günther and A Carlson. Fluid theory of langmuir probes in a magnetized plasma with open flux tubes. *Contributions to Plasma Physics*, 34(2-3):484–489, 1994. doi:[10.1002/ctpp.2150340260](https://doi.org/10.1002/ctpp.2150340260).
- [70] EG Thorsteinsson and Jon Tomas Gudmundsson. A global (volume averaged) model of a nitrogen discharge: I. steady state. *Plasma Sources Science and Technology*, 18(4):045001, 2009. doi:[10.1088/0963-0252/18/4/045001](https://doi.org/10.1088/0963-0252/18/4/045001).
- [71] EG Thorsteinsson and Jon Tomas Gudmundsson. A global (volume averaged) model of a nitrogen discharge: Ii. pulsed power modulation. *Plasma Sources Science and Technology*, 18(4):045002, 2009. doi:[10.1088/0963-0252/18/4/045002](https://doi.org/10.1088/0963-0252/18/4/045002).
- [72] Jon Tomas Gudmundsson. On the effect of the electron energy distribution on the plasma parameters of an argon discharge: a global (volume-

- averaged) model study. *Plasma Sources Science and Technology*, 10(1):76, 2001. doi:[10.1088/0963-0252/10/1/310](https://doi.org/10.1088/0963-0252/10/1/310).
- [73] C Lee and MA Lieberman. Global model of ar, o2, cl2, and ar/o2 high-density plasma discharges. *Journal of Vacuum Science & Technology A: Vacuum, Surfaces, and Films*, 13(2):368–380, 1995. doi:[10.1116/1.579366](https://doi.org/10.1116/1.579366).
- [74] Sumio Ashida and Michael A Lieberman. Spatially averaged (global) model of time modulated high density chlorine plasmas. *Japanese journal of applied physics*, 36(2R):854, 1997. doi:[10.1143/JJAP.36.854](https://doi.org/10.1143/JJAP.36.854).
- [75] Sungjin Kim. *An improved global model for electronegative discharge and ignition conditions for peripheral plasma connected to a capacitive discharge*. PhD thesis, EECS Department, University of California, Berkeley, 2006. URL <http://www2.eecs.berkeley.edu/Pubs/TechRpts/2006/EECS-2006-56.html>.
- [76] Derek Monahan. *Modelling the electronegative discharge*. PhD thesis, Physical Sciences, Dublin City University, Ireland, 2007. URL <http://doras.dcu.ie/17040/>.
- [77] C Lee, DB Graves, MA Lieberman, and DW Hess. Global model of plasma chemistry in a high density oxygen discharge. *Journal of the Electrochemical Society*, 141(6):1546, 1994. doi:[10.1149/1.2054960](https://doi.org/10.1149/1.2054960).
- [78] AJ Lichtenberg, IG Kouznetsov, YT Lee, MA Lieberman, ID Kaganovich, and LD Tsendin. Modelling plasma discharges at high electronegativity. *Plasma Sources Science and Technology*, 6(3):437, 1997. doi:[10.1088/0963-0252/6/3/022](https://doi.org/10.1088/0963-0252/6/3/022).
- [79] Francis F Chen and Davide Curreli. Central peaking of magnetized gas discharges. *Physics of Plasmas*, 20(5):057102, 2013. doi:[10.1063/1.4801740](https://doi.org/10.1063/1.4801740).
- [80] Davide Curreli and Francis F Chen. Cross-field diffusion in low-temperature plasma discharges of finite length. *Plasma Sources Science and Technology*, 23(6):064001, 2014. doi:[10.1088/0963-0252/23/6/064001](https://doi.org/10.1088/0963-0252/23/6/064001).

- [81] Y Hayashi, N Ohno, S Kajita, and H Tanaka. Plasma flow in peripheral region of detached plasma in linear plasma device. *Physics of Plasmas*, 23(1):012511, 2016. doi:[10.1063/1.4940310](https://doi.org/10.1063/1.4940310).
- [82] H Grote, W Bohmeyer, H-D Reiner, T Fuchs, P Kornejew, and J Steinbrink. Comparison of chemical sputtering yields for different graphites at high ion flux densities. *Journal of nuclear materials*, 241:1152–1155, 1997. doi:[10.1016/S0022-3115\(97\)80211-5](https://doi.org/10.1016/S0022-3115(97)80211-5).
- [83] Efim M Oks and Peter M Schanin. Development of plasma cathode electron guns. *Physics of Plasmas*, 6(5):1649–1654, 1999. doi:[10.1063/1.873420](https://doi.org/10.1063/1.873420).
- [84] GJH Brussaard, M Van der Steen, M Carrere, MCM Van de Sanden, and DC Schram. Langmuir probe measurements in an expanding magnetized plasma. *Physical Review E*, 54(2):1906, 1996. doi:[10.1103/PhysRevE.54.1906](https://doi.org/10.1103/PhysRevE.54.1906).
- [85] Nobuyuki Asakura, ITPA SOL, and Divertor Topical Group. Understanding the sol flow in l-mode plasma on divertor tokamaks, and its influence on the plasma transport. *Journal of nuclear materials*, 363:41–51, 2007. doi:[10.1016/j.jnucmat.2006.12.029](https://doi.org/10.1016/j.jnucmat.2006.12.029).
- [86] IC Nascimento, Yu K Kuznetsov, JHF Severo, AMM Fonseca, A Elfimov, V Bellintani, M Machida, MVAP Heller, RMO Galvão, EK Sanada, et al. Plasma confinement using biased electrode in the tcabr tokamak. *Nuclear fusion*, 45(8):796, 2005. doi:[10.1088/0029-5515/45/8/005](https://doi.org/10.1088/0029-5515/45/8/005).
- [87] Martha Bacal and HJ Doucet. Generation of negative ion-rich plasma in electro-negative gases (oxygen). *Vacuum*, 24(11-12):595–600, 1974. doi:[10.1016/0042-207X\(74\)90039-6](https://doi.org/10.1016/0042-207X(74)90039-6).
- [88] TY Kim, SJ Noh, JK Jing, KO Lee, and KH Chung. Recent results of multi-cathode electron beam plasma source. *Thin solid films*, 345(1):178–181, 1999. doi:[10.1016/S0040-6090\(99\)00110-8](https://doi.org/10.1016/S0040-6090(99)00110-8).
- [89] YB Kang, H Jeon, TY Kim, KH Chung, DK Ko, JK Jung, and SJ Noh. Properties of the plasma produced by multi-cathode electron beam plasma sources. *Thin solid films*, 341(1-2):9–12, 1999. doi:[10.1016/S0040-6090\(98\)01541-7](https://doi.org/10.1016/S0040-6090(98)01541-7).